The Dissertation Committee for Tushar Vijay Chitrakar Certifies that this is the approved version of the following Dissertation:

Predicting Deformation Mechanisms during High Speed Impact of Ag Nanoparticles

Committee:

Desiderio Kovar, Supervisor

Michael F. Becker, Co-Supervisor

John W. Keto

Eric M. Taleff

Predicting Deformation Mechanisms during High Speed Impact of Ag Nanoparticles

by

Tushar Vijay Chitrakar

Dissertation

Presented to the Faculty of the Graduate School of

The University of Texas at Austin

in Partial Fulfillment

of the Requirements

for the Degree of

Doctor of Philosophy

The University of Texas at Austin

December 2019

Dedication

To my loving parents for their continued support and encouragement

Acknowledgements

First and foremost, I would like to thank my supervisor, Dr Desiderio Kovar and my co-supervisor, Dr Michael Becker for letting me join the LAMA group to perform computational studies related to thick films produced by the LAMA experiments. Albeit a challenging experience, their invaluable guidance, continuous support and engaging conversations have helped hone my research and critical thinking skills. I would also like to thank the other members of the LAMA group (including my colleagues): Dr John Keto, Michael Gammage, Guillaume Noiseau, Jeremiah McCallister and Derek Davies. Our group and individual meetings have given me a broader outlook to my research due to their disciplines varying across various fields of science and engineering. I would like to thank the Texas Advanced Computing Center (TACC) who provided me access to their supercomputers without which my simulation times would have drastically increased beyond the timeframe of my Doctoral studies. Finally, I would like to thank all the MSE faculty, staff and graduate students for creating an ambient environment that encouraged learning and ignited interest in a wide array of topics related to material science.

Abstract

Predicting Deformation Mechanisms during High Speed Impact of Ag Nanoparticles

Tushar Vijay Chitrakar, Ph.D.

The University of Texas at Austin, 2019

Supervisor: Desiderio Kovar, Co-Supervisor: Michael F. Becker

A number of aerosol deposition methods are currently used to produce thick films by impacting particles onto a substrate at high velocities. Though these processes operate at a similar range of velocities, there are significant differences in the sizes of the particles used in the aerosol. Conventional aerosol deposition methods deposit 0.1–40 μm sized-particles, whereas the laser ablation of microparticle aerosol process uses very fine 2–40 nm nanoparticles (NPs) to produce thick films. For particles smaller than 0.1 μm, deformation mechanisms that occur upon impact have not been studied previously in a systematic manner. In this dissertation, molecular dynamic simulations are used to study the time-evolution of deformation mechanisms that occur at very small timescales and high strain rates during high speed impact of Ag NPs. The defect evolution and the underlying mechanisms for deformation are systematically studied and documented by varying the NP size, the NP impact velocity, and the NP crystallographic orientation

relative to the substrate. A wide range of microstructures ranging from polycrystalline to epitaxial morphologies are observed for these simulations. Because epitaxial deposition by particle impact has not been experimentally obtained, considerable attention is given to understanding the factors that are predicted to lead to epitaxy. Disordering is an important mechanism because it can play a role in epitaxial growth at high deposition velocities. A critical parameter is proposed to predict disordering that occurs upon impact. An alternative method to obtain epitaxial deposition at lower deposition velocities is also explored. The goal of this dissertation is to develop a thorough understanding of the available processing parameters for controlling the microstructure for a single NP deposition event. The impact studies in this dissertation provide fundamental guidelines needed to ultimately understand the formation of thick films where thousands of particles are impacted to produce a film.

Table of Contents

CHAPTER 1: Introduction

Patterned thick (1–100 μm) films that can be processed at low temperatures onto a variety of substrate materials with controlled crystallinity, porosity, composition, and morphology have several applications including high conductivity patterned Ag films for die attachments and interconnects in emerging high power SiC and GaN electronics [1–4], automotive electronics for electric vehicles [5], and front side metallizations in solar cells [6]. The performance of these devices could be further improved relative to current technologies if the Ag films were epitaxial single crystals because the conductivity would be higher than is currently possible. Even for polycrystalline films, improved film processing techniques that can produce flexible, higher conductivity films on temperature-sensitive polymeric or textile substrates are needed for high-Q inductors, capacitors, tuned circuits, and interconnects [7]. Several aerosol-based deposition processes exist for the production of these thick films where particles are impacted onto a substrate at high velocities.

In aerosol deposition processes, a gas is accelerated to supersonic velocity in a converging-diverging nozzle. The particles to be impacted are injected into the gas stream, accelerated by the gas in the nozzle, and propelled towards the substrate on which the thick film is deposited. Above a critical particle velocity, which is characteristic to each particle material and its properties, the particles form a solid, adhesive film on the substrate surface. Although the impact velocities are similar (300–1000 m/sec) for many

of these aerosol processes, the particle sizes used in each process varies considerably. The cold spray process utilizes 5–40 μm diameter particles to produce thick films over large areas [8–10], whereas the aerosol deposition method (ADM) has been developed to deposit finer 0.1–0.4 μm diameter particles [11, 12]. In the laser ablation of a microparticle aerosol (LAMA) process, even finer 2–40 nm nanoparticles (NPs) are impacted to produce patterned, microscale thick films [13–15]. Since their properties deviate from that of the bulk material, NP-based systems attract considerable interest from both academia and industry as these very small particles are ideal building blocks for new thick films with tailored properties. A systematic study and understanding of the impact of the smallest particles used in the LAMA process to produce thick films is the primary motivation of this dissertation.

For each of the deposition processes, it has been observed that there is significant plastic deformation that occurs upon impact, which is critical to the formation of dense films. In addition, the grain sizes in the deposited films [16–18] are different than the impacting particle sizes, suggesting that significant microstructural changes occur upon impact. Under certain conditions, epitaxial, single crystal films [19] have been reported, but the mechanisms that lead to the large range of microstructures that have been observed in aerosol deposited films remains unclear. Thus it is important to understand the deformation and film formation mechanisms that occur upon impact of particles at high velocities.

One example is where plastic deformation has shown to play an important role in film growth and the resulting film microstructure for the deposition of micron-sized

particles in the cold spray deposition technique. From an initial spherical shape, these particles flatten to high aspect ratios upon impact that result in the highest relative film densities (99%) among all aerosol deposition processes. A major limitation in studying the deposition process for these large particles is the necessity of using continuum models such as finite-element modeling. These models require accurate constitutive descriptions of material behavior at the high strain rates and short time scales experienced during impact. The absence of experimentally verified constitutive behavior results in significant uncertainty in their validity. Nevertheless, iterative procedures where *pre-* and *post-mortem* experiments are compared to finite element models to infer constitutive behavior has led to good correlations between experiments and modeling [20]. It has been observed that localized plastic deformation occurs along shear bands resulting in an adiabatic instability which is responsible for particle sticking upon impact [10]. Particles that do not undergo this instability bounce off the substrate whereas particles that do undergo the instability exhibit microstructures where the boundaries separating the interfaces between the original particles are readily apparent. TEM studies of the deposited films showed extensive dislocation networks, especially near the original particle interfaces, which are responsible for the generalized plasticity that leads to the large flattening of these particles upon impact [16]. The observed microstructures in these impacted films show a significant reduction in grain size compared to both the impacting particle size and the grain size within the impacting particles. For example, flattened grains with aspect ratios of ~ (2–3) and average grain sizes of 100±35 nm were observed in films impacted by micron-sized particles with a mean size of 33.9 μm [21]. The

reduction in grain size that occurs upon impact, particularly near the interfaces of previously deposited particles, has been attributed to dynamic recrystallization due to large plastic strains, heating of the films from the gas and from localized plastic deformation [22]. Although these studies have led to a reasonable understanding of the deformation behavior for these large micron-sized particles, there is less certainty about the deformation mechanisms that occur during impact of smaller particles.

Ample empirical evidence and a theoretical basis exist to support the hypothesis that the deposition behavior of smaller particles is considerably different from that of larger particles. For particles below a critical size, glissile dislocations are not stable and thus spontaneously move to the surface, where they are annihilated, leaving nearly or completely dislocation-free sub-micron particles or NPs [23]. Upon impact, these smaller particles are expected to be more resistant to plastic deformation via dislocation motion since they contain few or no pre-existing dislocations. Dislocation-driven deformation in these particles would first require dislocation nucleation, which requires higher stresses than dislocation motion from pre-existing dislocations [24]. This hypothesis is supported by the ADM technique of deposition where upon impact of Ag particles with an initial size of 0.12 μm, film densities of 85–90% were observed by Akedo *et al.* [25]. This was considerably lower than the densities of films produced via cold spraying, which suggests that the amount of deformation decreases with decreasing particle size. Also, films produced from these smaller particles did not undergo the large-scale flattening observed in films deposited from larger particles, but rather the grains remain relatively equiaxed [26]. However, the grain sizes in these resulting films were considerably smaller than the

impacting particle size. For example, the deposition of 0.4 μm Al_2O_3 particles at room temperature and a velocity of 300 m/sec resulted in nearly dense films with an average grain size of 12 nm [27]. It is postulated that the reduction in grain size relative to the impacting particle sizes occurs due to fracturing of the particles, although no direct evidence is presented to support this postulate. Thus, the deformation mechanisms upon impact remain unclear for particles in this size range.

Significant differences from the deposition of the aforementioned sub-micron and micron-sized particles have been observed during the impact of smaller NPs used in the LAMA process at similar velocities. Porous polycrystalline films have been produced from the impact of 5–10 nm Ag NPs using an impact velocity of 1000 m/sec (0.6 eV/atom) [15, 18]. The measured grain size was nearly 15 nm, the grain aspect ratio ~1, and the relative film density was 70%. For larger 16 nm Ag particles deposited at slower velocities of 320 m/sec (0.06 eV/atom), films with a density of about 42% have been obtained [28]. For other materials in this range of impact velocities/energies and particle sizes, the above results are in general agreement with the limited experimental data reported by others. For example, at an impact energy of 0.5 eV/atom with 1.9 nm Ag NPs, films with a grain size of about 10 nm were obtained (but no density measurements were made) [29]. Experiments with ionized TiN NPs showed that at deposition energies below 0.1 eV/atom, the films did not adhere to the substrate. However, at deposition energies of 3 eV/atom, porous adherent films were obtained, and at impact energies greater than 5 eV/atom, dense adherent films were produced [30]. Because of the high

velocities and short residence times during impact, it has not been possible to study the deformation mechanisms of these small impacting NPs directly through experiments.

For these small, dislocation-starved nanoparticles where dislocation nucleation stresses are large, FCC crystals can plastically deform by {111} <112> twinning which is expected to be the dominant plastic deformation mechanism at high stresses and strain rates [31]. This was validated by Carlton *et al.* who have shown that the nucleation energy for partial dislocations is lower than that for perfect dislocations for very small particle sizes in FCC nanoparticles that do not contain pre-existing dislocations [32]. Twins can be produced from nucleation of pairs of partial twinning dislocations. The region of material between pairs of partial dislocations is a stacking fault, which could lead to bands of HCP material interspersed within the FCC NP after impact. However, Carlton *et al.* showed that dislocations may be spontaneously ejected from the particle upon unloading [33], and thus, *post-mortem* analysis of the NPs alone cannot confirm the potentially complex deformation mechanisms that are active during deposition of particles in this size range. The study and prediction of mechanisms during the impact of these small NPs, specifically Ag NPs, using Molecular Dynamic (MD) simulations is thus the main focus of this dissertation.

MD Simulations are ideal tools for studying the deposition processes for small NPs because both the size (nm) and time scales (order of few picoseconds) that can be simulated are realistic relative to the experiments, thus providing an ideal platform to study the underlying deformation mechanisms that cannot be studied directly using experiments. There have been numerous MD studies involving the deposition of multiple

NPs to study film formation mechanisms. Muller used 2D MD simulations to study the deposition of multiple NPs to produce films [34]. Polycrystalline films with grains of the same size as the particles were predicted to become homo-epitaxial with the substrate and the packing densities increased with particle deposition velocity/energy. This work was among the first reported MD simulations for multiparticle impacts. Unfortunately, he used a primitive Lennard-Jones potential to model the interatomic interactions and it is now known that this formulation cannot accurately model the behavior of metallic materials. These simulations also used an unrealistic geometry relative to real NPs. Lastly, computational limitations prohibited Muller from using a more accurate 3D MD simulation approach. As a result the predicted thermal effects were unrealistically large and this affected the predicted microstructures.

The first reported 3D MD simulations to study film growth with more accurate potentials assumed that prior to impact, the particles were perfect crystals (i.e. did not contain pre-existing defects that are commonly observed experimentally such as twins) and the deposition was assumed to be at room temperature onto a substrate that was made from the same material as the particle. With these assumptions, Haberland *et al.* predicted little deformation of ~ 3.2 nm Mo NPs impacted at an energy of 0.1 eV/atom and the films were predicted to be porous, polycrystalline films with relative densities of only 50%. However, increasing the energy to 1 eV/atom resulted in greater particle deformation, denser films (80%), and large regions of epitaxy between the impacted particles. At very high energies of 10 eV/atom, epitaxial films with densities nearly the same as that of the substrate (100%) were observed; however, the original shape of the

NPs was hardly perceptible as the particles produced craters upon impact [19]. Unfortunately, no impacted films were reported at deposition energies between 1 and 10 eV/atom, and only a single particle size was studied.

Meinander *et al*. used MD simulations to study the impact of Cu NPs for a range of particle sizes from 1–9 nm with impact energies between 0.002–10 eV/atom [35]. It was observed that for the smallest ~ 1 nm NPs impacted, predicted film densities were 78% and the predicted densities stabilized to nearly 35% beyond particle sizes of ~ 6 nm for a fixed impact energy of 0.005 eV/atom. Also, when the impact energy for a fixed ~ 2.5 nm NP was increased from 0.005 eV/atom to 10 eV/atom, the film density increased from 45% to nearly fully dense films. Although the work did not focus on observing the film microstructures, the variation of particle sizes along with impact energies provided a better understanding of film densities. However, the comparison between simulation and experiment is complicated by the fact that particle sizes were assumed to be monodispersed for the simulations; experiments utilize particles with a broad size distribution for the impacted particles.

Hou and Bardotti provided the best estimates of film densities by a comparative computational and experimental study of film formation [36, 37]. The multiparticle impacts were simulated to produce a film layer-by-layer where each layer had sampled randomly sized particles similar to the size distribution from the experiment (0.8–6.4 nm). The simulations predicted films that ranged from porous, polycrystalline films with densities of 60% for impact energies of 0.25 eV/atom to highly dense (95%), polycrystalline films where a few regions of epitaxial growth were observed at impact

energies of 1.25 eV/atom. Although these studies provide useful information about the film microstructures that are expected for a range of particle sizes and impact energies, no information as to how these final microstructures evolved and why the film densities were low or high were elucidated. There are a large number of other system parameters apart from particle size and impact energy that can affect film microstructures. These include particle-particle contact angle, particle-particle relative crystallographic orientations, presence of defects in the impacting particles, and temperature, to name a few. Hence, it is highly desirable to independently study each system parameter to understand its influence on the deformation behavior of impacting particles and on the evolution of film microstructure.

Hsieh and Averback reported the first MD simulations on single NP impacts where very small (4–92 atoms only) Cu, Ni and Al NP impacts were studied for different combinations of particle-substrate material at impact energies of ~ (3.5–10) eV/atom [38, 39]. Though several deposition regimes were observed for these particles, computational restrictions limited the study to very small particles. Nordlund *et al.* furthered this study by expanding the particle diameter range to ~ 1–32 nm for impact energies ranging from a few tens of meV/atom to several MeV/atom [40]. Due to this large range of both NP sizes and impact energies, similar but more pronounced deposition regimes were observed in this study demarcated as follows: a) deposition of the NP into a non-epitaxial configuration, b) deposition of the NP directly into an epitaxial configuration, c) crater formation by liquid flow, d) crater formation by hydrostatic pressure and e) NP implantation. For the LAMA process, regimes (a) and (b) are of particular interest as

these are the ranges of deposition energies that are accessed by the experiments. For Cu NPs, a range of particle morphologies were possible, depending on the NP size and impact energy. For 1.4 nm Cu NPs, polycrystalline deposition was predicted for impact energies less than about 0.02 eV/atom, whereas epitaxial deposition was predicted at larger impact energies. The predicted energy required for epitaxial deposition increased so that for a particle size of 3.2 nm, the transition energy was nearly 1 eV/atom [41]. This has been attributed to a lowering of the surface-to-volume ratio with an increase in NP size, which resulted in a smaller release of surface energy as the larger NP impacted the substrate [42]. This study of single particle impacts can be used to define the range of film morphologies that are possible for impact energies of interest. However, since the corresponding deformation mechanisms and the defects production upon impact were not studied, an understanding of how the various microstructures and their corresponding film densities evolved is not possible.

Han *et al*. showed that 2–15 nm Cu NPs plastically deform upon impact at relatively low velocities of 25–200 m/sec and the deformed particles contain bands of stacking defects after impact [43]. Järvi *et al.* also studied low energy deposition (0.025 eV/atom) of NPs onto heated substrates via MD simulations [44]. These results showed that twins were often present in FCC particles following impact. During annealing, the twins were ejected to the surface via the motion of Shockley partial dislocations. Apart from the fact that these simulation studies were performed at impact energies that are too low to produce high quality films experimentally, they also did not track the evolution of the defects from nucleation to growth so the mechanisms of deformation were not

demonstrated. Hence, there remains a need to systematically study the deformation mechanisms during NP impact by studying the time-evolution of defects produced as well as to see how these mechanisms change when the impacting particle parameters are individually modified. This is an important goal for this dissertation.

Previous studies have demonstrated that a variety of particle and film morphologies are predicted from single and multiparticle impact simulations depending on particle sizes and impact energies. Thus, this dissertation starts with a systematic study of the post-impact evolution of the particle-substrate system and deformation mechanisms. For different combinations of particle sizes and velocities, these mechanisms are shown to vary, suggesting that a range of final morphologies from polycrystalline to epitaxial deposition are possible. In the chapter that follows, *post-mortem* TEM results from LAMA experiments conducted by others are compared to simulations and it is suggested that these are not the only deposition parameters that govern deformation and the subsequent final particle morphologies. Since epitaxial deposition at low energies is not as commonly observed for the LAMA process as well as other aerosol deposition processes, a new method to achieve epitaxy is described for specific crystallographic orientations. In the chapter that follows, deformation and related mechanisms are systematically studied as a function of orientation. Finally, an important mechanism is characterized which is observed in cases where epitaxial growth is predicted with the substrate, and a critical parameter is proposed that can explain other reported experiments and simulations of epitaxial growth.

1.1: REFERENCES

1. J.G. Bai, Z.Z. Zhang, J.N. Calata, and G.Q. Lu, in: Proceedings of IMEC2005, ASME. 415 (2005).
2. J.G. Bai and G.Q. Lu, IEEE Transactions on Device and Materials Reliability. 6, 441 (2006).
3. J.G. Bai, T.G. Lei, J.N. Calata, and G.Q. Lu, J. Mater. Res. 22, 3494 (2007).
4. L. Dupont, G. Coquery, K. Kriegel, and A. Melkonyan, Microelectr. Rel. 49, 1375 (2009).
5. U. Scheuermann, Microelectr. Rel. 49, 1325 (2009).
6. A. Mette, P.L. Richter, M. Hörteis, S.W. Glunz, Prog. in Photovol.: Res. App. 15, 627 (2007).
7. D. Huang, F. Liao, S. Molesa, D. Redinger, V. Subramanian, J. Electrochem. Soc. 150, G412 (2003).
8. T. Stoltenhoff, H. Kreye, H.J. Richter, J. Therm. Spray Tech. 11, 542 (2000).
9. C. Borchers, T. Stoltenhoff, F. Gartner, H. Kreye, H. Assadi, In: Proceedings of the Materials Research Society Conference, San Francisco, CA, Apr 17-19, 2001; vol. 673: p 7.
10. H. Assadi, F. Gärtner, T. Stoltenhoff, H. Kreye, Acta Mater. 51, 4379 (2003).
11. A. Schroth, R. Maeda, J. Akedo, M. Ichiki, Jpn. J. Appl. Phys. 37, 5342 (1998).
12. J. Akedo, M. Ichiki, K. Kikuchi, R. Maeda, Sensors and Actuators A: Physical. 69, 106 (1998).
13. W.T. Nichols, G. Malyavanatham, M.P. Beam, D.E. Henneke , J.R. Brock , M.F. Becker, J.W. Keto, In: Mat. Res. Soc. Symp. Proc., Nanophase and Nanocomposite Materials III, Materials Research Society , Warrendale, PA, 2000, editted by: Komarneni S, Parker JC, Hahn H; vol. 581: p 193.
14. G. Malyavanatham, D.T. O'Brien, M.F. Becker, W.T. Nichols, J.W. Keto, D. Kovar, S. Euphrasie, T. Loue, P. Pernod, J. Mat. Proc. Tech. 168, 273 (2005).
15. C. Huang, W.T. Nichols, D.T. O'Brien, M.F. Becker, D. Kovar, J.W. Keto, J. Appl. Phys. 101, 064902 (2007).

16. C. Borchers, F. Gartner, T. Stoltenhoff, H. Assadi, H. Kreye, J Appl Phys. 93/12, 10064 (2003).

17. M. Ichiki, J. Akedo, A. Schroth, R. Maeda, Y. Ishikawa, Jap. J. App. Phys. 36/9, 5815 (1997).

18. C. Huang, M.F. Becker, J.W. Keto, D. Kovar, J. Appl. Phys. 102, 054308 (2007).

19. H. Haberland, Z. Insepov, M. Moseler, Phys. Rev. B. 51, 11061 (1995).

20. B. Yildirim, S. Muftu, A. Gouldstone, Wear. 270, 703 (2011).

21. V.K. Champagne, M. Trexler, Y. Sohn, and G.E. Kim, in: ICAA13, 13th International Conference on Aluminum Alloys (John Wiley & Sons, Inc., 2012), p. 993.

22. C. Borchers, T. Schmidt, F. Gärtner, H. Kreye, Applied Physics A. 90, 517 (2008).

23. D. Mordehai, M. Kazakevich, D.J. Srolovitz, E. Rabkin, Acta Mater. 59, 2309 (2011).

24. J.R. Greer, W.D. Nix, Phys. Rev. B. 73, 245410 (2006).

25. J. Akedo, M. Ichiki, K. Kikuchi, R. Maeda, In: Proceedings of the 1997 10th Annual International Workshop on Micro Electro Mechanical Systems, MEMS: 1997 Jan 26-30; IEEE, Piscataway, NJ, USA. Nagoya, Jpn: 1997. p 135.

26. J. Akedo, M. Lebedev, Jpn. J. Appl. Phys. 38, 5397 (1999).

27. M. Lebedev, J. Akedo, T. Ito, J. Cryst. Growth. 275, 1301 (2005).

28. M. Nahar, Ph.D. Dissertation (University of Texas at Austin, 2012).

29. W. Bouwen, E. Kunnen, K. Temst, P. Thoen, M.J. Van Bael, F. Vanhoutte, H. Weidele, P. Lievens, R.E. Silverans, Thin Solid Films. 354, 87 (1999).

30. Y. Qiang, Y. Thurner, T. Reiners, O. Rattunde, H. Haberland, Surf. Coat. Tech. 100-101, 27 (1998).

31. G.T. Gray, Ann. Rev. Mat. Res. 42, 285 (2012).

32. C.E. Carlton, L. Rabenberg, P.J. Ferreira, Phil. Mag. Let. 88, 715 (2008).

33. C.E. Carlton, P.J. Ferreira, Micron. 43/11, 1134 (2012).

34. Muller, J. Appl. Phys. 61/7, 2516 (1987).

35. K. Meinander, K. Nordlund, Phys. Rev. B. 79, 235431 (2009).

36. Q. Hou, M. Hou, L. Bardotti, B. Prevel, P. Melinon, A. Perez, Phys. Rev. B. 62/4, 2825 (2000).

37. L. Bardotti, B. Prevel, P. Melinon, A. Perez, Q. Hou, M. Hou, Phys. Rev. B. 62/4, 2835 (2000).

38. H. Hsieh, R. S. Averback, H. Sellers, C. P. Flynn, Phys. Rev. B. 45/8, 4417 (1992).

39. H. Hsieh, R. S. Averback, Phys. Rev. B. 42, 5365 (1990).

40. K. Nordlund, T.T. Järvi, K. Meinander, J. Samela, Appl. Phys. A. 91, 561 (2008).

41. K. Meinander, K. Nordlund, J. Keinonen, Nuclear Instruments and Methods in Phys. Research B. 242, 161 (2006).

42. K. Meinander, J. Frantz, K. Nordlund, J. Keinonen, Thin Solid Films. 425, 297 (2003).

43. L. B. Han, Q. An, S. N. Luo, W. A. Goddard, Materials Letters. 64, 2230 (2010).

44. T.T. Jarvi, A. Kuronen, K. Meinander, K. Nordlund, K. Albe, Phys. Rev. B. 75, 115422 (2007).

CHAPTER 2: Study of Deformation Mechanisms for Different Nanoparticle Sizes and Impact Velocities [1]

2.1: INTRODUCTION

A number of high-velocity aerosol processes have been developed over the past two decades for producing thick (1–100 μm) metallic and ceramic films. One of the more commonly used methods is cold-spray deposition [1, 2] where a powder is injected into a high-pressure gas and accelerated to high velocity through a nozzle. Polycrystalline films result when the particles impact onto a substrate. The aerosol deposition method is an alternative method for producing thick films [3–6] that utilizes particles that are accelerated from atmospheric pressure through a nozzle into vacuum. The impact velocities for both processes are similar, ranging from 300–1000 m/sec. However, the particle sizes are quite different: 0.1–0.4 μm for the aerosol deposition method and 5–40 μm for the cold-spray process. A third aerosol deposition process for producing thick films, the Laser Ablation of Microparticle Aerosols (LAMA) [7–9] process, utilizes similar impact velocities as both the cold spray and the aerosol deposition method, but employs even smaller nanoparticles (2–40 nm) in the aerosol.

Despite the similarities in the impact velocities between all of these aerosol processes, the final microstructures are dramatically different. For example, impact of micron-sized particles results in thick films that are nearly 100% dense and whose grains

[1] T.V. Chitrakar, J.W. Keto, M.F. Becker, D. Kovar, Acta Mater. 135, 252 (2017) (I performed the simulations, helped to analyze the results and helped to write the paper).

are heavily deformed along the impact direction. In contrast, films produced using the LAMA process are ≈ 70% dense and the grains are equiaxed [10]. This suggests that there are significant differences in the deformation mechanisms as the particle size is reduced from the micron-scale to the nano-scale.

TEM studies [11] and finite element simulations [12] have been used to understand the deformation and film formation mechanisms that occur when micron-sized particles impact a surface at high velocity, but there has been comparatively little work on understanding the deformation mechanisms that occur for smaller particles. The large local strain gradients, rapid cooling, and lack of constitutive property data for particles in this size range make it challenging to study nanoparticles (NPs) using experimental methods or continuum-based numerical modeling. Instead, molecular dynamics (MD) simulations have been utilized to study the final states after impact of NPs. For example, MD simulations have been used by Haberland *et al.* [13] to study the porosity of thin nanostructured films of molybdenum for a range of impact energies. Meinander and Nordlund [14] studied the density dependence of copper films on the impacting particle's size and energy. They also studied the effects of these variables on the morphology after impact of a single nanoparticle onto a substrate [15]. However, only the final film morphologies were emphasized, and there has been little consideration of the particle size and velocity dependent mechanisms of deformation that occur during and after impact.

Ogawa [16] studied the influence of particle velocity on single particle impact of 10 nm monoclinic zirconia particles over a range of velocities from 250–2,000 m/sec

using MD simulations. He observed no significant particle deformation for impact velocities below 1,000 m/sec, but above this velocity significant deformation occurred. At this velocity, discrete planar defects were observed that were hypothesized to be {100} <110> dislocations. At higher velocities, crystalline regions separated by regions of more complex defect structures were observed that exhibited lower degrees of crystallinity. Thus, Ogawa's study demonstrated that there are significant effects of particle velocity on deformation, but a detailed study of the nature of these defect structures and how they form were beyond the scope of his paper.

In this chapter, we study the deformation mechanisms that occur when a single silver NP impacts onto a silver substrate and seek to understand how these mechanisms influence the final nanostructure of the particle. We use classical MD simulations to study a range of NP sizes and impact velocities which match the experimentally accessible range of variables from the LAMA experiments. In the first part of the analysis, the final microstructure of the NPs and the conditions that lead to them are analyzed. In the latter part, the deformation and annealing mechanisms that lead to the observed final morphologies are studied.

2.2: PROCEDURE

LAMMPS (the Large-scale Atomic/Molecular Massively Parallel Simulator) was used to perform MD simulations of the impact of the Ag nanoparticles [17]. The

LAMMPS simulations were run in parallel by simultaneously solving the equations of motion of the atoms that interact with a pairwise potential on the Lonestar Linux cluster at the Texas Advanced Computing Center (TACC) at the University of Texas at Austin [18]. Two visualization packages, OVITO [19] and AtomEYE [20], were used to visualize atomic positions along planes of interest.

NPs were simulated in the size range of 2–9 nm (diameter) and the impact velocities ranged from 10–1500 m/sec. These ranges of sizes and velocities were selected because they represent the experimentally accessible ranges for NPs produced and impacted using the LAMA process [21]. The simulation volume was 60 × 60 lattice constants in the *x* and *y* directions (the lattice constant for silver is 0.409 nm), and 80 lattice constants in the NP impact (*z*) direction. The boundary conditions in all 3 directions were periodic. For smaller NPs, it was possible to simulate smaller volumes with a concomitant reduction in simulation times. However, a standard volume was adopted to accommodate the impact of the largest NPs to be analyzed. The substrate was located at the bottom of the simulation volume and extended 40 lattice constants in the *z* direction. Within the substrate, the *z* direction momentum in the bottom 5 atomic rows was fixed at zero during the simulation so that atoms would not move out of the simulation volume as a result of the momentum transfer from the impact. There was no thermal boundary condition set for the substrate base, and the substrate interface acted as a vacuum interface with respect to the periodic boundary condition imposed in the *z* direction.

The substrate was oriented such that the (100) and (010) faces were parallel to the simulation box, and the *z* axis was normal to the (001) face of the substrate such that it had the Miller indices *x* [100], *y* [010], *z* [001]. The substrate surface was oriented so that its surface was aligned along the reference *x* [100] and *y* [010] axes and the reference z [001] axis lay perpendicular to the substrate surface. The orientation of the impacting NP was defined relative to this reference axis. To consider a general case where the NP is misaligned relative to the substrate when the particle impacts, the NP was rotated by 45˚ about the *z* [001] axis with respect to the substrate surface prior to initiating motion of the NP. The orientation of this NP was defined by the Miller indices *x* [110], *y* [$\bar{1}$10], *z* [001]. Its orientation can also be represented by the Bunge notation of Euler angles as (22.5˚, 0˚, 22.5˚) [22] with respect to the fixed substrate surface orientation.

For the simulations, the Ag atom interactions were described using the embedded-atom method (EAM) potential [23, 24] obtained from the NIST Interatomic Potentials Repository Project [25]. To initiate the simulation, a spherical nanoparticle was placed near the center of the simulation volume at a height of 20–25 lattice constants above the substrate surface. Although Wulff polyhedra [26] are the equilibrium shapes for nanoparticles, nanoparticles produced by LAMA are generally spherical, and thus spherical nanoparticles were selected for these simulations [8]. The silver atoms in the substrate and the nanoparticle were then thermalized at room temperature (300 K, to emulate the experimental conditions for LAMA) for 30–40 ps, depending on the nanoparticle size. The time integration and equilibration of the system to 300 K were performed with a time step of 0.001 ps (1 fs) using Nose-Hoover style, non-Hamiltonian

equations of motion on the isothermal-isobaric (npt) ensemble [27], which generated positions and velocities of the atoms at every time step. This integrator was configured to incorporate a thermostat to a 300 K bath. The time constant for temperature dissipation to the bath was selected to give reasonable cooling times (~500 ps) for the substrate, which was much longer than the NP thermalization times of less than 50 ps.

Following the thermalization, a constant velocity was imparted to all atoms in the NP. During this stage of the simulation, the angular momentum for all atoms in the nanoparticle were zeroed at every time step in order to prevent rotation of the particle during flight. Upon impact, the atomic positions were output to a file for subsequent analysis at time steps of every 0.5 to 1 ps for the first 5 to 20 ps after impact and then every 20 to 30 ps for the remaining 300 to 1000 ps. The relaxation time for all nanoparticles to reach their final states ranged from 300 to 1000 ps, depending on the size of the NP.

For some simulations, the atomic positions were post-processed [28] to find the bond order parameter, q6 [29], in order to obtain information about the local atomic order and to identify atomic-scale defects. For figures in which the q6 parameter is displayed, the magnitude of q6 is quantified by the color of individual atoms. Representations of the bond order parameter, q6, were obtained for the short times only. For reference, an ideal FCC crystal has a q6 value of 0.575, an ideal HCP crystal has a value of 0.485, and disordered atoms/amorphous materials have lower q6 values of between 0.1–0.2 [30].

We initially conducted MD simulations of a single NP impacting the Ag (001) surface at a range of velocities and NP diameters in order to study how these parameters

influence the resulting film morphologies. A summary of the NP sizes and their impact velocities that were used is presented in Table 2.1.

NP size in diameter (nm) (Equivalent number of atoms)	Impact Velocity (m/sec) (Impact Kinetic energy (eV/atom))
2 (249)	10 (5.6×10^{-6})
3 (844)	100 (5.6×10^{-3})
4.5 (2859)	300 (5.0×10^{-2})
6 (6787)	600 (0.20)
9 (22610)	900 (0.45)
	1200 (0.80)
	1500 (1.30)

Table 2.1: Nanoparticle sizes (and equivalent number of atoms) and their impact velocities (and equivalent kinetic energies) that were studied.

2.3: RESULTS

Final Morphologies

The final morphologies that were observed after impact of an Ag NP onto a substrate at the ranges of particle sizes and impact velocities that were studied can be broadly classified into three categories:

a) Polycrystalline structures in which the initially single-crystal particle and substrate contain multiple grains following impact (p).

b) Monocrystalline structures where both the particle and substrate acquire the same orientation and are thus epitaxial, but where defects are present (ed).

c) Monocrystalline structures in which particle and substrate are epitaxial and where no defects are present (e).

Representative examples of particle impact events that resulted in each of the three categories are shown in Fig. 2.1.

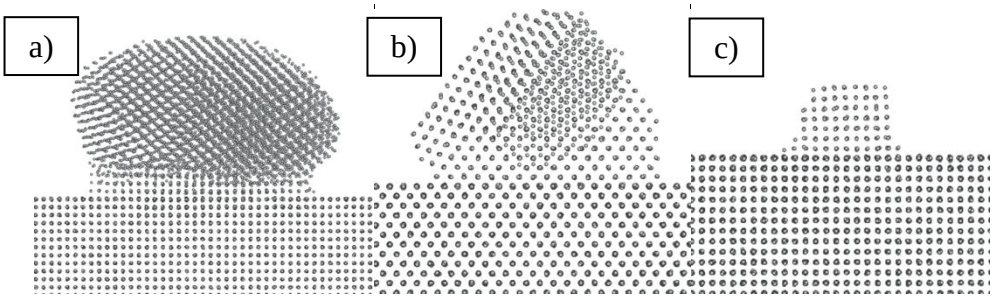

Figure 2.1: Representative final morphologies: a) Polycrystalline morphology (6 nm NP impacted at 300 m/sec), b) epitaxial morphology with defects present (4.5 nm NP impacted at 300 m/sec), and c) epitaxial morphology with no defects (2 nm NP impacted at 100 m/sec).

The final states from simulations for a range of particle sizes and impact velocities are shown in Table 2.2. Letter symbols are used to represent the final equilibrium morphology predicted from the simulation for each case of nanoparticle size and velocity. The number to the right of each symbol is the aspect ratio of the NP following impact. The aspect ratio, which is a measure of the deformation that occurs upon impact, is defined as the ratio of the largest width of the nanoparticle measured parallel to the substrate to its maximum height measured perpendicular to the substrate. Thus, aspect ratios near 1 represent morphologies in which minimal deformation occurred upon impact, whereas aspect ratios much larger than 1 represent significant deformation.

	Velocity (m/sec)						
Particle diameter (nm)	10	100	300	600	900	1200	1500
2	ed 1.7	ed 1.3	e 1.7				
3	ed 1.4	ed 1.1	e 1.7	e 3.4	e 2.7		
4.5		p 1.2	p/ed* 1.5	ed 2.0			
6			p 1.7	p 1.9	e 2.7		
9			p 1.5	p 2.0	p 2.9	e 4.3	e 7.9

**Simulations produced two different results when repeated.*

Table 2.2: Final morphologies as a function of particle size and impact velocity. Each cell in the table contains a letter and a number. The letter(s) defines the final state: polycrystalline morphology (p), epitaxial morphology with defects (ed), or epitaxial morphology with no defects (e). The number that follows is the final aspect ratio of the NP.

From Table 2.2, several general trends are apparent. For the smallest particle sizes, epitaxial morphologies (with or without defects) result for all impact velocities that were studied. For particles in this size regime, at velocities of 10 and 100 m/sec, defects were present. However, at the highest velocity (300 m/sec), the particle and substrate were epitaxial and free of defects. For particles with a diameter 4.5 nm and larger, low velocity impact produces a polycrystalline structure. For these sizes, a particle size-dependent transition from a non-epitaxial polycrystalline morphology to an epitaxial morphology was observed when the impact velocity was increased. Also, for a given impact velocity, a transition was observed as the particle size was increased from an epitaxial morphology to a non-epitaxial polycrystalline morphology. For example, for an impact velocity of 300 m/sec, the transition from epitaxial to non-epitaxial impact occurred at a particle size of

4.5 nm. Moreover, as the particle size was increased, the impact velocity required to transition from polycrystalline to epitaxial deposition increased. Thus, although the transition from polycrystalline to epitaxial deposition occurred at 300 m/sec for the 4.5 nm particle, velocities of 600–900 m/sec were required for 6 nm particles, and velocities of 900–1200 m/sec were required for 9 nm particles for the transition to occur. The aspect ratios of the impacted particles did not appear to be strongly dependent on particle size, but increased significantly with impact velocity. For example, the aspect ratios ranged from slightly greater than 1 for particle velocities up to 100 m/sec to nearly 8 for the highest impact velocity (1500 m/sec). Note that because statistical fluctuations are intrinsic to these types of simulations, there are small anomalies apparent in the trends in the aspect ratio. For example, the aspect ratio for 3 nm particles impacted at 10 and 100 m/sec is slightly higher at the lower velocity. Nevertheless, these variations were small relative to the broader trends that were apparent with increasing impact velocity and particle size.

These results show that the final morphologies following impact depend strongly on the impact parameters. However, understanding the deformation mechanisms and the evolution of the particle and substrate morphology that occurs during impact requires an examination of the dynamic behavior of the impact events at short time scales.

Dynamic Analysis of Particle Impact

The dynamic analyses were conducted using MD simulations and focused on four representative cases of NP sizes and impact velocities that illustrate the breadth of

possible final states that were observed. The goals were to study the range of deformation and annealing behaviors that occur when NPs impact, deform, heat, and then cool back to room temperature.

Case 1: 4.5 nm particle impacting at 100 m/sec

Referring to Table 2.2, we note that a polycrystalline morphology was obtained as the final state of the nanoparticle when a 4.5 nm NP impacted at a velocity of 100 m/sec. For the dynamic analysis, snapshots were taken at time intervals to study deformation mechanisms, as shown in Fig. 2.2(a-g). These images show the atomic positions, with the color of the atoms representing the magnitude of q6. In Fig. 2.2, the cross-section of the particle is 6 atomic layers thick, and the viewing axis is oriented along the [110] direction of the NP unless otherwise noted in the figure caption. There is a slight clockwise rotation of the NP about the axis of view (~5˚) from the intended impact orientation due to thermal fluctuations that occur while the NP is in flight and before impact. Only the top (001) planes of the substrate are presented for clarity.

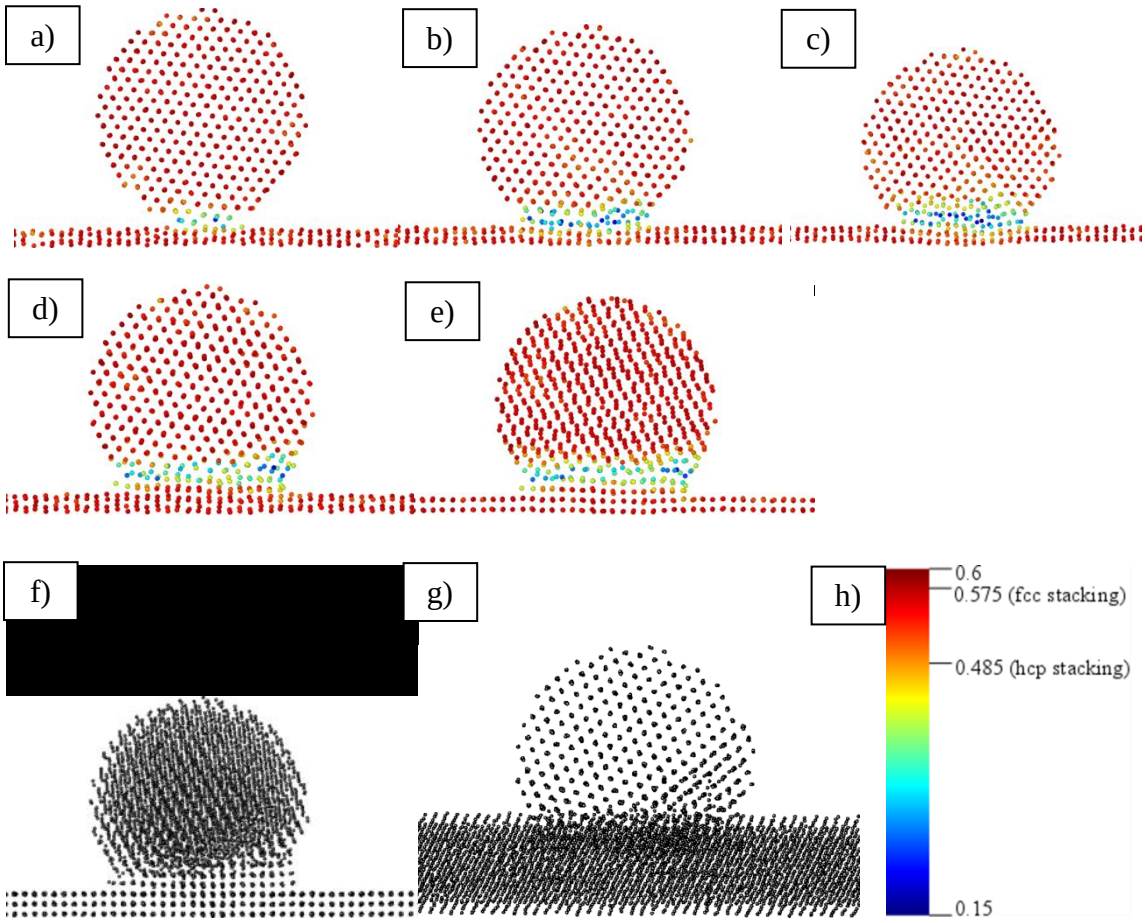

Figure 2.2: Cross-sections for a 4.5 nm NP impacted at 100 m/sec with the atomic positions and q6 values shown at times: a) 1 ps, b) 4 ps, c) 6 ps, and d) 16 ps after impact. In e) the NP is viewed at 16 ps along the [010] direction of the substrate. Atomic positions at 320 ps after impact are viewed along the [010] direction in the substrate in f) and along the [110] direction in the nanoparticle in g). The aforementioned two views are rotated by ~15^0 about the [001] axis with respect to each other. h) shows the scale used to represent the q6 values.

This sequence of events shows that, upon impact, the bottom 2–3 rows of atoms that are perpendicular to the impact direction in the NP initially disorder (Fig. 2.2(a)). This is confirmed by the change in color of these atoms from red (FCC) to blue (disordered). After 4 ps, the center of mass of the NP has moved further down, and the

number of disordered atoms has increased. In addition, the top few layers of the substrate are visibly compressed (Fig. 2.2(b)). After 6ps (Fig. 2.2(c)), the disorder has spread upwards by an additional 1–2 atomic layers. However, the upper part of the NP retains its pre-impact orientation and remains ordered with its original FCC structure.

The top of the NP has stopped moving 16 ps after impact (Fig. 2.2(d)). The elastic deformation that was visible in the substrate at earlier time steps has now relaxed, and the 2–3 atomic layers in the NP that were initially disordered have recrystallized with the same orientation as the substrate (Fig. 2.2(e)). Closer inspection shows that the atoms in the second epitaxial layer are located at approximately periodic positions indicating that the disorder has been largely eliminated, although they continue to exhibit a depressed q6 parameter (are bluer) relative to an FCC lattice.

Comparing the final state at 320 ps with the previous state at 16 ps, it is apparent that the grain boundary that was present between the substrate and the NP at earlier times has moved upwards, consuming the region that was previously disordered. This results in a polycrystalline final morphology where a single grain boundary separates the epitaxial layers of NP atoms that have grown from the substrate and the rest of the NP (Fig. 2.2(f)). A defect is also visible in the lower right corner that originated from the surface and propagated into the NP, propagating into the region that was initially disordered, and creating a stacking fault (Fig. 2.2(g)).

Case 2: 4.5 nm particle impacting at 300 m/sec

Referring to Table 2.2, we note that impact of a 4.5 nm NP at 300 m/sec results in a final state consisting of either a polycrystalline or epitaxial morphology with twins. Statistical fluctuations were evident upon repetition of the simulations, suggesting that either final state can result. Similar to the previous case, snapshots were taken at time intervals, as shown in Fig. 2.3(a-l). Again, the viewing direction is [110] in the NP unless otherwise noted, and a similar rotational misorientation (~5˚) from the intended impacting orientation is observed.

Similar to the previous case, at early times, the bottom 2–3 layers of atoms in the NP initially disorder (Fig. 2.3(a)) while the rest of the NP maintains its original FCC stacking while deforming. As the NP moves downwards, more atoms disorder. After 2 ps (Fig. 2.3(b)), a pyramidal feature appears within the NP directly above the contact zone between the NP and substrate. The angle at the apex of the pyramid is 70.5˚ which is the angle of intersection between two intersecting {111} planes. Looking down from the top of the NP along the impacting axis (Fig. 2.3(c)), we note that the pyramid boundary is formed by the intersection of four {111} planes, which is evident from the symmetric atomic displacements along the four <110> directions. In addition, we observe symmetric atomic displacements in four <100> directions at 45˚ between each of the intersecting {111} planes, which results in the observed 8-fold octagonal symmetry in the displacements of the atomic positions. While the pyramid is forming, atomic planes in the top part of the NP are visibly bent about the pyramid apex. The pyramidal feature and the

bending of atomic planes were not observed in case 1, but the elastic deformation of the substrate observed in case 1 is also evident in case 2.

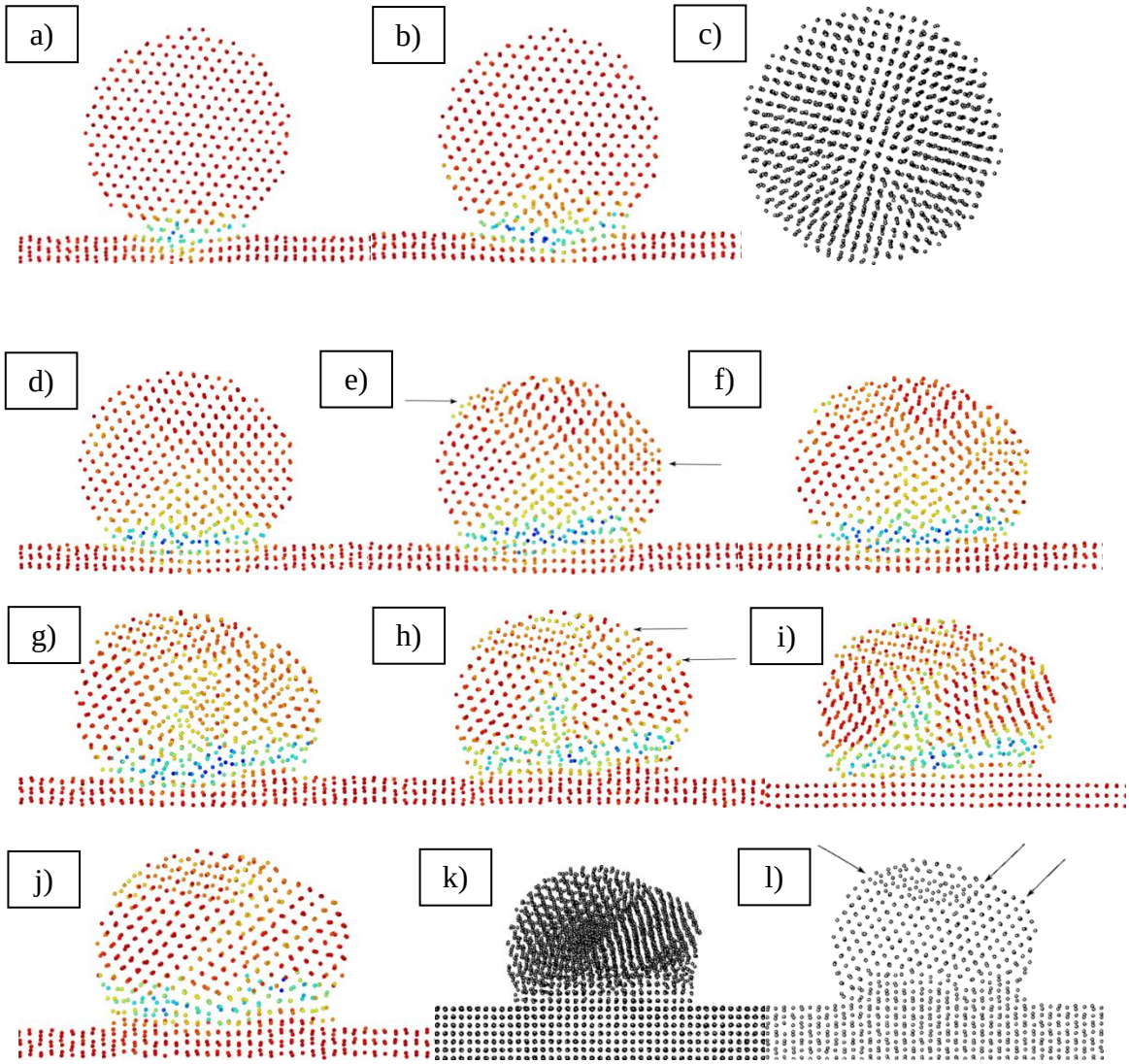

Figure 2.3: Cross-sections of a 4.5 nm NP impact at 300 m/sec. Atomic positions and q6 values are shown at a) 1 ps, b and c) 2 ps, d) 3 ps, e) 4 ps, f) 4.5 ps, g) 5.5 ps, h and i) 11.5 ps and j) 16 ps after impact. In c) a top view of the NP viewed along the impacting axis is shown at 2 ps, and in i) the impact event is viewed at 11.5 ps but along the [010] direction of the substrate. The final state at 320 ps after impact is viewed along the [010] direction in the substrate in k), and is rotated by ~ 45° about the [001] axis of the sustrate in l). Arrows in the latter image denote the locations of partial dislocations.

At 3 ps following impact (Fig. 2.3(d)), the pyramid has grown by 2 atomic layers along the <111> axes associated with the pyramid boundaries. Though the top part of the NP is still moving downward, the NP reaches its maximum area of contact with the substrate, and the bending of the atomic planes in the upper part of the NP has increased. At 4 ps after impact (Fig. 2.3(e)), the pyramid has grown by 2 more atomic layers and reaches its maximum size. The pyramid appears to be rigid as evidenced by the bending of the lattice planes about the pyramid apex as the upper portion of the NP is driven down towards the pyramid. However, the bending of the upper planes is reduced by the nucleation of two partial dislocations (arrows in Fig. 2.3(e)). The disorder near the contact patch has increased compared to early time steps and spread 2–3 atomic layers further into the NP.

At 4.5 ps (Fig. 2.3(f)), the partial dislocations have propagated towards the center of the NP. The pyramid has started to distort from the momentum of the deforming top part of the NP, and its apex angle has increased to greater than the expected value of 70.5˚. This distortion of the pyramid continues for another 1 ps (Fig. 2.3(g)), after which the top part of the NP stops deforming and the NP reaches a state of maximum deformation. The region of disorder inside the pyramid has reached its maximum size. A small region of atoms on the left side of the NP retains its original orientation with an FCC structure, while the rest of the NP has rotated about the pyramid apex.

Near the center of the NP and directly above the impact zone, atoms that were previously disordered have started to recrystallize and relax to an FCC structure 11.5 ps after impact (Fig. 2.3(h)). The disorder near the center of the NP further decreases, and

two annealing partial dislocations form near the surface of the NP and propagate into region that was previously disordered (arrows in Fig. 2.3(h)). Similarly to case 1, two layers of atoms that grew epitaxially from the substrate surface are apparent (Fig. 2.3(i)), but they have not yet relaxed completely to an FCC structure. At 16 ps after impact (Fig. 2.3(j)), the disorder decreases further, and most of the atoms have relaxed significantly. By 320 ps after impact (Fig. 2.3(k)), the NP reaches its stable state and the grain boundary has moved a few more atomic layers upwards. The NP now has a polycrystalline morphology like case 1, but it contains a number of partial dislocations in different {111} planes. An example is shown in Fig. 2.3(l) of a cross-section taken near the center of the NP showing two parallel partial dislocations and a third partial dislocation in the upper left corner that is not in the same plane. Closer inspection of Figs. 2.3(k) and (l) show that the final state is characterized by a large number of parallel and non-parallel stacking faults caused by the presence of partial dislocations.

Case 3: 6 nm particle impacting at 600 m/sec

Referring to Table 2.2, we note that impact of a 6 nm NP at a velocity of 600 m/sec results in a polycrystalline morphology. The simulation conditions were maintained and a rotational misorientation of ~5˚ was again observed, similar to the previous cases. Snapshots were obtained at intervals shown in Fig. 2.4(a- f), and only grey-scale atom position images are presented because q6 is difficult to interpret with the increased number of defects that are present in this case.

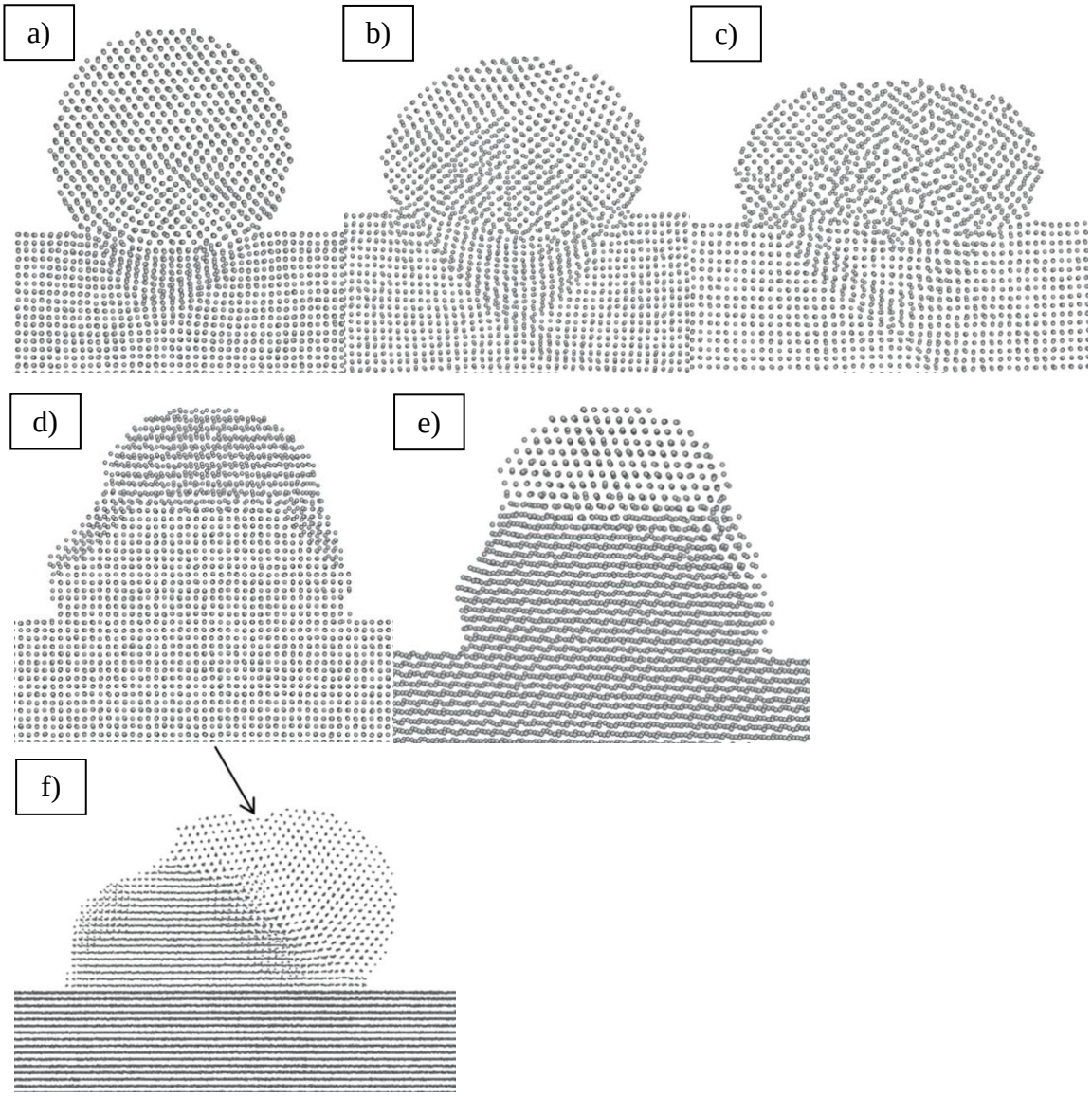

Figure 2.4: Cross-sections for a 6 nm NP impact at 600 m/sec. The sections are 5 atoms thick for a-e) and 7 atoms thick for f), taken at the center of the NP. Atomic positions are captured at a) 0.5 ps, b) 1.5 ps, c) 2.5 ps and d-f) 600 ps. The viewing direction is oriented along the [110] axis for the NP and the [010] axis for the substrate in a-c); d-f) show the final morphology of the NP where d) and e) are seperated by a rotation of 27˚ about the impact axis. f) is rotated 90° about the [001] axis of the substrate from d), and an annealing partial dislocation in the upper grain of the NP is marked with an arrow.

Just after impact (Fig. 2.4(a)), a pyramidal feature similar to case 2 is observed in the NP, along with a larger compression of the substrate. In this case, a symmetrically opposite pyramid is also observed in the substrate directly below the contact zone. After 1.5 ps, the pyramid within the NP has grown, and several layers of atoms in this region near the contact patch start disordering (Fig. 2.4(b)). The top rows of atoms in the substrate are bent more than in case 2, and the pyramid in the substrate has grown, but has not disordered. At 2.5 ps after impact (Fig. 2.4(c)), the regular periodicity within the upper pyramid is lost and only two regions on the left and the right of the NP remain crystalline. Even these crystalline regions, however, contain several partial dislocations that were intiated 1 ps earlier due to the highly strained lattice caused by the relative upward motion of the pyramid and the resulting bending of atomic rows. Unlike case 2, where a few partial dislocations were observed in the first 10 ps following impact, at this higher impact velocity, the density of partial dislocations is much higher. After the NP has relaxed for 600 ps, the disordered atoms in Fig. 2.4(c) recrystallize from the substrate upwards creating a polycrystalline morphology (Fig. 2.4(d and e)) with a defect-free lower grain and an upper grain containing partial dislocations (Fig. 2.4(f)). In summary, the observed deformation mechanisms for case 3 are similar to case 2 and lead to a similar final morphology. However, the number of partial dislocations is increased and results in a larger number of stacking faults in the final morphology.

Case 4: 4.5 nm particle impacting at 600 m/sec

For case 4, the impact velocity is increased by a factor of two compared to case 2 and the particle size is decreased from a diameter of 6 nm to 4.5 nm compared to case 3. From Table 2.2, it is apparent that the final state for this case is epitaxial. The simulation conditions and the rotational misorientation prior to impact were similar to case 3, and again only grey scale images are presented due to the large number of defects that are present.

Figure 2.5(a-c) suggests that the same deformation mechanisms are operating for this case as observed in case 3. In particular, the initiation and propagation of the pyramid, significant bending of atomic rows at the top of the NP, elastic deformation and relaxation of the substrate, and a highly defected upper region of the NP are also visible. However, it is apparent that, by 4.5 ps (Fig. 2.5(d)), nearly the entire NP except the very top part disorders. This degree of disorder was not observed in any of the previous cases. With increased time, the grain boundary separating the NP and the substrate continues to grow (Fig. 2.5(e)), and the bottom 4–5 atomic rows within the NP have recrystallized epitaxially from the substrate. The grain boundary continues to move upward until it consumes the entire disordered NP. At 320 ps after impact (Fig. 2.5(f)), a monocrystalline morphology of the NP is present where both the substrate and the NP have the same crystallographic orientation. Three non-parallel annealing partial dislocations have formed during relaxation near the surface of the NP. Thus, the final state of the system is a monocrystalline morphology containing defects.

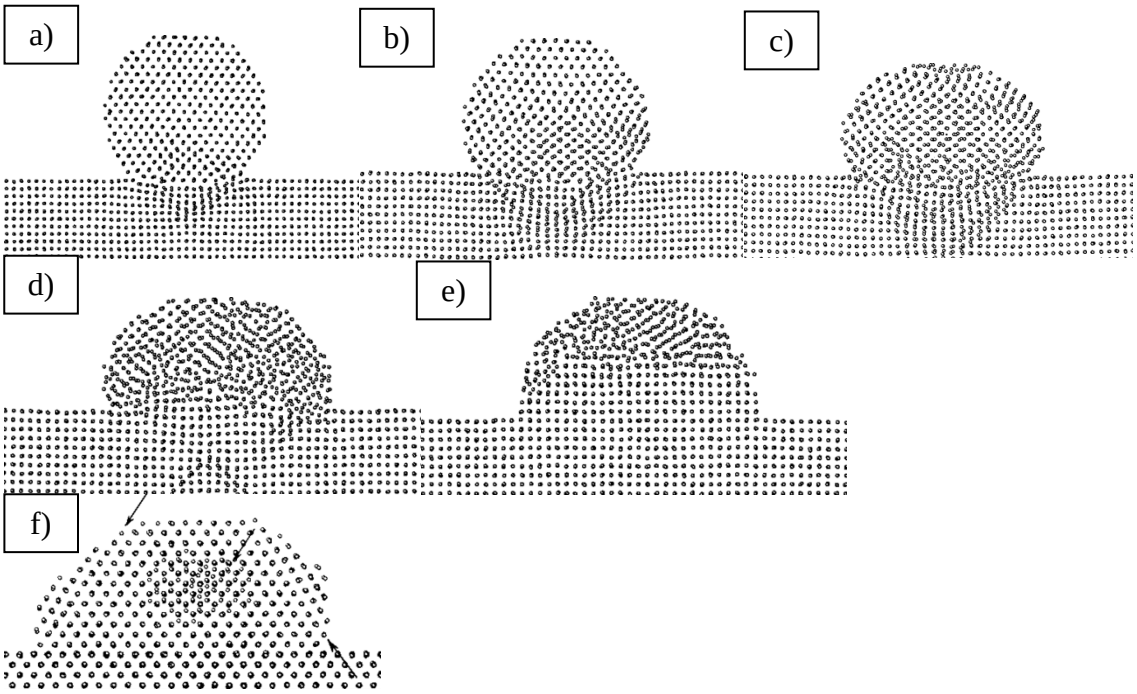

Figure 2.5: Cross-sections for a 4.5 nm NP impact at 600 m/sec. The sections are 6 atoms thick taken at the center of the NP. Atomic positions are captured at a) 0.5 ps, b) 1.5 ps, c) 2.5 ps, d) 4.5 ps and e) 17.5 ps after impact. The orientation of the final state at 320 ps after impact is shown with respect to the [110] direction in the substrate in f), and the partial dislocations near the surface of the NP are highlighted with arrows.

2.4: DISCUSSION

Temperature rise upon impact and surface energy effects

One logical variable to consider when considering the major factors that determine the final outcomes of impact is the NP energy and the resulting temperature increase that arises from the conversion of linear kinetic energy of motion to energy distributed among

the vibrational and electronic modes of the material. We will first consider the magnitude of the temperature rise and show that the impact energy is not sufficient to predict the variety of final states from a NP impact that were observed in the simulations.

The temperature reported by LAMMPS includes all motional energy, linear and random, and the linear velocity of the NP before impact is thus reported as a temperature (for example, 3800 K for 900 m/sec, 1820 K for 600 m/sec, etc.). Thus, temperature distributions in the NP during impact were examined after all linear motion of the NP had stopped in order to estimate a maximum temperature rise within the NP. Temperature in the NP was averaged within atomic layers in the NP that were parallel to the substrate surface. The thickness of each layer of atoms used for the averaging was about 20% of the diameter of the NP. This is reasonable since the thermal distribution for the first few ps is roughly one-dimensional.

The following caveats apply to this interpretation of temperature derived from MD simulations. In addition to the inexact mapping of MD-simulated temperature to temperature measured in physical experiments, the maximum local temperature may be underestimated due to the time required for all linear NP motion to cease and due to the temperature averaging by layers. On the other hand, the temperature may be overestimated because LAMMPS does not consider electronic thermal conduction, a significant factor in crystalline metals. For the case of NP impact, we see that the lattice planes, especially in the NP, become distorted and disrupted in less than a few ps. The electron-phonon scattering time is also in this time range, 1–3 ps for nano-gold and silver [31, 32]. Although there is some delay in energy transfer to the electrons, increased

electron-defect scattering would greatly decrease the electronic conductivity in the NP. In the presence of these counteracting factors, we assume that the reported MD temperatures nominally represent the maximum temperature reached during the impact event at a time when the deformation rate is greatest.

With these caveats, the nominal maximum temperatures for the cases from Table 2.2 are plotted in Fig. 2.6 versus impact energy, with NP diameter as a parameter. The data are self-consistent and show the expected linear dependence of temperature rise on kinetic energy. However, there is no consistent dependence on NP diameter, and therefore the different observed final outcomes for different NP diameters cannot be ascribed to the effect of temperature rise alone.

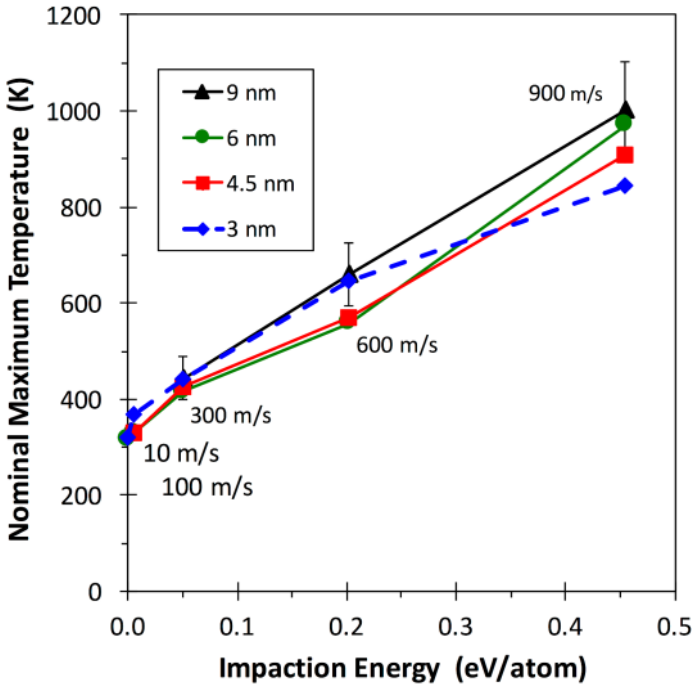

Figure 2.6: Nominal maximum temperature rise in the NP versus impact energy with NP diameter as a parameter.

Another feature observed in Fig. 2.6 is that for an impact velocity of 10 m/sec, there is a temperature rise of 20–40 K, which is much greater than the energy from the conversion of kinetic energy to heat. Extrapolation of the data to the zero-energy intercept also gives a temperature rise of this amount. Both of these results suggest that there is an excess energy beyond that from the kinetic energy that is a result of the release of surface energy that occurs upon impact. The temperature rise associated with the release of surface energy is particularly significant for the low-energy impact of small NPs ($\leq$ 3 nm). In these particles, the surface energy lost at the NP-substrate interface upon impact is stored in the form of a grain boundary between the substrate and the NP, and the grain boundary area-to-volume ratios are large for small particles. Thus, there is a large driving force to remove the grain boundary between the NP and substrate by migrating it completely out of the NP. A temperature rise of only a few tens of degrees is sufficient to facilitate the epitaxial growth observed for the low-energy impact of very small NPs.

Deformation Mechanisms

Another global variable that can be related to the final morphology after impact is the magnitude of the deformation experienced by the particle after impact. This is readily measured from the final aspect ratio. Aspect ratios for all the cases reported in Table 2.2 are plotted in Fig. 2.7 as a function of impact energy. Similar to the case of temperature rise, deformation scales roughly linearly with impact energy in this range of energies, but again there are no obvious correlations that would explain how NP diameter effects the

range of observed final morphologies.

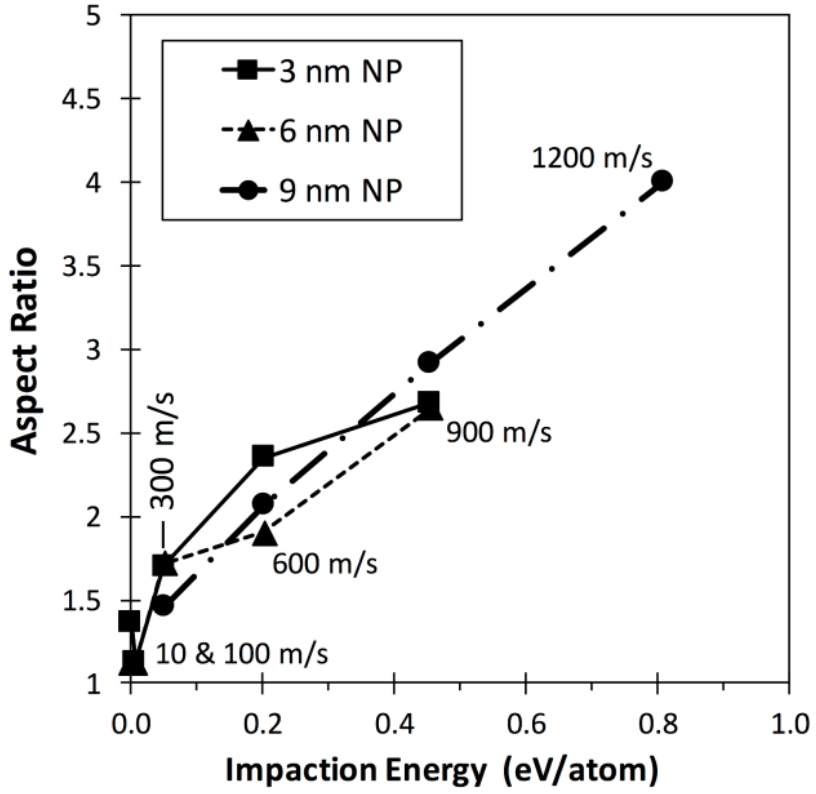

Figure 2.7: Total nanoparticle deformation as shown by final NP aspect ratio, (max width)/ (max height from substrate), versus impact velocity.

Since impact energy and deformation alone cannot predict final states, we now consider the role of deformation mechanisms on a case-by-case basis to illustrate how they can be used to distinguish the evolution and final states of the NPs during and after impact. For representative cases of impact velocity and NP diameter reported in the Results section, the corresponding deformation mechanisms were studied. Here we analyze these cases, looking for unifying themes and known mechanisms associated with deformation and recrystallization.

At low impact velocities (case 1), we observed a region of disorder near the contact patch between the NP and substrate where the atoms recrystallized epitaxially from the substrate. At these relatively low velocities, pyramidal structures were not observed in the NP or substrate, and the final polycrystalline morphology of the NP was only influenced by the disordering of the NP atoms close to the region of contact.

When the velocity was increased while maintaining a constant NP size, a pyramidal structure was observed that expanded with time. In case 2, the atomic rows that intersect the pyramid appear to have an orderly change in their q6 parameter as a function of position, which suggests that the pyramid is composed of line defects such as dislocations or twins. To identify the nature of the defects that form these pyramids, it is helpful to first review the nature of dislocations that typically occur in FCC crystals. The closed-packed planes along which slip occurs for FCC crystals are the {111} planes and the slip directions for perfect dislocations are the <110> directions, and thus perfect dislocations are of the type a/2 <011>. In some cases, it may be more energetically favorable for deformation to occur by motion of partial dislocations. Shockley partials of the type a/6 <112> are commonly observed in FCC crystals such as Ag. When a single Shockley partial dislocation propagates, a stacking fault is generated where the normal ABCABC stacking of {111} planes is disrupted by the absence of a single {111} plane. At the location of the stacking fault, the missing {111} plane results in a local region where the stacking is ABABC. The local region of ABAB stacking of {111} planes results in a hexagonally closed-packed (HCP) structure. If the leading Shockley partial dislocation is followed by slip of a trailing Shockley partial dislocation on the same plane, the overall

reaction is given by: $\frac{a}{6}[\bar{2}\,1\,1] + \frac{a}{6}[\bar{1}\,\bar{1}\,2] \rightarrow \frac{a}{2}[\bar{1}\,0\,1]$. Thus, the trailing partial restores the original ABCABC stacking of the FCC structure.

To understand the nature of the atomic arrangements in the vicinity of the pyramids, the q6 parameters were studied in greater detail. Fig. 2.8(a) shows the pyramid 2 ps after impact just as it is begging to expand. Lines have been used to highlight the pyramid edges and the region of sampling. Only atoms to the left of (and including) the upper line outside the pyramid, and all atoms within the pyramid are analyzed. An origin line, 0, is defined at the edge of the pyramid along one of the {111} planes. Fig. 2.8(b) was obtained 3 ps following impact after the pyramid has propagated upward by 2 atomic layers, but the reference 0 line remains at the same location where it was defined at the 2 ps time step. The numbering of each atomic row is defined with respect to the reference line along the corresponding <111> direction from the lower right to upper left. Atomic rows outside the pyramid are numbered with an increasing positive value starting from the reference line and moving up and left. The rows inside the pyramid are numbered with negative values, starting from the same reference line and moving down and right. In Fig. 2.8(b), lines are used to identify the reference line (the edge of the original pyramid in Fig. 2.8(a) at 2 ps) and the edge of the current pyramid at 3 ps. A plot of average q6 versus position along each row of atoms from the bottom left to the top right and parallel to the left edge of the pyramid is shown in Fig. 2.9. Averaging was carried out over all atoms having the same atomic row and position number.

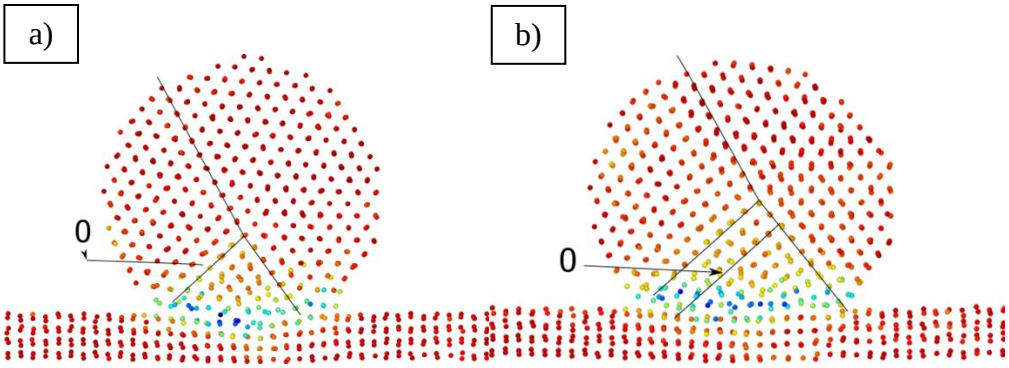

Figure 2.8(a-b): Representative images from case 2 to show the technique used to analyze the q6 values of the NP atoms; a) and b) are at 2 ps and 3 ps after impact respectively.

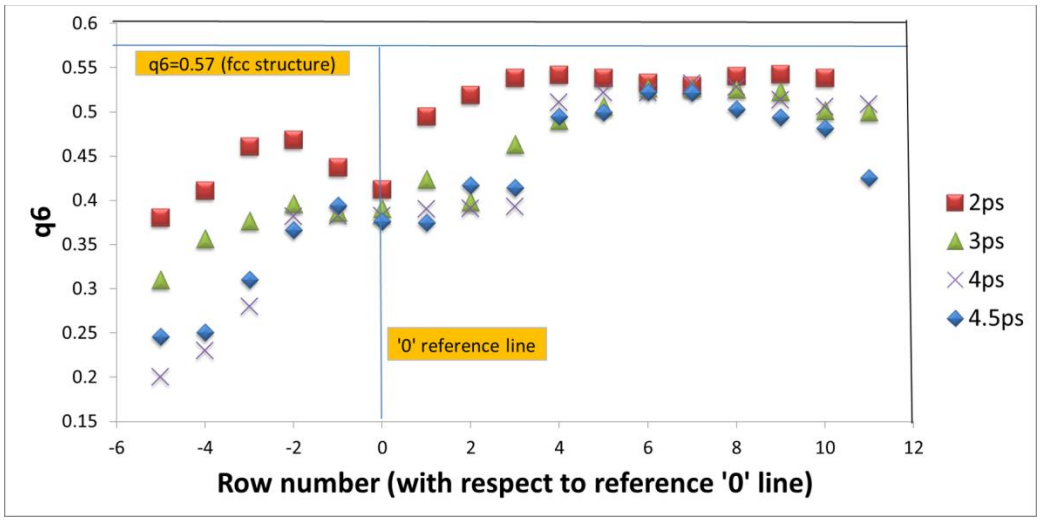

Figure 2.9: The average q6 parameters for each atom row versus row number are plotted for different time intervals after impact.

At 2 ps after impact, outside of the pyramid, we observe that the q6 values are ~0.55, which indicates that this region of the NP retains its original FCC structure. Due to thermal vibrations of the NP atoms at 300 K, the q6 values in this region are slightly lower than the theoretical value of 0.57 for a perfect FCC lattice. As the time after impact is increased, the q6 values in this region decrease slowly, but generally remain above

approximately 0.5. Comparison between Fig. 2.9 and Figs. 2.2–2.5 shows that this decrease results from an increase in the elastic bending of the top rows of the NP and from propagation of the deformation Shockley partial dislocations from the NP surface.

Moving across the pyramid edge to its interior, the q6 values decrease abruptly, as shown in Fig. 2.9. Due to growth of the pyramid, the row number corresponding to the pyramid edge at the step in the q6 values moves to a higher row number as time increases. The pyramid is observed to propagate upwards as it expands and the number of rows in the interior increases. For example, comparing Figs. 2.8(a) and (b), it is apparent that the pyramid has propagated upward by 2 atomic rows. This is also evident in Fig. 2.9, where the steep edge in the q6 values at 3 ps has shifted from row 0 to row 2. We observe relatively high q6 values inside the pyramid at 2 ps, and though this region is strained, it has not yet begun to disorder. The q6 values inside the pyramid continuously decrease with time due to the disorder that originates near the base of the pyramid and moves upwards into the pyramid body as time increases.

To better understand the nature of this pyramid and how it influences the disorder that is quantified using the q6 parameter, further analyses of the local atomic displacements in the vicinity of the pyramid were conducted by directly measuring the relative atomic displacements on either side of the pyramid surface. This analysis confirmed that each of these faces of the pyramid are a/6 <112> Shockley partial dislocations that lie in intersecting {111} planes. At the apex of the pyramid, the Shockley partial dislocations intersect. The intersection of Shockley partial dislocations has been shown previously to produce a/6 <011> sessile dislocations (e.g. Lomer-Cottrell

locks [33]), stair-rod dislocations, or other complex lock structures [34]. The formation of a lock prevents further motion of the a/6 <112> partial dislocations and thus the pyramid bounded by the Shockley partial dislocations acts like a nearly rigid wedge. When this wedge is driven upwards into the NP, the top planes of the NP bend, and the pyramid apex angle is increased by the local displacements of atoms in the NP. Partial dislocations are observed to initiate at the NP surface, and they propagate inward towards the pyramid. These are likely Shockley partial dislocations based on the observation of stacking faults in the wake of the moving dislocations. However, a quantitative analysis of displacement vectors in this region is not possible because of the superimposed large, non-uniform bending strain that is also present. Dislocations continue to nucleate and propagate until the pyramid has grown to its maximum size. Eventually, the top part of the NP stops moving, and the maximum deformation of the NP is obtained.

There are two sources of atomic disorder that were observed in the NPs upon impact: 1) near the contact zone between the NP and substrate and 2) outside of the pyramid. The disorder that is observed to initiate within the pyramid in the vicinity of the contact zone is likely driven by localized heating from the conversion of linear kinetic energy to heat as well as surface energy (Fig. 2.2). Outside of the pyramid, the process is more complex. For NPs impacted at moderate speeds, a small number of partial dislocations are initiated due to the wedging action of the pyramid (Fig. 2.3), but the extent of disordering outside of the pyramid is limited. However, as the impact velocity is increased, the number of dislocations increases (Fig. 2.4), and the probability that the dislocations lie on non-parallel planes increases dramatically. When the density of the

dislocations is very high (Fig. 2.5), it may not be possible to identify individual dislocations, and the NP therefore appears to be completely disordered. At a given impact velocity, increasing the NP size reduces the relative contribution of the surface energy effects, and thus larger particles require higher impact energies to disorder. Therefore, this transition from individual dislocation initiation at moderate impact velocities to complete disordering at higher velocities does not occur at a discrete velocity or particle size, but rather varies continuously from one mechanism to the other.

Although the boundary conditions fixed the bottom layers of the substrate, small displacements of the entire NP-substrate system were observed. This occurred only for the 4.5 nm particle and not the other smaller-sized particles because the larger particle had sufficient momentum transfer to the substrate upon impact to move the edges of the entire particle-substrate system slightly outside of the simulation volume. The effect of these displacements is to increase the effective compliance of the substrate. Increasing the effective compliance of the substrate may affect both the magnitude of the deformation experienced by the impacting particle and the substrate as well as the deformation mechanisms that are active.

Final Microstructure

For very small NPs (≤ 3 nm), it is possible to produce epitaxial deposition without significant deformation of the NP because the NP-substrate interactions are dominated by surface energy effects. However, as particle size is increased, the importance of deformation on the final microstructure becomes the key factor. Particles that do not

deform sufficiently to initiate partial dislocations result in a polycrystalline structure with a grain boundary located near the original NP-substrate interface. At higher impact velocities, a pyramid is formed by the intersection of Shockley partial dislocations on non-parallel planes. This intersection of partial dislocations results in a lock structure that causes the pyramid to act like a nearly rigid wedge that amplifies the deformation in the remaining regions of the NP. At higher velocities, the partial dislocations that initiate in these heavily deformed regions can reach sufficiently high densities so that the NPs appear completely disordered. Upon relaxation of these disordered regions, the recrystallization front can propagate completely through the particle, resulting in epitaxial deposition. In some cases, the resulting NP and substrate are not perfect single crystals because annealing stacking faults are produced during the rapid movement of the recrystallization front through these highly defective regions.

Previous experimental results for Ag NP deposition at impact velocities near the transition from polycrystalline to epitaxial deposition resulted in films with grain sizes of ~16 nm [8]. This is significantly larger than the impacting NP size, which had a mean diameter of 6 nm. These multi-particle impact experiments likely result in polycrystalline films despite the fact that the particles with the mean size are in a regime where epitaxial deposition is predicted because, at velocities near the transition, different impact conditions (NP size, velocity, and orientation) may not lead to epitaxial deposition for every NP deposition event. As a result, the grain size of the deposited films may be larger than the initial NP size, but the film will still not be entirely epitaxial because not every impact results in epitaxial deposition.

2.5: CONCLUSIONS

MD simulations of a single Ag NP impact were conducted for a range of NP sizes and impact velocities that match the experimentally accessible range of processing variables in the LAMA process in order to study the underlying deformation mechanisms and to observe how these mechanisms influence the final nanostructure of the particle and substrate. For very fine NPs (< 3 nm), the morphology was observed to be independent of particle velocity. In this size regime, the NP adopted the same orientation as the substrate, i.e., the final morphology was epitaxial. For particles larger than 3 nm, the final morphology was shown to depend on both the particle size and impact velocity. For a given particle size, a transition from polycrystalline to epitaxial monocrystalline morphology was observed as the particle velocity was increased and a corresponding increase in the final deformation of the particle was observed. For a given impact velocity, the transition from polycrystalline to epitaxial morphologies was observed to increase with particle size, but no significant differences were observed in the final global deformation of the particle.

To understand the deformation mechanisms and the evolution of the particle and substrate morphologies that occurred during impact, dynamic behavior was studied at short time scales. For particles impacting in the low velocity regime, atoms with the NP near the contact zone were observed to disorder. Subsequent recrystallization of this region resulted in a polycrystalline morphology with a grain boundary dividing an upper grain that retained its pre-impact orientation and the lower portion of the particle that

adopted the orientation of the substrate. In the moderate velocity regime, in addition to disordering near the contact zone, an octagonal pyramidal feature was observed to form from the contact zone by the intersection of Shockley partial dislocations along four intersecting {111} planes. The intersection of these partial dislocations produced a lock that effectively impeded further movement of the partial dislocations. As deformation proceeded, this pyramid acted like a nearly rigid wedge, causing very large strains to develop in the NP outside of the wedge. Non-parallel partial dislocations were observed to initiate from the NP surface which moved towards the pyramid in these regions of high strain. When the particles were impacted in the high velocity regime, a similar deformation mechanism was observed, but the density of partial dislocations increased multifold compared to the moderate velocity regime. The intersections of these partial dislocations in the high velocity regime produced such a high degree of disorder, that a crystal structure could not be identified in these regions. Upon relaxation, the atomic structure in the NP was found to adopt the same orientation as the substrate; e.g., an epitaxial monocrystalline morphology was obtained.

This work shows that a wide range of morphologies are possible when NPs impact onto a substrate. Specific defect mechanisms oriented within {111} planes have been identified to occur during impact. Here we have explored the effects of particle size and velocity for single particle impacts, but we have not considered other variables such as particle misorientation relative to the substrate and defects present in the NP prior to impact, that may influence deformation mechanisms and final particle morphology. In addition, to understand film-formation mechanisms, multiple particle impacts must also

be studied. Thus, not only is careful control of aerosol deposition processing parameters required to allow the deposition of films with the desired grain size and orientation, but knowledge of all possible impact outcomes is required as well. Further exploration of the entire ensemble of NP impact conditions is needed to understand and model the experimental film deposition process.

2.6: REFERENCES

1. T. Stoltenhoff, H. Kreye, H.J. Richter, J. Therm. Spray Tech. 11, 542 (2002).
2. T. Stoltenhoff, H. Kreye, H.J. Richter, H. Assadi, in: Thermal Spray 2001 New Surfaces for a New Millennium: Proceedings of the International Thermal Spray Conference. (May 28-30, 2001) p: 409.
3. J. Akedo, M. Ichiki, K. Kikuchi, R. Maeda, Sensors and Actuators A: Physical. 69, 106 (1998).
4. J. Akedo, M. Lebedev, S. Nakano, H. Ogiso, Ceram. Eng. Sci. Proc. 24/3, 9 (2003).
5. A. Schroth, R. Maeda, J. Akedo, M. Ichiki, Jpn. J. Appl. Phys. 37, 5342 (1998).
6. M. Lebedev, J. Akedo, T. Ito, J. Cryst. Growth. 275, 1301 (2005).
7. W.T. Nichols, J.W. Keto, D.E. Henneke, J.R. Brock, G. Malyavanatham, M.F. Becker, H.D. Glicksman, Applied Physics Letters. 78, 1128 (2001).
8. C. Huang, W.T. Nichols, D.T. O'Brien, M.F. Becker, D. Kovar, J.W. Keto, J. Appl. Phys. 101, 064902 (2007).
9. M. Nahar, J. W. Keto, M. F. Becker, D. Kovar, Journal of Electronic Materials. 44/8, 2559 (2015).
10. C. Huang, M. F. Becker, J. W. Keto, D. Kovar, J. Appl. Phys. 102, 054308 (2007).
11. C. Borchers, F. Gartner, T. Stoltenhoff, H. Assadi, H. Kreye, J Appl Phys. 93/12, 10064 (2003).
12. B. Yildirim, S. Muftu, A. Gouldstone, Wear. 270, 703 (2011).
13. H. Haberland, Z. Insepov, M. Moseler, Phys. Rev. B. 51, 11061 (1995).
14. K. Meinander, K. Nordlund, Phys. Rev. B. 79, 235431 (2009).
15. K. Meinander, K. Nordlund, J. Keinonen, Nuclear Instruments and Methods in Phys. Research B. 242, 161 (2006).
16. H. Ogawa, J-Stage Mat. Transactions. 46/6, 1235 (2005).
17. S. Plimpton, J Comp Phys. 117, 1 (1995) (http://lammps.sandia.gov).
18. Lonestar Linux Cluster, TACC (http://www.tacc.utexas.edu).
19. A. Stukowski, Modelling Simul. Mater. Sci. Eng. 18, 015012 (2010).

20. J. Li, Modelling Simul. Mater. Sci. Eng. 11, 173 (2003) (http://mt.seas.upenn.edu/Archive/Graphics/A).
21. W.T. Nichols, G. Malyavanatham, D.E. Henneke, J.R. Brock, M.F. Becker, J.W. Keto, H.D. Glicksman, J. Nanoparticle Research. 2, 141 (2000).
22. O. Engler, V. Randle, *Introduction to Texture Analysis: Macrotexture, Microtexture and Orientation Mapping* (CRC press, Taylor and Francis Group, Boca Ration, Florida, USA, 2010).
23. M. S. Daw, M. I. Baskes, Phys. Rev. Lett. 50, 1285 (1983).
24. M. S. Daw, M. I. Baskes, Phys. Rev. B. 29, 6443 (1984).
25. P.L. Williams, Y. Mishin, J.C. Hamilton, Modelling Sim. Mater. Sci. Eng. 14, 817 (2006) (http://www.ctcms.nist.gov/potentials/Ag.html).
26. J. E. Hearn, R. L. Johnston, J. Chem. Phys. 107, 4674 (1997).
27. W. Shinoda, M. Shiga, M. Mikami, Phys Rev B. 69, 134103 (2004).
28. Y. Wang, S. T. C. Dellago, J. Chem. Phys. 122, 214722 (2005).
29. P. J. Steinhardt, D. R. Nelson, M. Ronchetti, Phys. Rev. B. 28, 784 (1983).
30. J. Song, D. J. Srolovitz, Acta Materialia. 55, 4759 (2007).
31. S. Link, C. Burda, Z. L. Wang, M. A. El-Sayed, J. Chem. Phys. 111, 1255 (1999).
32. W. Huang, W. Qian, M. A. El-Sayed, Y. Ding, Z. L. Wang, J. Chem. Phys. C Lett. 111, 10751 (2007).
33. D. Hull, D.J. Bacon, *Introduction to Dislocations* (Butterworth-Heinemann, Oxford, GB, 2011).
34. A. Tolvanen, K. Albe, Beilstein J. Nanotechnol. 4, 173 (2013).

CHAPTER 3: An Experimental and Computational study of High Speed Two-Particle Impacts of Ag Nanoparticles [2]

3.1: INTRODUCTION

Thick films are produced via several related aerosol-based manufacturing processes by impacting particles onto a substrate at high velocity (300–1,000 m/sec). A distinguishing characteristic between these manufacturing processes is the significant differences between the particle sizes of the impacting particles. The cold spray process utilizes 5–40 μm particles to produce thick films over large areas [1–3], whereas the aerosol deposition method (ADM) has been developed to deposit finer 0.1–0.4 μm particles into patterned thick films [4, 5]. We have developed the laser ablation of microparticle aerosol process (LAMA), where even finer 2–40 nm nanoparticles (NPs) are impacted to produce patterned, microscale thick films [6–8].

It has been previously established that dislocation plasticity plays a large role in the impact deformation and resulting film microstructures for deposition of micron-sized particles such as those used in cold spraying [2, 3, 9, 10]. However, there is less understanding of the deformation and film formation mechanisms for finer particles at similar impact velocities. Empirical evidence and a theoretical basis suggest that the deformation behavior of finer particles is considerably different from that of larger

[2] T.V. Chitrakar, G. J. J. Noiseau, J.W. Keto, M.F. Becker, D. Kovar, J. Appl. Phys. 125, 195104 (2019) (I performed the simulations, helped to analyze the simulation results and helped to write the paper)

particles [3, 11]. One reason for this is that a critical particle size exists below which glissile dislocations are not stable, and thus dislocations in very fine NPs may spontaneously move to the NP surface, where they are annihilated, leaving dislocation-free or nearly dislocation-free NPs [12]. Plasticity in dislocation-starved NPs is dependent on dislocation nucleation, which requires higher stresses than dislocation propagation from pre-existing dislocations [13].

Further indirect support for size-dependent impact behavior is evident in the experimental work of Akedo *et al.* [14], who observed that particles with an initial size of 120 nm produced relative film densities for Ag of 85–90%, which is considerably lower than observed for films produced from micron-sized metallic particles impacted as similar velocities via cold spraying [1]. The relative densities of films are an indirect measure of the amount of deformation that occurred upon impact, because densification requires deformation to fill the interstices between the particles. Our own experimental work with 2–40 nm Ag NPs impacted at velocities of 1,000 m/sec also showed significant differences compared to deposition of larger particles at similar velocities. With 2–40 nm particles, porous polycrystalline films were produced with a relative density of only about 70% [15, 16]. Unlike films produced from micron-sized particles, films produced from these very fine NPs are composed of grains having relatively low aspect ratios (near unity) [8]. Taken together, these experimental findings suggest that the magnitude of deformation that occurs upon impact decreases with decreasing particle size.

In this study, we investigate the morphologies of several high speed particle-on-particle impact events of 2–40 nm particles using transmission electron microscopy (TEM) for the first time. These studies reveal that a range of impact morphologies result, even for particles with nominally similar sizes and impacted at similar impact velocities. This suggests that there are additional impact parameters beyond those that have been previously identified (particle size and impact velocity) [17] that play a role in determining whether impact leads to epitaxial or polycrystalline deposition. It should be noted that important information about the particles prior to impact such as particle crystallographic orientations and particle-particle crystallographic misorientations cannot be controlled experimentally nor ascertained from *post mortem* observations. For this reason, molecular dynamics (MD) simulations have also been employed in this study. These simulations allow the impact parameters to be controlled and independently varied so that the influence of specific impact parameters on deformation behavior and the final microstructures obtained during particle-to-particle impact events can be studied. These simulations show that, in addition to particle size and velocity, other impact parameters including particle orientation and particle-particle misorientation also significantly influence the final state following impact. The similarities in the particle morphologies between those obtained from experiments and those obtained from the final states of the simulations provide evidence that the dynamic events observed in the simulations capture the essential mechanisms responsible for the observed behaviors.

3.2: PROCEDURES

Laser ablation

A schematic drawing of the laser ablation apparatus used to produce the nanoparticle aerosol is shown in Fig. 3.1(a). A pulsed, KrF excimer laser (Lumonics PM-848, Light Machinery, Inc., Ottawa, Canada) with a nominal wavelength λ = 248 nm, maximum power output of 80 W, and pulse length of 12 ns was used at its maximum repetition rate of 200 Hz. Two cylindrical lenses of focal lengths f_1 = 110 cm and f_2 = 14 cm were used to focus the beam both horizontally and vertically. The laser beam energy was set at 250 mJ and the beam area at the ablation zone was measured to be 0.08 cm^2 (height: 4 mm, width: 2 mm), resulting in a fluence on the MPs of 3.1 J/cm^2, which was well above the breakdown threshold for ablation for Ag MPs (0.8 J/cm^2) [18].

a) b)

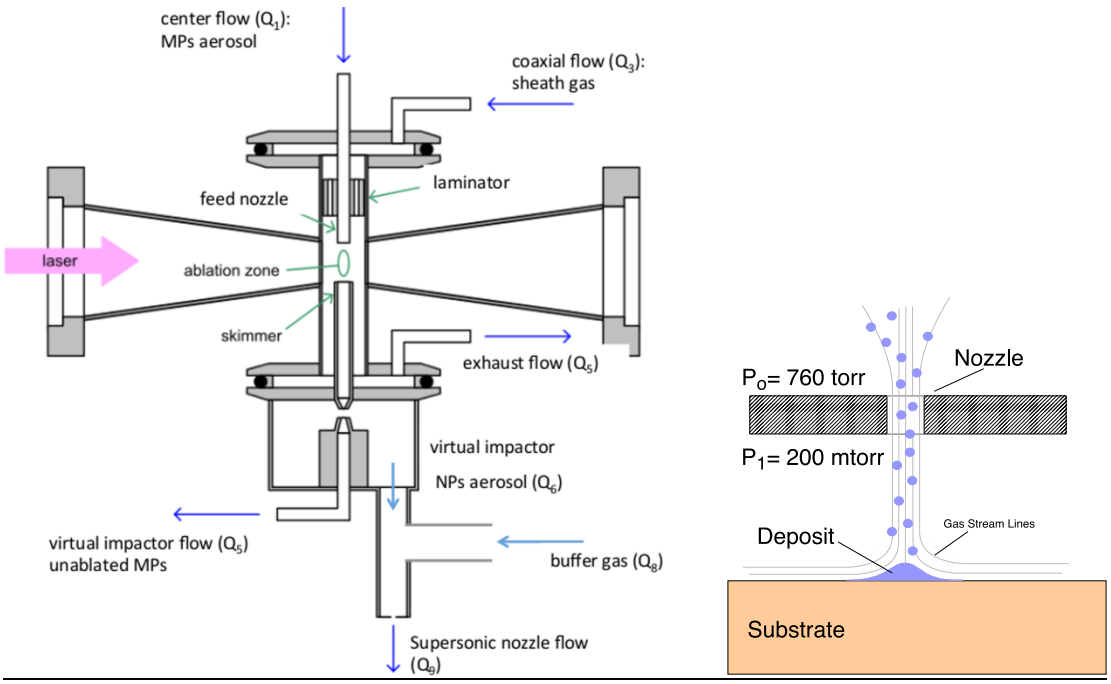

Figure 3.1: a) Laser ablation system for production and deposition of nanoparticles, b) deposition of nanoparticles by acceleration through a supersonic nozzle.

The MP aerosol was fed into the ablation zone through a coaxial nozzle at a gas velocity of approximately 80 cm/sec so that the laser beam struck the MPs only once as they traveled through the ablation zone. Both the central gas and the coaxial sheath gas were He at a pressure of 1 atmosphere. The center flow (Q_1) was adjusted to achieve the desired 80 cm/sec velocity, depending on the cross-sectional area of the feed nozzle. The sheath flow (Q_3) was first laminarized and then fed around the center flow to constrain the center flow and maintain laminar flow past the ablation zone and into the skimmer. The center flow as well as part of the sheath gas was captured by the skimmer, and the remaining gas flow exited to a fume hood. To remove any unablated MPs or

agglomerated NPs from the ablated aerosol, a virtual impactor was used with a cutoff size set at 500 nm (e.g., only particles smaller than 500 nm were passed to the deposition chamber).

Acceleration of NPs

The NP aerosol was accelerated through a flat-plate nozzle by the pressure differential between the ablation chamber held at atmospheric pressure (760 torr) and the deposition chamber which was pumped using a mechanical vacuum pump to a pressure of approximately 200 mtorr, as shown in Fig. 3.1(b). The nozzle and the nozzle aspect ratio was fixed at 1:1 so that the nozzle diameter and plate thickness were both equal to 0.25 mm. This resulted in choked flow which was maintained through the nozzle.

Huang *et al.* developed a model to predict the velocity reached by Ag NPs, taking into account the gas dynamics through the nozzle and the drag force of the gas on NPs [8]. The partial differential equation that describes the NP speed developed by Huang *et al.* was solved numerically and the maximum speed and deposition energies reached by the NPs were calculated and are presented in Fig. 3.2. Note that the deceleration that occurs prior to impact is negligible for the range of experimental conditions that are typically used in LAMA [8]. Using He as a carrier gas, the maximum predicted velocity reached by a typical 5 nm particle for a 0.25 mm nozzle is predicted to be approximately 1,000 m/sec upon impact (corresponding to a kinetic energy of 0.6 eV/atom). The deposition velocity for more massive 20 nm particles is less than 800 m/sec (corresponding to a kinetic energy of approximately 0.35 eV/atom).

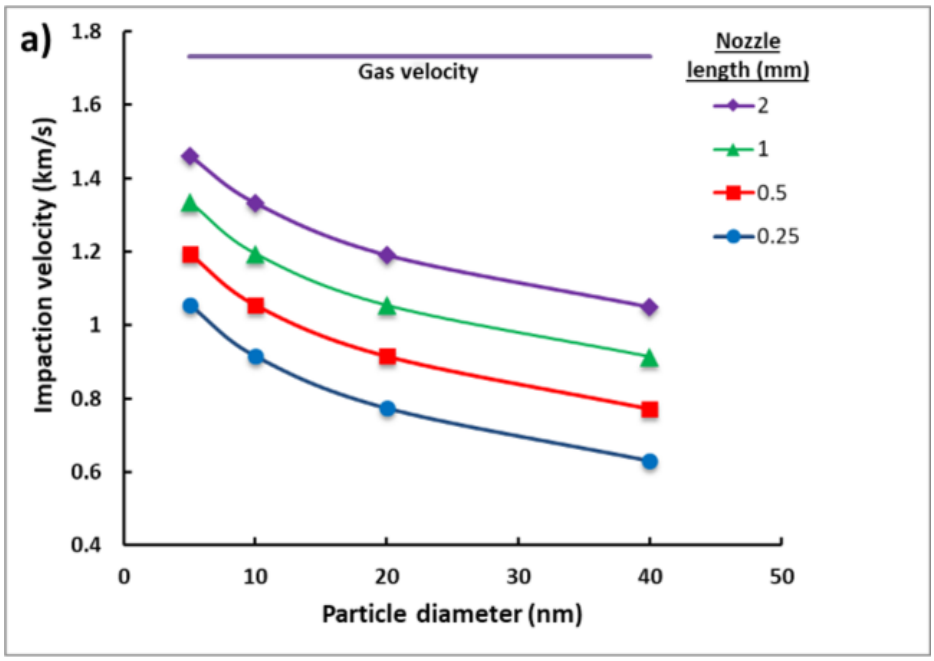

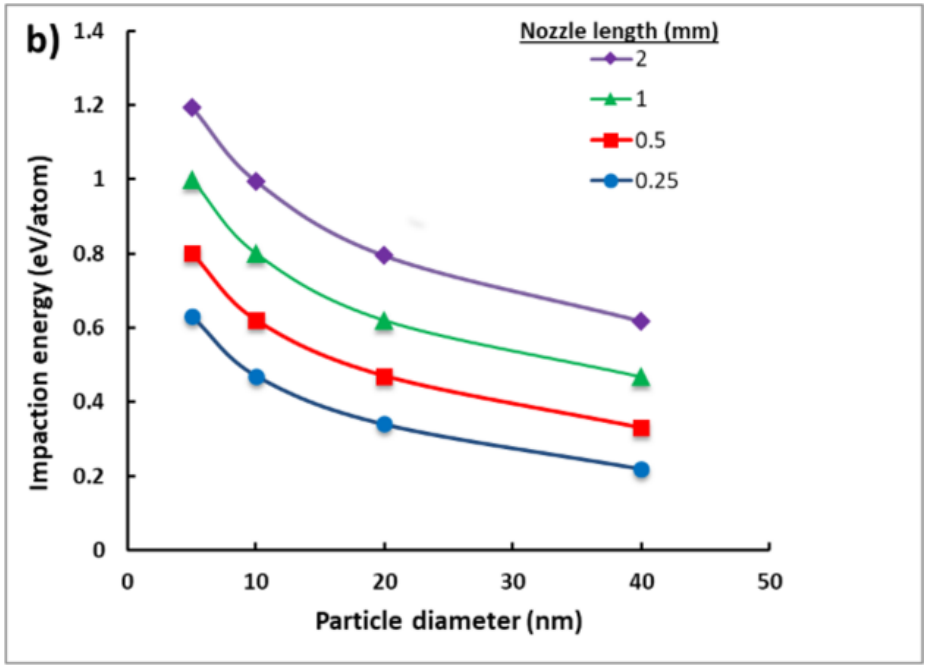

Figure 3.2: a) Influence of accelerating nozzle diameter (nozzle diameter = nozzle plate thickness) and particle size on the final impact velocity for Ag NPs, b) Influence of accelerating nozzle diameter and particle size on the final impact energy/atom for Ag NPs.

Transmission Electron Microscopy

Previous TEM observations reveal that the as-produced Ag particles from LAMA are spherical, range in diameter from 2–40 nm, and are free of a measurable surface oxide. Some of the particles contain defects such as stacking faults and twins, depending on processing conditions [8, 19]. To further investigate the final morphology of particle following impact by the LAMA process, TEM grids with a Formvar® support film (Model 200M-TH, Ted Pella Inc., Redding, CA) were clamped onto a flat substrate and NPs were deposited onto the TEM grids. A large nozzle-to-substrate distance equal to about 10 times the nozzle diameter was used for these experiments in order to minimize damage to the delicate support TEM films. The stage was translated beneath the deposition nozzle fast enough (approximately 5 mm/sec) so that some of the particles deposited onto the grid or into the Formvar film were individual NPs or small clusters of nanoparticles.

A TEM (2010F, JEOL, Tokyo, Japan) was used to image the NPs at sufficiently high magnification such that lattice planes were visible. In some cases, regions of the images were cropped and Fourier transforms were performed to obtain diffraction patterns from selected regions. The diffraction patterns were used to identify whether specific regions were monocrystalline or polycrystalline and to analyze the nature of defects such as stacking faults.

Molecular Dynamic Simulations

Molecular dynamics (MD) simulations of the impact of a NP onto a stationary NP were conducted using LAMMPS [20] implemented on the Lonestar Linux cluster at the Texas Advanced Computing Center (TACC) [21] at the University of Texas at Austin. The embedded-atom-method (EAM) potential for Ag from the NIST Interatomic Potentials Repository Project was used [22]. The simulation volume was 100 × 100 × 150 lattice constants (lattice constant= 0.409 nm for Ag), with the larger dimension in the *z* direction, which corresponded to the NP impact direction.

Representative spherical particles with diameters 13.6 nm for the impacting particle and 32 nm for the stationary impacted particle (~80,000 atoms and ~ 1,000,000 atoms, respectively) were studied using the simulations. Details on why this particular configuration was studied using MD simulations is presented in the Results section. We considered only particles that were free of stacking imperfections to limit the parameter space to a reasonable number of variables and, consistent with experimental observations, we assumed that the particles were free of surface oxides. Since the influence of NP size on the final microstructures has been previously studied in detail [17], nanoparticle size was not varied in the current study.

The two NPs in the simulations were placed so that they were not touching the simulation boundary at the start of the simulation, which is equivalent to a vacuum interface at the edges of the NPs. The edges of the simulation volume were treated by LAMMPS as periodic in all three dimensions. During the simulation, the particles never contacted the edges of the simulation volume and therefore they did not interact across

the periodic boundaries. The Ag atoms in the larger stationary NP and the smaller impacting NP were allowed to thermalize at 300 K for 100 ps before the smaller NP was set in motion in the *z* direction. A temperature of 300 K was chosen because the stagnation conditions for impact experiments are approximately 300 K and one atmosphere, and the residence times are extremely short in the region where the gas temperatures are significantly depressed at the exit of the nozzle [8], which results in particle temperatures that are near 300 K at impact. The angular momentum of the impacting NP was set to zero at every timestep during thermalization to control particle orientation during thermalization, and the linear momentum in the bottom 50% of the stationary NP was set to zero every timestep during the impact to prevent the particle from moving out of the simulation volume.

Following the thermalization, a constant velocity was imparted to all atoms in the impacting NP. The time integration for the equilibration of the system to 300 K and for the subsequent impact were performed with a time step of 0.002 ps (2 fs) using Nose-Hoover style, non-Hamiltonian equations of motion on the isothermal-isobaric (npt) ensemble [25], which generated positions and velocities of the atoms at every time step. The positions of all atoms were recorded at intervals of 2 ps for the first 80 ps after impact and at intervals of 80 ps for the remaining 240 ps. Although there were minor fluctuations in atom and grain-boundary positions in some cases, a simulation time of 320 ps was selected to represent the final state because the deformation and microstructure were no longer noticeably evolving at this time.

Applying a Langevin condition to a few layers of atoms below the region of impact is one of the methods that has been used previously to effectively damp the compressional waves that are launched upon impact and to prevent their undesirable reflection back to the impact interface [23, 24]. For our simulations, we observed that the range of impact velocities are not high enough to produce shock waves, and the back-reflected acoustic waves are negligible. To confirm this, simulations were performed both with and without the Langevin condition, and it was observed that the Langevin condition did not affect the microstructural evolution following impact. Thus, subsequent simulations did not include the Langevin condition.

Visualizations of the atomic positions were conducted off-line using the OVITO visualization software [26]. Polyhedral template matching (PTM) was used to identify the local atomic environments for all atoms in the simulations, which allowed the local stacking sequence for the atoms to be determined [27]. The visualizations were color-coded with this information with green representing local regions of FCC stacking and red representing regions with a local HCP stacking. When the atomic stacking sequence could not be identified (e.g. at grain boundaries or where the atoms were disordered), atoms were colored white. A cutoff value of the root-mean-square deviation (RMSD) threshold of 0.15 was used in our simulations, which produced results that agreed with visual inspections of ordered and disordered regions of the simulations.

3.3: RESULTS AND DISCUSSION

Experimental Studies of Two Particle Impacts

Impact of many clusters of NPs were studied in the TEM to ascertain their final microstructures after NP impact. Most impacts resulted in either single particle or multiparticle depositions. To allow for unambiguous analysis, only the rarer cases of two particle impacts were analyzed and are presented here. Observations using the high resolution TEM revealed examples of two general types of final particle morphologies for two particle impact events: 1) non-epitaxial deposition and 2) epitaxial deposition. The term non-epitaxial is used when the final microstructure for the impacted NP and the particle onto which it impacted contain one or more grain boundaries, and the term epitaxial deposition is used when the final microstructure consists of a single crystallographic orientation. Multiple examples of each type of final microstructure were observed experimentally and representative examples are shown below. Although detailed statistical analysis of the fraction of particles that deposited epitaxially could not be performed given the small fraction of two particle impacts, evidence of both epitaxial and non-epitaxial depositions were readily observed in many of the multiparticle impacts.

Non-Epitaxial Deposition

Two examples of non-epitaxial deposition are shown in Fig. 3.3. In Fig. 3.3(a), a spherical NP is still clearly visible after impacting onto a previously deposited NP. The lattices fringes in the TEM image show that there is no continuity of the crystallographic

planes across the original boundary between the two NPs, indicating that this was a non-epitaxial deposition. A closer look at the crystallographic arrangements within the spherical NP shows periodic changes in contrast that are consistent with planar defects. A 12 nm Ag particle impacted onto a larger Ag particle is shown in Fig. 3.3(b). Again, the lattice fringes in the TEM image show that there is a sharp discontinuity in the crystallographic planes across the original boundary between the two NPs defined by connecting the two regions of concave curvature. In this case, the smaller NP is itself clearly polycrystalline, consisting of a number of grains smaller than 5 nm.

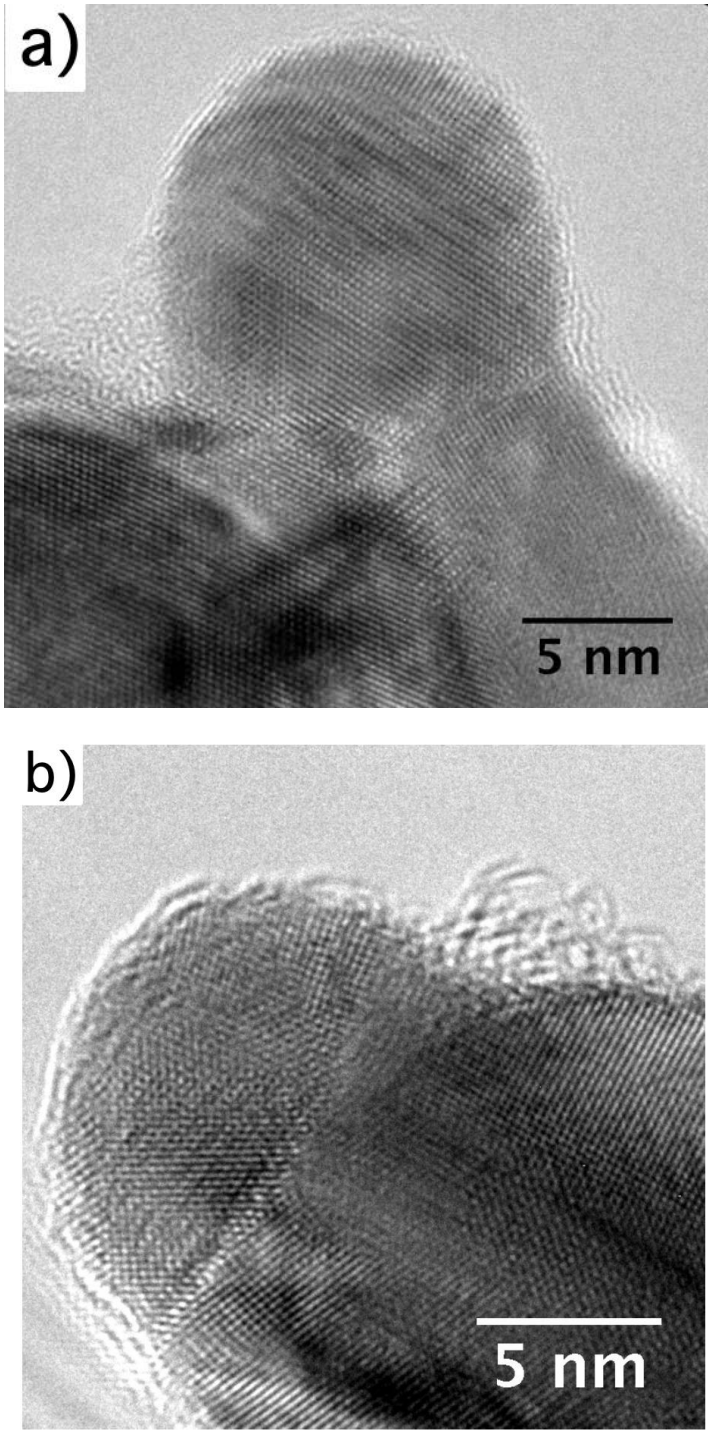

Figure 3.3: a) and b) High resolution TEM images of NP-NP impact events showing two representative examples of non-epitaxial deposition.

Epitaxial Deposition

The TEM image of a particular two-particle impact event where a 13.6 nm NP impacted epitaxially onto a 32 nm NP is shown in Fig. 3.4(a). Lattice fringes are apparent in the upper portion of smaller 13.6 nm particle with a spacing of 0.24 nm, which is consistent with the known {111} interplanar spacing for Ag. Dark bands, perpendicular to the direction of impact and parallel to the interface between the impacting and impacted particle, are visible in the micrograph. The dark bands are likely stacking faults or twins [28] that appear as bands because the TEM micrograph was slightly misoriented with respect to a zone axis.

The orientations of the lattice planes can be followed starting in the impacting particle and progressing down into the impacted particle. It is apparent that these planes are continuous across the interface between the impacting and impacted particle, suggesting that this impact resulted in epitaxial deposition. Fourier transforms of the impacting and impacted particles were generated by masking off regions of the image so that only the particles of interest were visible before performing the transform. The upper inset shows that the Fourier transform for the impacting particle contains two spots, consistent with the single set of planes that is visible in the image. The streaking of these spots is due to slight changes in orientations of the lattice planes that occur as the planes intersect the stacking faults. The Fourier transform for the impacted particle contains the same two spots, in the same orientations as the Fourier transform for the impacting particle. This confirms that the particles have approximately the same orientation. Note that the left side of the impacted particles contains two additional pairs of lattice fringes

that are much weaker than the primary lattice planes. The corresponding Fourier transform contains two additional but weaker pairs of spots associates with these fringes. Since the right side of the impacted particle does not exhibit these additional lattice fringes, we believe the fringes on the left side of the particle result from a slight tilt of this portion of the crystal resulting from stacking faults/partial dislocations that terminate within the impacted particle. This tilt makes additional planes visible that are not visible in the impacting particle or the right side of the impacted particle. Analysis of the angles between these spots and the relative distances between co-linear spots suggests that these additional lattice fringes are from {111} and {200} planes. A similar example of an epitaxial deposition is shown in Fig. 3.4(b).

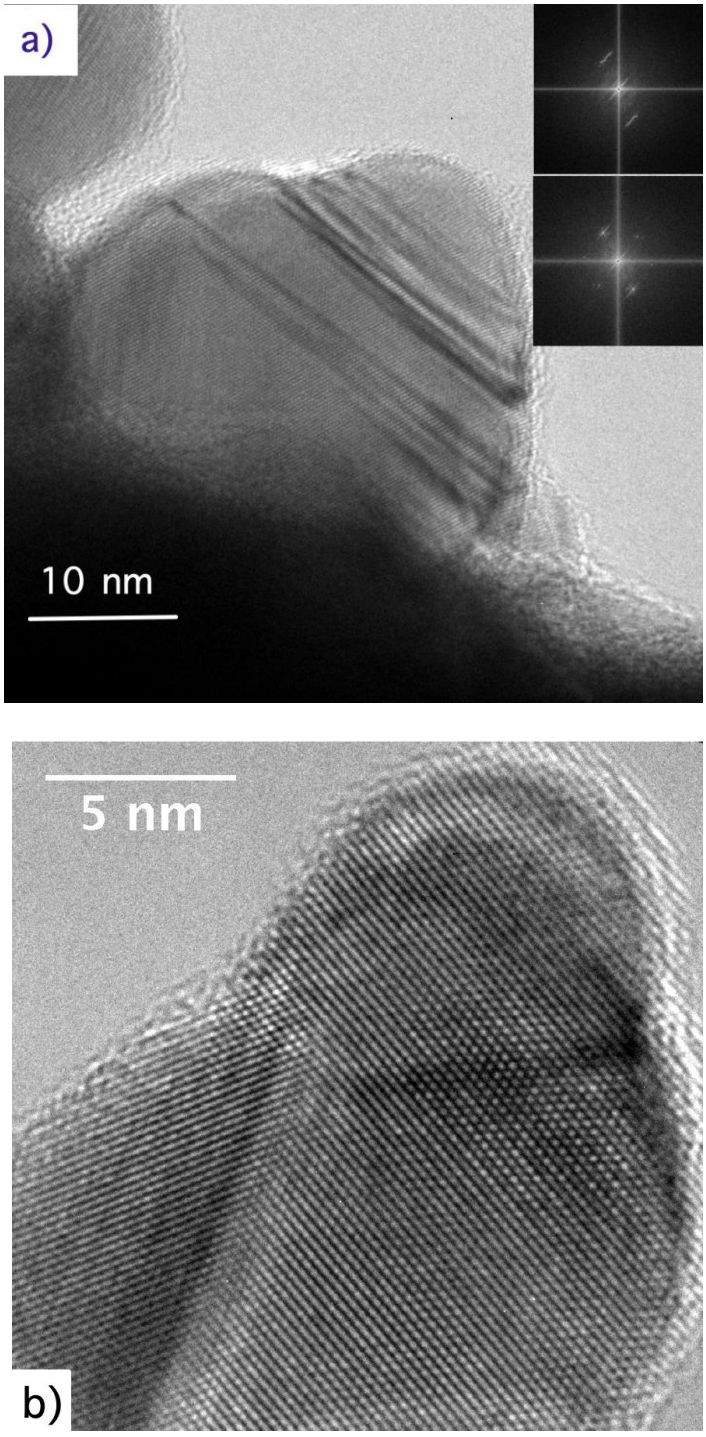

Figure 3.4: a) and b) TEM images of a two particle impact events where epitaxial deposition was observed: overview of two particle impacts with insets showing fast Fourier transforms of impacting (top) and impacted (bottom) particle.

The TEM images reveal that a range of particle morphologies and defect states result from particle impact under nominally identical conditions. The mechanism for non-epitaxial deposition shown in Fig. 3.3 in which a grain boundary is formed at the interface between the impacting and impacted particle is intuitively obvious. Instead we focus on the conditions and mechanism that produce epitaxial deposition in a two-particle impact. To do this, we study in detail a particular impact event shown in Fig. 3.4(a) that lead to epitaxial deposition. The NP diameters can be inferred from the TEM images and the NP impact velocities can be estimated from [8]. However, information about the particles prior to impact such as particle crystallographic orientation and particle-particle crystallographic misorientation is not known. Thus, molecular dynamics (MD) simulations were used to study the influence of uncontrollable or unknown experimental impact parameters on the final microstructures obtained during this particle-to-particle impact event.

MD Simulations of a Two Particle Impact Event

The particle size for the impacting particle was determined to 13.6 nm for the impacting NP and 32 nm for the impacted NP, based on the areas of the particles and assuming the particles were spherical prior to impact. The impact velocity of the 13.6 nm particle was calculated using Fig. 3.2, and was determined to be 860 m/sec. This velocity was used in the simulation of the two-particle impact which was subsequently followed from the instant the two particles made contact until the final microstructure was formed by both particles reaching a steady-state. Snapshots of a cross section containing 5 atomic

layers from the region near the central cross-sections of the particle are shown for each MD simulation. A {110} type cross-section in the impacting NP is chosen consistently for viewing in all the simulations.

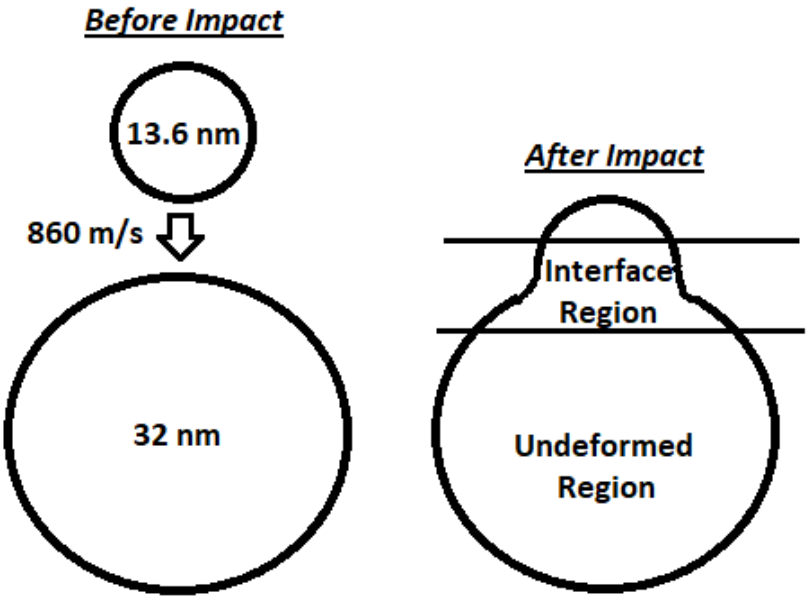

Figure 3.5: Schematic of the two particle impact event studied by TEM and MD simulations.

Statistical Fluctuations

Statistical fluctuations in atomic positions from thermal vibrations result in variations in experiments that can also be simulated. To determine if these fluctuations were the cause of the observed variability in the observed final states for experiments, several simulations were conducted under nominally identical conditions: an initially defect-free 13.6 nm NP was impacted at 300 K onto a stationary 32 nm NP at 860 m/sec,

with the particles initially having a 45˚ crystallographic misorientation about the axis of impact. The results of these simulations after the particles had reached a steady state are shown in Figs. 3.6(a-c). Although there are very minor atomistic differences between the final states from these three simulations conducted under the same impact conditions, all aspects of the deformation microstructures are similar. In each case, the final morphology consists of a non-epitaxial deposition, with multiple grain boundaries present in the original impacting NP. In addition, stacking faults are present, primarily in the impacting NP. Since stacking faults in FCC metals can result from either deformation or rapid crystallization, it cannot be ascertained which mechanism gave rise to the faults from observations of these final states. Nevertheless, it is clear from these simulations that thermal fluctuations result in only minor atomistic differences in the final states and thus, these fluctuations cannot be responsible for the large range in final morphologies from polycrystalline to epitaxial that were observed experimentally under nominally identical deposition conditions.

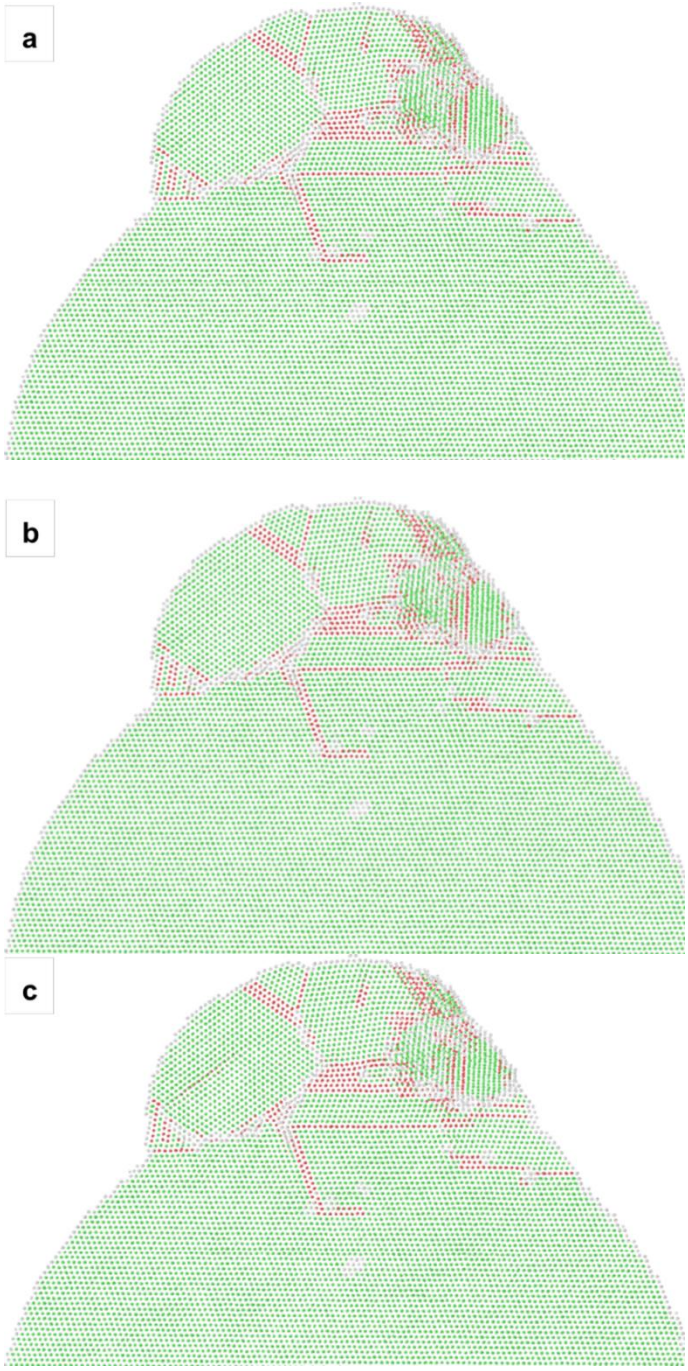

Figure 3.6: Reproducibility of simulations: Three simulations conducted with nominally identical impact conditions: v = 860 m/sec, Stationary impacted NP orientation (Miller indices): x [$1\bar{1}0$], y [$11\bar{2}$], z [111], Impacting NP is misoriented by 45˚ with respect to the impacted NP about its impact z [111] axis. Cross sections are taken at the same position.

Influence of Variations in Impact Velocity

The impact velocity of 860 m/sec that was assumed in the previous set of simulations was based on average properties of the particle and gas. However, it is likely that actual particle impact velocities are distributed about a range of impact velocities. Meinander *et al.* [29] have suggested that epitaxial deposition may be favored at higher velocities when a particle impacts a flat substrate. To determine if this trend also holds when a particle strikes another particle, a series of simulations were conducted in which the particle velocity was varied from 860 m/sec to 1,300 m/sec.

Fig. 3.7 shows the final states for simulations that were conducted with all variables fixed except for the particle impact velocity. Comparing Fig. 3.7(a) (v = 860 m/sec) to Fig. 3.7(b) (v = 1,000 m/sec), it is apparent that the impacting particle is more heavily deformed at the higher velocity. However, many of the other key microstructural features such as the presence of multiple grain boundaries in the original NP and the presence of stacking imperfections is similar between the two simulations. Increasing the impact velocity further to 1,300 m/sec (Fig. 3.7(c)) results in qualitatively different impact morphology compared to the lower impact velocities. In this case, both the impacting particle and the top part of the impacted NP are severely deformed to a degree that is significantly greater than what was observed experimentally. This suggests that the impact velocity in the experiment did not reach such extreme velocities. Comparing all the three figures, we observe that the degree of polycrystallinity decreases with impact velocity which is evident in the size of the small grains near the surface. At 860 m/sec, two large surface grains are observed. When the velocity is increased to 1,000 m/sec, the

grain that is visible on the left side of the impacting particle shrinks considerably and it disappears completely for impacts at 1,300 m/sec. The size of the grain on the right decreases when the velocity is increased. This trend suggests that at extremely high velocities, the grain on the right might be eliminated, leading to an epitaxial crystalline state. However, for the range of possible experimental impact velocities, epitaxial deposition was not observed in these simulations. These simulations show that impact velocity plays a significant role in the amount of deformation that occurs upon impact and also influences the final crystalline state in the impacted particles. However, none of the simulations predicted epitaxial deposition.

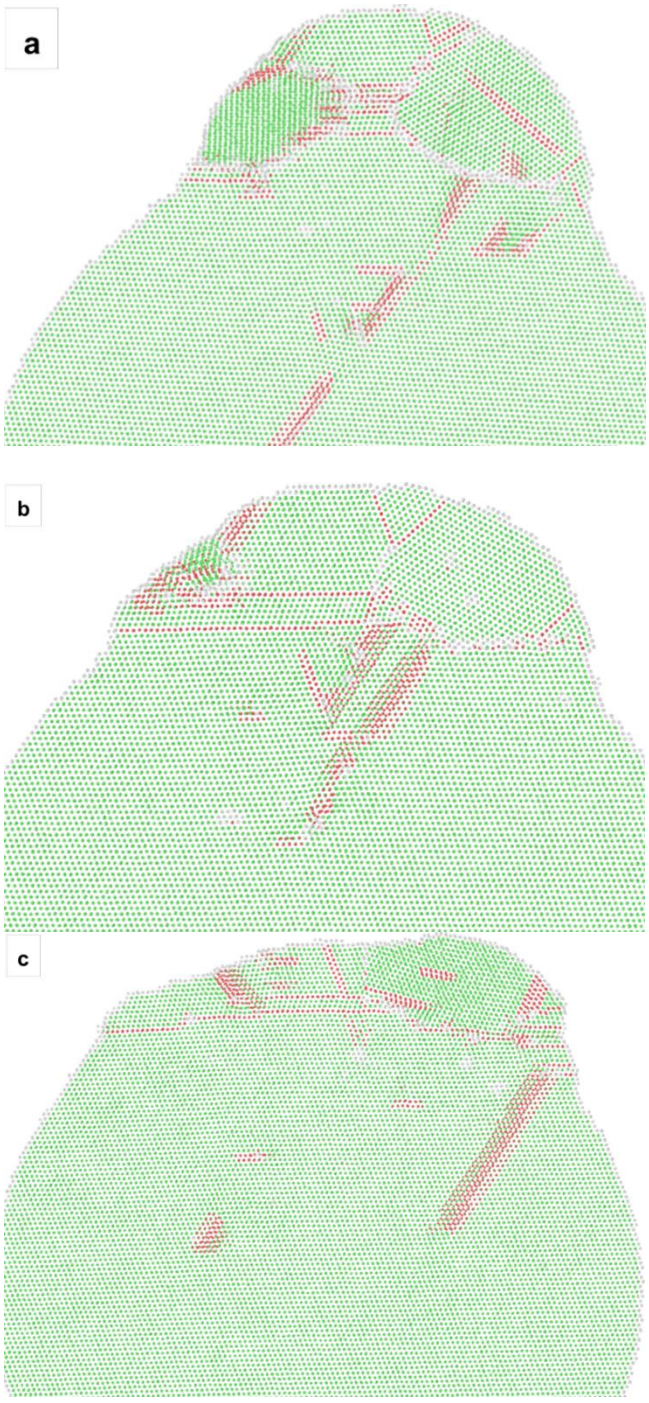

Figure 3.7: Influence of particle velocity (no misorientation): a) v = 860 m/sec, b) v = 1,000 m/sec, and c) 1,300 m/sec. Impacted NP orientation (Miller indices): x [$1\bar{1}0$], y [$11\bar{2}$], z [111], Impacting NP is misoriented by 0˚ with respect to the impacted NP about its impact z [111] axis (i.e. both NPs have the same orientation).

Influence of Crystallographic Orientation and Misorientation of the NPs

Since partial dislocations and twins propagate in <112> directions on corresponding {111} planes in FCC crystals [30–32], the influence of particle impact orientation or particle misorientation with respect to the impacted particle could affect deformation and the final state of the impacted particles. The effects of particle orientation and particle misorientation are particularly challenging to study experimentally because the orientations of the particles cannot be controlled and the orientations of the particles prior to impact cannot be ascertained by observation of the final states of the particles. Thus, simulations are essential for studying orientation and misorientation effects. Simulations were first performed where the influence of impact direction was studied. For these simulations the impact direction was [001], [111] and [110]. For these simulations the impacting and impacted particle had the same orientation (i.e. there was no misorientation between he impacting and impacted particle). The results of these simulations are shown in Fig. 3.8(a-c). It is observed that the overall degree of deformation varies with impact orientation. The greatest deformation is observed when the impact direction is along the particle [001] direction (Fig. 3.8(a)) and the least deformation occurs when the impact direction is along the particle [110] direction (Fig. 3.8(c)). In the case of [001] and [111] impact orientations, the final states were polycrystalline. However, for the [110] impact orientation, where the least deformation was observed, the resulting final state was epitaxial. For all three impact orientations, many stacking imperfections are apparent that have a range of orientations relative to the impact direction.

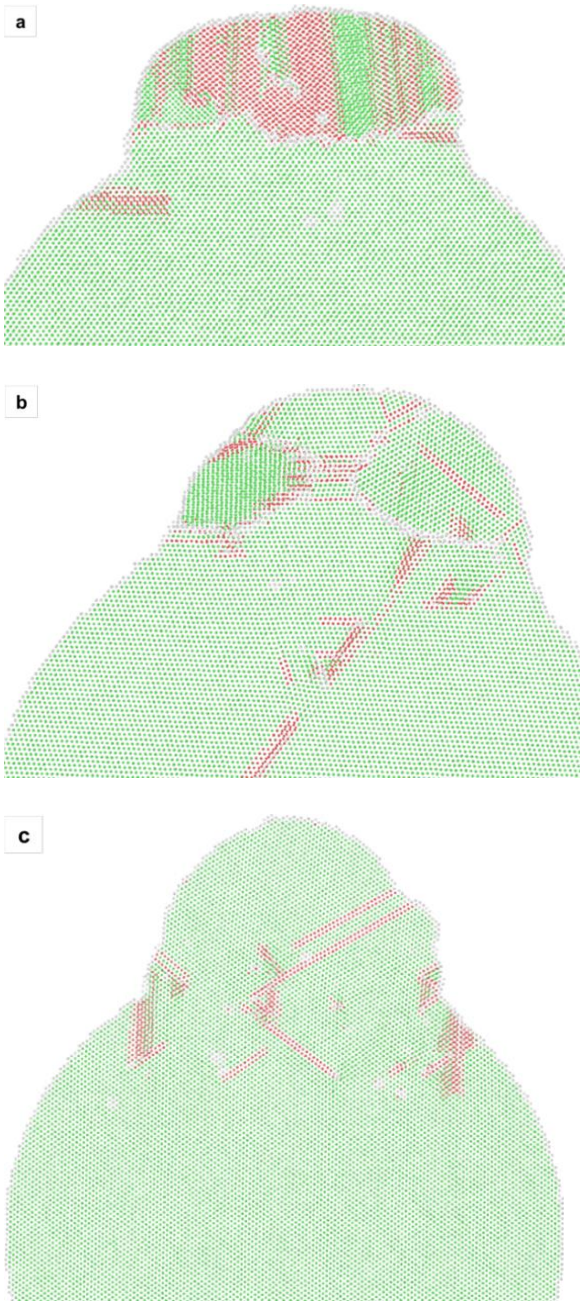

Figure 3.8: The influence of particle orientation relative to the impact direction for defect-free particles with an impact velocity = 860 m/sec with impacting and impacted particles having the same orientation with respect to each other. The impact direction relative to this orientation was varied: a) [001], b) [111], and c) [110]. Miller indices of the NPs are a) x [100], y [010], z [001], b) x [$1\bar{1}0$], y [$11\bar{2}$], z [111] and c) x [$\bar{1}10$], y [001], z [110]. Unlike b) and c), the viewing direction in a) is along a <110> direction along the impacted NP.

Figs. 3.9(a-c) show the influence of NP-NP misorientation. For these simulations, NPs were impacted at 860 m/sec, the impacting particle direction was fixed along the [110] direction, and the misorientation angle was varied by changing the orientation of the impacted NP. Note that Figs. 3.8(c) and 3.9(a) show the results from the same simulation for impact along the [110] direction, with no misorientation between the impacting and impacted particles. For Figs. 3.9(b) and (c), where there is a misorientation between the impacting and impacted particle, the final states show that a grain boundary results near the interface between the particles. Comparing the results shown in Fig. 3.8 where the impact axes were varied to those shown in Fig. 3.9 where the degree of misorientation was varied, the differences in the overall degree of deformation and in the number and orientation of the stacking imperfections is much less dramatic in the latter case. In summary, these simulations show that the degree of deformation and the final morphology are primarily governed by impact velocity and particle orientation.

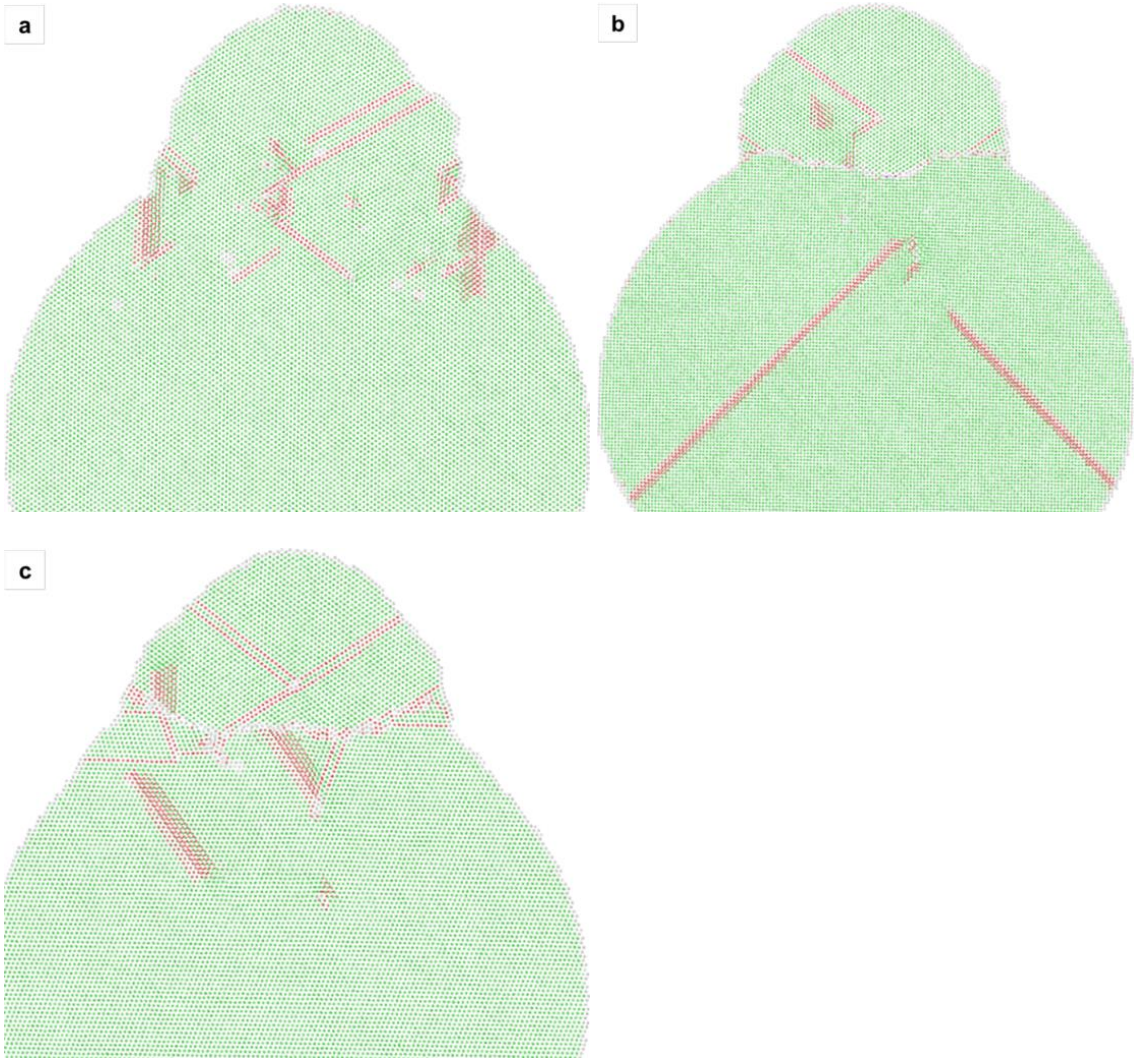

Figure 3.9: Influence of particle-particle misorientation for defect-free particles with a fixed impact velocity = 860 m/sec and with the impact orientation along the [110] for the impacting particle with a) no misorientation; both particles are aligned so that the impacting direction is along the [110] orientation, b) the [001] in the impacted particle is parallel to the impact direction and c) the [111] in the impacted particle is parallel to the impact direction. Miller indices of the impacted NPs are a) x [$\bar{1}$10], y [001], z [110], b) x [100], y [010], z [001] and c) x [1$\bar{1}$0], y [11$\bar{2}$], z [111].

Study of Conditions Leading to Epitaxial Deposition

Fig. 3.8(c)/9(a) show the only instance predicted of epitaxial deposition among all of the conducted MD simulations. To determine the sensitivity for epitaxial deposition to small misorientations of the impacting NP with respect to the stationary impacted NP, another set of simulations was conducted in which small tilt misorientations of 5˚, 10˚, 15˚ and 20˚ were introduced to the impacting NP and the particles were again impacted a velocity = 860 m/sec. The small tilt misorientations were applied about the non-impacting orthogonal *x* [$\bar{1}$10] and the *y* [001] axes with respect to the fixed crystallographic orientation of the impacted NP which has the following miller indices: *x* [$\bar{1}$10], *y* [001], *z* [110]. Figs. 3.10(a) and (b) show the pre-impact tilt misorientation between the NPs for a misorientation angle of 10˚ about the x and y axes respectively.

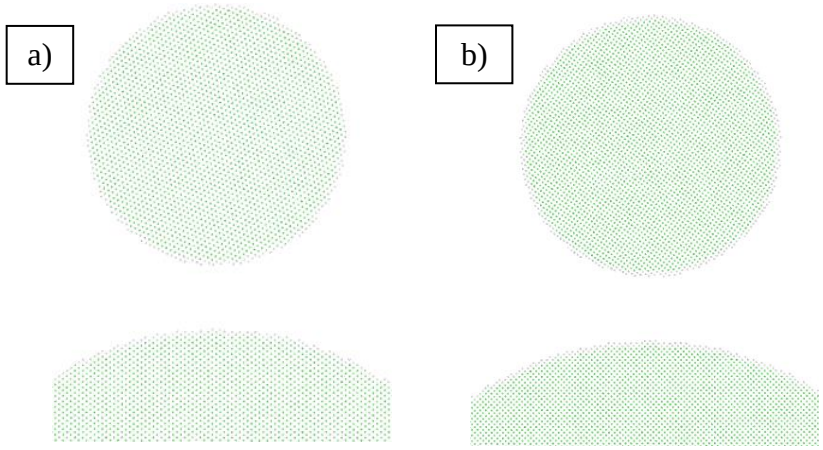

Figure 3.10: Pre-impact tilt misorientation of 10˚ between the NPs about the orthogonal non-impacting a) x [$\bar{1}$10] axis and b) y [001] axis. A cross-section is taken along the [001] direction in b) to view the rotation plane.

Figs. 3.11(a-d) shows the final states for particles impacting with a tilt misorientation of 5˚ (a), 10˚ (b), 15˚ (c), and 20˚ (d) about the non-impacting x [$\bar{1}$10] axis. This figure shows that the NPs deposit epitaxially for tilt misorientations of 5˚, 10˚, and 15˚ about the non-impacting x [$\bar{1}$10] axis. However, for a larger tilt misorientation angle of 20˚, a low angle grain boundary is visible, confirming that the impacting NP did not deposit epitaxially onto the stationary impacted NP. Figs. 3.12(a-d) shows the final states for particles impacting with a tilt misorientation of 5˚ (a), 10˚ (b), 15˚ (c), and 20˚ (d) about the non-impacting *y* [001] axis. These tilt misorientations also produced epitaxial deposition for misorientations of 5˚, 10˚, and 15˚, but grain boundaries were again visible (See Fig. 3.12(e)) when the tilt misorientation was increased to 20˚.

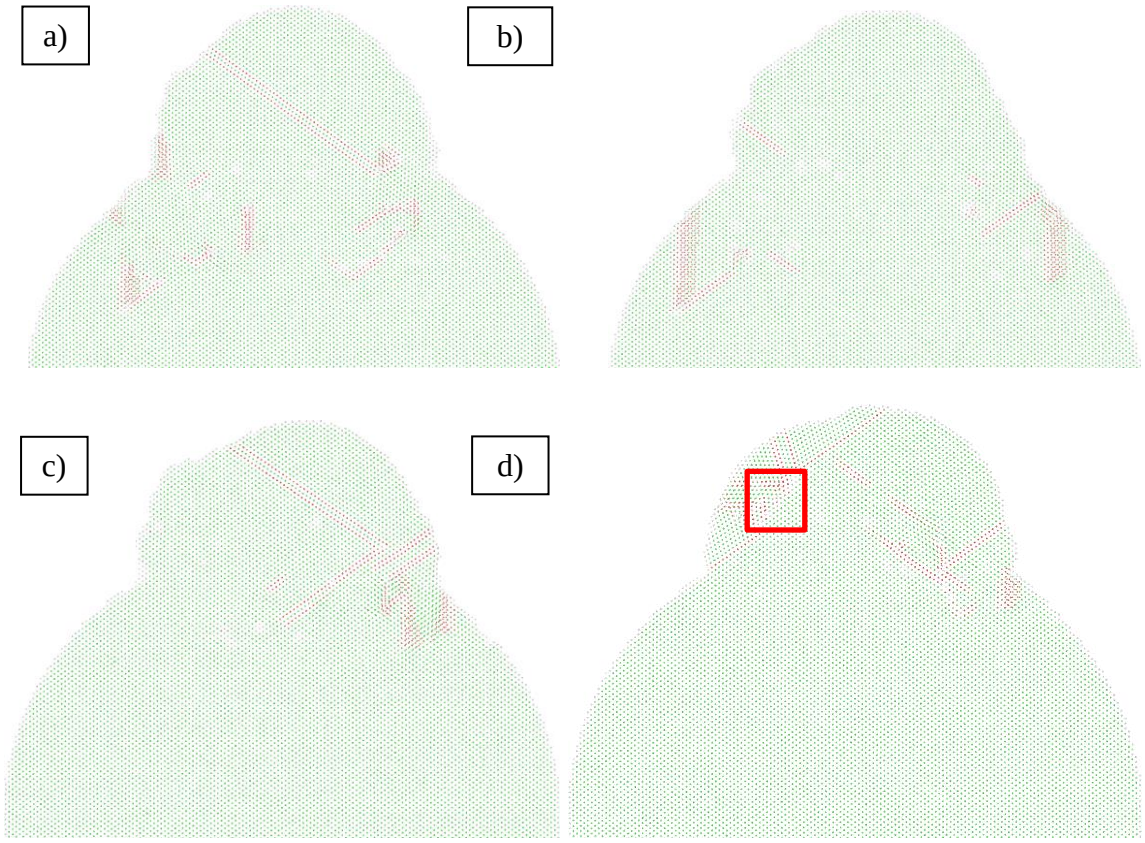

Figure 3.11: Final states following a two NP impact with the impacting NP misoriented with respect to the stationary impacted NP by a) 5˚, b) 10˚, c) 15˚ and d) 20˚ about the non-impacting *x* [$\bar{1}$ 1 0] axis. A low-angle grain boundary separating the surface grain from the rest of the NP is apparent in Fig. 3.11(d) (red box).

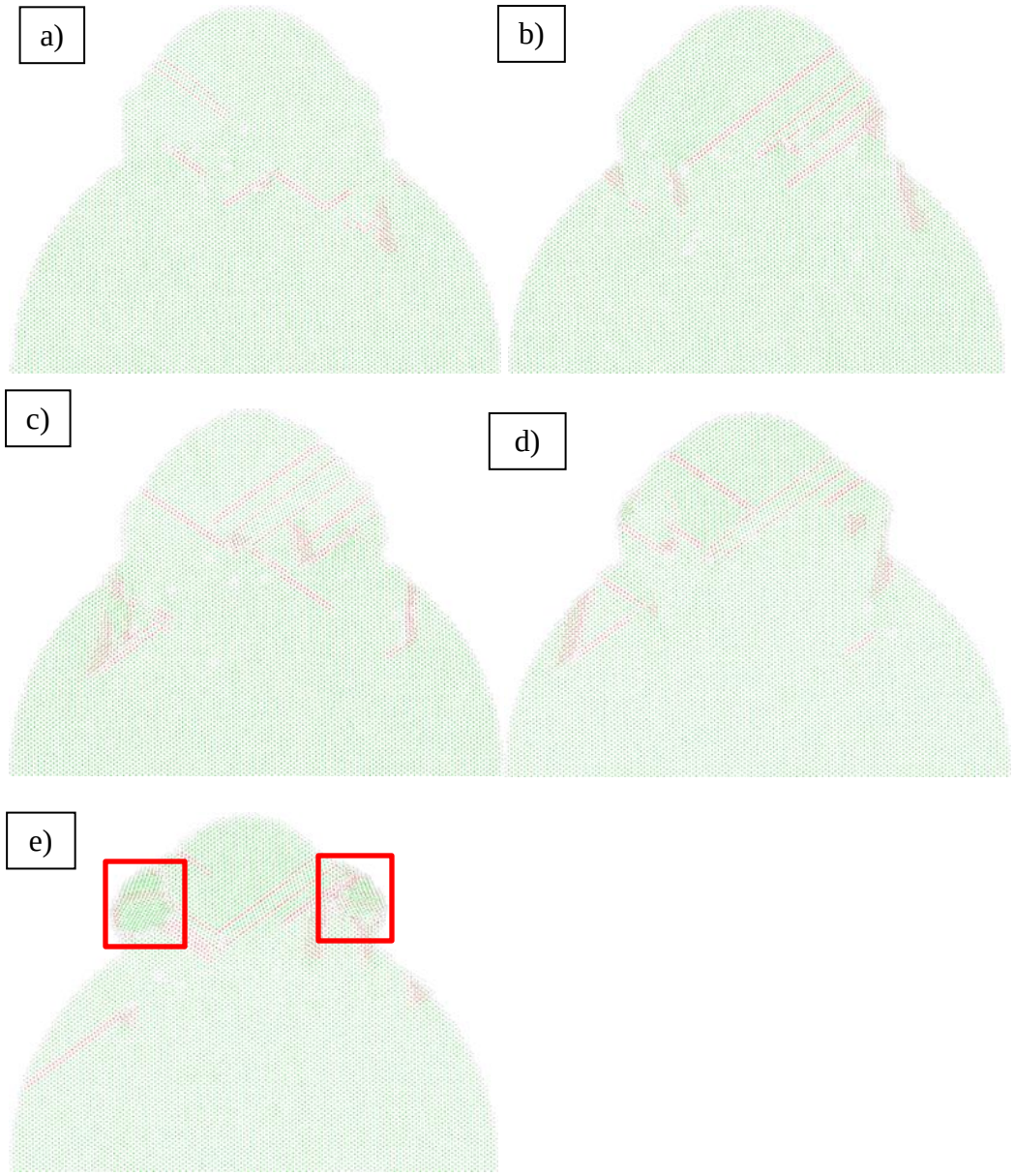

Figure 3.12: Final states following a two NP impact with the impacting NP misoriented with respect to the stationary impacted NP by a) 5˚, b) 10˚, c) 15˚ and d) 20˚ about the non-impacting *y* [001] axis. Fig. 3.12(e) is a different cross-section for the 20˚ case that shows the surface grains more clearly (red boxes).

From these simulations, we can conclude that epitaxial deposition is possible at impact velocity of 860 m/sec when two NPs are tilted up to within approximately 15˚ of the <110>. There is a transition predicted from epitaxial to non-epitaxial behavior when the tilt misorientation angle is increased to larger misorientations. However, we note that only 5 atomic layer thick cross-sections have been shown in Figs. 3.11 and 3.12 where all final states appear to be epitaxial for tilt misorientation of 5˚–15˚. While studying the final microstructures for all the cases of tilt misorientations, we observed that the NPs are disoriented by 0.5˚–3˚. This misorientation between the NPs is accommodated at their interface by a number of stacking faults whose density increases with increasing pre-impact NP-NP tilt misorientation. Since this leads to the creation of a very low-angle grain-boundary between the NPs, the impact event can still be described as epitaxial.

A final set of simulations were conducted in which small twist misorientations of 5˚, 10˚ and 15˚ about the impacting z [110] axis were introduced to the impacting NP impacting at 860 m/sec to study if small twist misorientations also lead to epitaxial deposition. It was observed that the NPs in the final microstructure untwisted only by 1˚–2˚ with respect to the initial twist misorientation between the NPs. Hence, compared to the impact events involving tilt misorientations, twist misorientations are more difficult to eliminate, leading to a high-angle grain boundary between the NPs in the final microstructure. Tilt misorientations of 5˚ and 10˚ lead to the creation of a relatively lower angle boundary which could be accommodated by stacking faults. However, for a higher tilt misorientation of 15˚, the density of stacking faults accommodating the misorientation between the NPs increases rapidly leading to a disordering of the atoms at the grain

boundary. These simulations show that epitaxial deposition is favorable for small tilt, but not twist misorientations of NPs impacting along a <110> direction.

Mechanisms for Epitaxial Deposition for Impact Orientations near [110]

To better understand the mechanisms that leads to epitaxial deposition, a short-time simulation was conducted where a tilt misorientation was applied about the non-impacting *x* [$\bar{1}$10] axis and where the stationary impacted NP was fixed with *x*: [$\bar{1}$10], y: [001], z: [110]. The evolution of the microstructure and morphology was then studied. A representative case for a 10˚ NP-NP tilt misorientation is presented in Fig. 3.13, but we have confirmed that the observed mechanisms are similar for all the studied tilt and twist angles of misorientation.

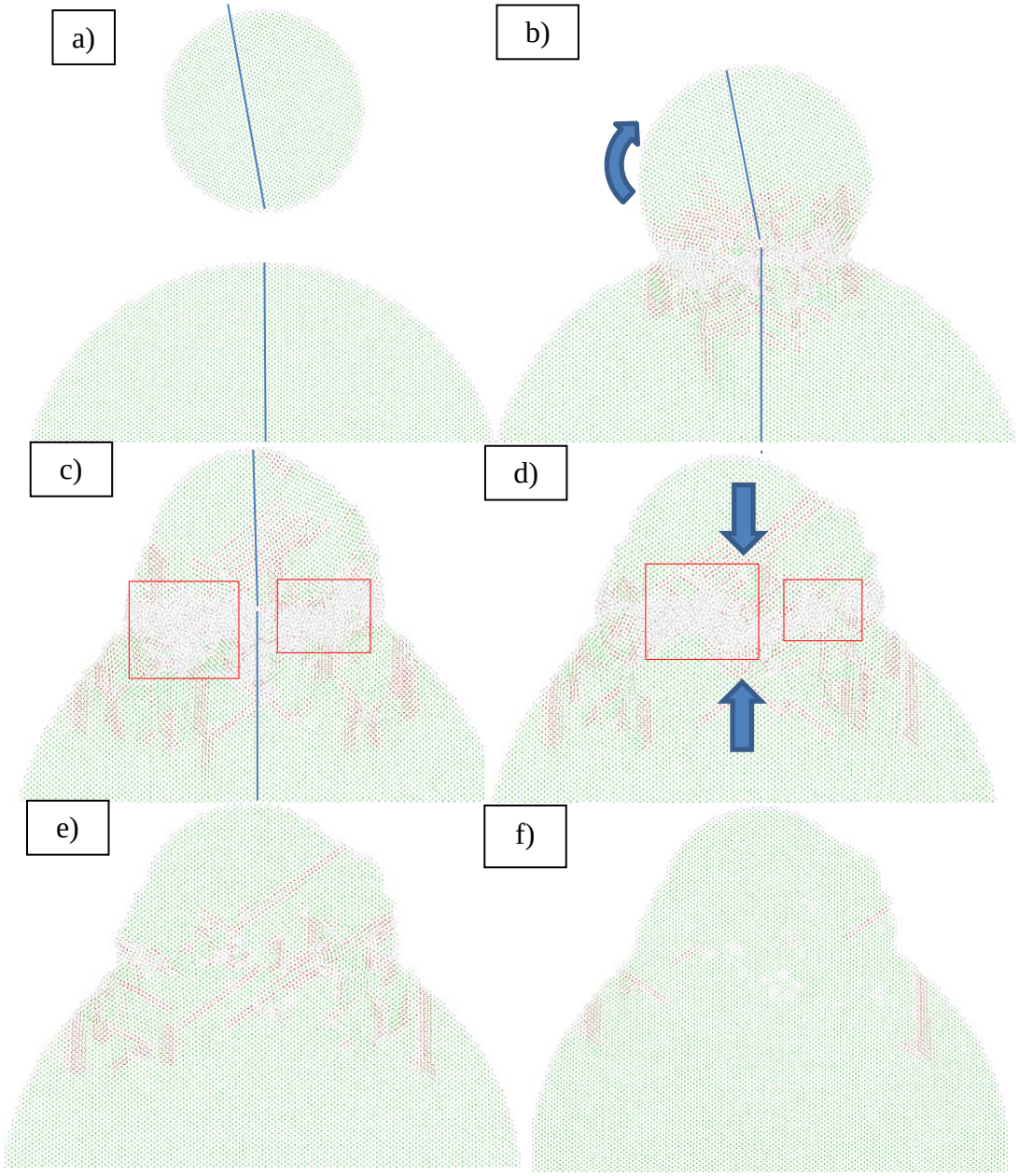

Figure 3.13: Microstructural evolution when the NPs have their impact axis tilted 10˚ from the [110] at a) 0 ps (before impact), b) 8 ps (after impact), c) 16 ps, d) 24 ps, e) 40 ps and f) 440 ps (final state).

Fig. 3.13(a) shows a central cross-section (5 atomic layers thick) viewed along the direction of misorientation x $[\bar{1}10]$. Solid lines are used in the figure to show the orientations of the [110] for the NPs before and following impact. Fig. 3.13(b) shows the NPs 8 ps after impact; it is apparent that there has been significant deformation and that the impacting NP has started tilting towards the impacted NP orientation. The atoms that were part of the impacting particle and that were near the contact region have disordered (atoms colored white) upon impact. Previously, we have shown that such regions of disorder initiate in regions of high von Mises stress [17]. A large number of partial dislocations emerge from this highly-stressed, disordered region and propagate along {111} planes towards the NP surface. The partial dislocations are visible as red atoms because the passage of a leading Shockley partial dislocation produces a stacking fault by changing the normal ABCABC stacking sequence for FCC crystals to an ABABC stacking, e.g. a region of HCP crystal. The nucleation and propagation of partial dislocations for this orientation is similar to that observed previously when the impacting NP had its impact axis oriented along [001] [17]. Because of the differences in the angles between the impact orientations and {111} planes on which partial dislocations propagate, however, the partial dislocations that nucleate from the disordered region in the current case are localized to the region near the contact and their propagation directions occur nearly parallel to the interface between the particles. Note also that the 10˚ misorientation away from the x $[\bar{1}10]$ induces nonsymmetric deformation on the {111} planes and, therefore the deformations are not symmetric about the impact direction.

A snapshot 16 ps after impact is shown in Fig. 3.13(c) where it is observed that the impacting NP has deformed and tilted further so that it is now nearly aligned with the impacted NP orientation. There is also an increase in the density of partial dislocations and in the size of the disordered region that exists in the vicinity of the interface between the impacting and impacted particles. Examination of the impacting particle reveals that mass flow occurs radially outward between the two NPs in the disordered region (red rectangular regions). This mass flow is not symmetric and thus results in untilting of the impacting particle. The radial and asymmetric nature of this mass flow explains tilt and twist misorientations lead to very different final states. While a non-symmetric mass flow mitigates the influence of tilt misorientations, there is no corresponding mechanism that can effectively untwist misaligned particles. Since twist misorientations are more difficult to eliminate, even small twists generally lead to non-epitaxial deposition.

Fig. 3.13(d) shows the particles 24 ps after impact, where it is observed that the size of the disordered region between the now oriented NPs begins to decrease (as seen in the red rectangular regions) by recrystallization. The recrystallization growth front moves approximately vertically inward from both the top and bottom of the amorphous region. The remaining disordered atoms completely recrystallize approximately 40 ps after impact (Fig. 3.13(e)), which results in the monocrystalline NP-NP system with a large number of stacking imperfections. Note that the cross-section shown in Fig. 3.13(f) appears to show an epitaxial deposition event as the final state; however, a careful analysis shows that there is a remnant 0.88˚ misorientation between the two NPs. This very small-angle can be accommodated by a stacking fault between the two NPs.

3.4: CONCLUSIONS

In this study, the microstructures produced during high velocity particle-on-particle impacts of 2–40 nm NPs were investigated using TEM for the first time. These observations for specimens prepared with similar particle sizes and impact velocities revealed morphologies that ranged from polycrystalline to epitaxial. This suggested that there are additional impact parameters beyond the previously identified parameters of particle size and impact velocity [17] that play a role in determining whether impact leads to epitaxial or polycrystalline deposition. MD simulations were used to study parameters that cannot be controlled experimentally nor ascertained from *post mortem* observations, including particle crystallographic orientations, and particle-particle crystallographic misorientations.

Previously it has been shown that high velocity impact onto a substrate can result in complete disordering of the impacting particle for some combinations of particle size and impact velocity [17]. Upon cooling, the impacting particle was found to recrystallize with the orientation of the substrate, which resulted in epitaxial deposition. This mechanism of epitaxial deposition is favored for small particle sizes and high particle velocities. Increases in particle size necessitate even higher velocities to achieve complete epitaxy. In this chapter, an alternative mechanism for epitaxial deposition during two particle impacts was demonstrated that does not require complete disordering and is operative at lower particle velocities. We show that epitaxial deposition is favored when the impacting and impacted particle axis are both near a <110> orientation relative to the

impact direction. When small tilt misorientations away from the <110> axis were present, it was shown that asymmetric deformation and localized disordering occur, and the associated asymmetric mass flow tilts and reorients the impacting particle so that it realigns with the impacted particle. Upon cooling, the recrystallization front moves inward from both the impacting and impacted particles, consuming the disordered regions and resulting in epitaxy. It was found that this mechanism can produce epitaxial depositions for particles with tilt misorientations of at least 15˚ from the <110> impact axis for an impacting particle size of 13.6 nm and a velocity of 860 m/sec. Twist misorientations, however were shown to be much more difficult to remove and thus tend to favor polycrystalline final states.

Experiments conducted as part of this study showed a range of final states from polycrystalline to epitaxial for particles deposited with similar particle sizes and impact velocities. MD simulations showed that variations in the orientation and tilt and twist misorientations of the particles could be responsible for the experimentally observed variations in final states. Further work is needed to determine the influence of simultaneous tilt and twist misorientations between the NPs and the influence of off-center particle impacts. An understanding of the influence of these factors could lead to combinations of particle size and velocity that extend epitaxial deposition to larger ranges of tilt and twist misorientations.

3.5: REFERENCES

1. T. Stoltenhoff, H. Kreye, H.J. Richter, J. Therm. Spray Tech. 11, 542 (2002).
2. C. Borchers, T. Stoltenhoff, F. Gartner, H. Kreye, H. Assadi, In: Proceedings of the Materials Research Society Conference, San Francisco, CA, Apr 17-19, 2001; vol. 673: p 7.
3. H. Assadi, F. Gärtner, T. Stoltenhoff, H. Kreye, Acta Mater. 51, 4379 (2003).
4. A. Schroth, R. Maeda, J. Akedo, M. Ichiki, Jpn. J. Appl. Phys. 37, 5342 (1998).
5. J. Akedo, M. Ichiki, K. Kikuchi, R. Maeda, Sensors and Actuators A: Physical. 69, 106 (1998).
6. W.T. Nichols, G. Malyavanatham, M.P. Beam, D.E. Henneke , J.R. Brock , M.F. Becker, J.W. Keto, In: Mat. Res. Soc. Symp. Proc., Nanophase and Nanocomposite Materials III, Materials Research Society , Warrendale, PA, 2000, editted by: Komarneni S, Parker JC, Hahn H; vol. 581: p 193.
7. G. Malyavanatham, D.T. O'Brien, M.F. Becker, W.T. Nichols, J.W. Keto, D. Kovar, S. Euphrasie, T. Loue, P. Pernod, J. Mat. Proc. Tech. 168, 273 (2005).
8. C. Huang, W.T. Nichols, D.T. O'Brien, M.F. Becker, D. Kovar, J.W. Keto, J. Appl. Phys. 101, 064902 (2007).
9. C. Borchers, F. Gartner, T. Stoltenhoff, H. Assadi, H. Kreye, J Appl Phys. 93/12, 10064 (2003).
10. C. Borchers, T. Schmidt, F. Gärtner, H. Kreye, Applied Physics A. 90, 517 (2008).
11. M. Lebedev, J. Akedo, T. Ito, Journal of Crystal Growth. 275, 1301 (2005).
12. D. Mordehai, M. Kazakevich, D.J. Srolovitz, E. Rabkin, Acta Mater. 59, 2309 (2011).
13. J.R. Greer, W.D. Nix, Phys. Rev. B. 73, 245410 (2006).
14. J. Akedo, M. Ichiki, K. Kikuchi, R. Maeda, In: Proceedings of the 1997 10th Annual International Workshop on Micro Electro Mechanical Systems, MEMS: 1997 Jan 26-30; IEEE, Piscataway, NJ, USA. Nagoya, Jpn: 1997. p 135.
15. C. Huang, M.F. Becker, J.W. Keto, D. Kovar, J. Appl. Phys. 102, 054308 (2007).

16. M. Nahar, PhD Dissertation (University of Texas at Austin, 2012).
17. T.V. Chitrakar, J.W. Keto, M.F. Becker, D. Kovar, Acta Mater. 135, 252 (2017).
18. M. Nahar, I.F. Gallardo, K.L. Gleason, M.F. Becker, J.W. Keto, D. Kovar, J. Nanopart. Res. 13, 3455 (2011).
19. M.A. Asoro, D. Kovar, P.J. Ferreira, Chem. Comm., 50/37, 4835 (2014).
20. S. Plimpton, J Comp Phys. 117, 1 (1995) (http://lammps.sandia.gov).
21. Lonestar Linux Cluster, TACC (http://www.tacc.utexas.edu).
22. P.L. Williams, Y. Mishin, J.C. Hamilton, Modelling Sim. Mater. Sci. Eng. 14, 817 (2006) (http://www.ctcms.nist.gov/potentials/Ag.html).
23. H. Haberland, Z. Insepov, M. Moseler, Phys. Rev. B. 51, 11061 (1995).
24. Q. Hou, M. Hou, L. Bardotti, B. Prevel, P. Melinon, A. Perez, Phys. Rev. B. 62/4, 2825 (2000).
25. W. Shinoda, M. Shiga, M. Mikami, Phys Rev B. 69, 134103 (2004).
26. A. Stukowski, Modelling Simul. Mater. Sci. Eng. 18, 015012 (2010).
27. P.M. Larsen, S. Schmidt, J. Schiøtz, Modell. Simul. Mater. Sci. Eng. 24, 055007 (2016).
28. D.B. Williams, C.B. Carter, *Transmission Electron Microscopy: A Textbook for Materials Science* (Springer, New York, 2009).
29. K. Meinander, K. Nordlund, Phys. Rev. B. 79, 235431 (2009).
30. D. Hull, D.J. Bacon, *Introduction to Dislocations* (Butterworth-Heinemann, Oxford, GB, 2011).
31. A. Tolvanen, K. Albe, Beilstein J. Nanotechnol. 4, 173 (2013).
32. H. Tsuzuki, J.P. Rino, P.S. Branicio, J. Phys. D: Appl. Phys. 44, 055405 (2011).

CHAPTER 4: Influence of Crystallographic Orientation on the Deformation of Ag Nanoparticles during High Speed Impact

4.1: INTRODUCTION

In Chapter 2 we observed that for a range of nanoparticle (NP) sizes and impact velocities, NP deformation was governed by a rigid-pyramidal structure created by the locking of propagating partial dislocations, which lead to a significant straining of the atoms outside of the pyramidal structure [1]. The same mechanism was also observed at higher velocities, but with an increased magnitude of the strains that resulted in an almost complete disordering of the impacting NP. A wide range of final states ranging from polycrystalline to epitaxial containing a considerable number of defects were observed for a combination of NP sizes and impact velocities. These NP impacts were however studied for a fixed NP-substrate orientation where the nanoparticle was oriented with the same orientation as the flat (001) Ag substrate except with a 45˚ rotation about its impact *z* [001] direction. In chapter 3, a similar range of final states ranging from polycrystalline to epitaxial were observed experimentally using TEM for nominally similar particle sizes and impact velocities which suggested that these are not the only parameters that influence final morphologies [2]. Keeping the NP size and impact velocity fixed, MD simulations were conducted for different particle crystallographic orientations and particle-particle crystallographic misorientations where a range of both deformation behavior and final microstructures were observed for these simulations. Thus, NP

crystallographic orientation is another impact parameter that has to be thoroughly examined, and it is important that we understand how the deformation mechanisms evolve and change for different crystallographic orientations of the NP to understand NP deformation in further detail.

In this chapter, MD simulations of the impact of an Ag NP of fixed size and impact velocity onto a substrate with a fixed crystallographic orientation are conducted to understand the influence of impacting particle orientation on the deformation of the NPs. We first consider an impacting NP with the same orientation as the substrate and then consider the influence of NP orientation as the NP is rotated about specific coordinate axes from 0˚–45˚.

Schmid factor analysis is the traditional tool used to predict the influence of orientation on onset of deformation in crystals [3]. This analysis suggests that deformation is favored in orientations with high values of the Schmid factor. Thus, it was first hypothesized that there should be a correlation between the total deformation experienced by NPs (characterized by comparing the predicted aspect ratios from simulations) and the theoretically calculated Schmid factors. Simulations, however, suggested that the orientation dependence for impacting particles is more complicated and that a simple Schmid factor analysis cannot predict the magnitude of the total deformation. Additional simulations were then conducted for cases where maximum and minimum deformations were observed to study the underlying deformation mechanisms.

4.2: PROCEDURE

Molecular dynamics (MD) simulations were conducted using LAMMPS [4] implemented on the Lonestar Linux cluster at the Texas Advanced Computing Center (TACC) [5] at the University of Texas at Austin to study the influence of crystallographic orientations of Ag NPs onto a stationary Ag substrate. The Ag atomic interaction was described by the embedded-atom-method (EAM) potential [6]. The simulation volume was 60 × 60 × 80 lattice constants (lattice constant = 0.409 nm for Ag) with periodic boundary conditions applied in all three dimensions for the simulation volume. The substrate consisted of the bottom-half of the simulation volume (60 × 60 × 40 lattice constants).

Spherical NPs with a fixed diameter of 4.5 nm (~2,750 atoms) were impacted at a fixed velocity of 300 m/sec onto a flat substrate that had a fixed crystallographic orientation with Miller indices of *x* [100], *y* [010], *z* [001]. The impact orientations of the particles were systematically varied to assess the influence of particle orientation on deformation following impact. At the start of each simulation, the impacting NP was placed 20 lattice units above the substrate so that it did not touch the simulation box boundary, which was equivalent to the NP floating in vacuum. Before the NP was set in motion in the *z* direction, the Ag atoms in the NP were thermalized at 300 K for 40 ps. This temperature is consistent with the experimental conditions used to impact NPs [7] via the LAMA process. To prevent undesirable NP rotations during thermalization, the angular momentum of the impacting NP was zeroed at every time-step during

thermalization. The NP-substrate system was prevented from moving out of the simulation volume by zeroing the linear momentum at every timestep for the bottom 50% of the stationary substrate during impact. Nose-Hoover style, non-Hamiltonian equations of motion were used on the isothermal-isobaric (NPT) ensemble [8] to perform the time integration for the equilibration of the system to 300 K and for the subsequent impact at a time step frequency of 0.001 ps (1 fs). The atomic trajectories and velocities were calculated for every time step.

The deformation of the NP following the impact event was evaluated by capturing atomic positions at intervals of 50 ps for the first 300 ps after impact, after which the deformation and microstructure was no longer noticeably evolving. Since most of the deformation occurred in the first few picoseconds after impact, the positions of all atoms in selected additional simulations were then recorded at intervals of 0.25 ps for the first 10 ps after impact to study the deformation mechanisms that are responsible for the range of observed behavior. The software program OVITO [9] was used to visualize the atomic positions and polyhedral template matching (PTM) [10] was used to determine the local atomic stacking sequence. The visualizations were color-coded with this information, with green representing local regions of FCC stacking and red representing regions with a local HCP stacking. When the atomic stacking sequence could not be identified (e.g. at grain boundaries or where the atoms were disordered), atoms were colored white. A cutoff value of the root-mean-square deviation (RMSD) threshold of 0.15 was used in our simulations, which produced results that agreed with visual inspections of ordered and disordered regions of the simulations.

From previous studies, it is known that the nucleation and motion of partial dislocations plays a large role in the deformation behavior of impacting NPs [1]. The Schmid factor [3] is a measure of the resolved shear stress (τ_R) acting on specific atomic planes in specific directions during application of a global uniaxial stress (σ) along a specific impact axis and therefore it is a quantifiable measure of the driving force for dislocation motion. The Schmid factor is obtained by the following relation:

$$\tau_R = \sigma \times (\cos\Phi \times \cos\theta)$$

where Φ is the angle between the impact axis and the normal to the slip plane,

θ is the angle between the impact axis and the slip direction,

$(\cos\Phi \times \cos\theta)$ is the Schmid factor.

For a given uniaxial stress (σ) along the impact axis, slip is expected to occur for the lowest resolved shear stress (τ_R) on a specific slip plane along a specific slip direction corresponding to the highest Schmid factor.

In FCC systems, slip can occur along any of the four equivalent {111} planes and in any of the three equivalent <110> directions that lie in each {111}. Thus, there are 12 possible geometric slip systems. The Schmid factor was calculated for each impact direction for all 12 slip systems to determine if it is a useful parameter in understanding Ag NP deformation. The Schmid factors were compared to the deformations experienced by the NPs upon impact from MD simulations. The magnitudes of the deformations were quantified from the measured aspect ratios, defined as the ratios of maximum width (w) to maximum height (h), which were obtained from the final states of the impacted particles taken 300 ps after impact.

In order to isolate the effects of NP crystallographic orientation on the deformation of the NP, for the first simulation, the impacting NP had the same orientation as the substrate. For the next set of simulations, the NP impact axis was rotated about the *z* [001] axis at 5˚ intervals up to a maximum misorientation of 45˚. The symmetry of the system dictates that rotation larger than 45˚ duplicate the misorientations probed within the 0–45˚ interval and therefore it is not necessary to perform simulations with rotations larger than 45˚. For the next set of simulations, the NP impact axis was rotated about the *y* [010] axis at 5˚ intervals up to a rotation angle of 45˚. Note that for rotations about the *y* [010] axis, there is a different impact axis for each rotation.

For the last set of simulations, the NP was impacted at specific directions obtained from a standard triangle from a stereographic projection. The impact axes for the NP were obtained by a sequential combination of rotations with respect to the fixed coordinate axes of the substrate in the following order: the first rotation was performed about the fixed *z* [001] axis of the substrate till the required NP impact axis lay on the *x*-*z* plane of the substrate coordinate system, and the second rotation was performed about the *y* [010] axis of the substrate till the rotated NP impact axis coincided with the substrate *z* [001] axis. For this set of simulations, this combination of rotations provided the desired impact axis along which the NP impacted on the substrate with the given fixed orientation. There are standard notations used to denote rotations between coordinate systems such as the euler angle notations proposed by Bunge, Kocks, Matthies and Roe [11]. Although we have not used a standard method of rotation of coordinate systems, the simultaneous *z* and *y* axis rotations used in this last set of simulations are intuitive to

understand with respect to the previous sets of simulations where the NP was oriented as a consequence of either a pure *z* or a *y* axis rotation with respect to the fixed substrate. For this set of simulations it is also important to note that for certain NP impact axes including [313], [212], [535] and [111], the second rotation about the *y* [010] axis of the substrate exceeds 45˚.

A snapshot taken from a simulation before impact is shown in Fig. 4.1(a) from a representative simulation. A schematic of an impacted particle on a substrate and the variables needed to evaluate the deformation parameters are shown in Fig. 4.1(b). This figure illustrates the parameters needed to calculate the Schmid factor including the axis of impact, the slip plane normal, the slip plane direction, the angle between the impact axis and the slip plane normal (Φ), and the angle between the impact axis and the slip direction (θ). This figure also shows the height (h) and width (w) of the deformed particle used in quantifying the aspect ratio.

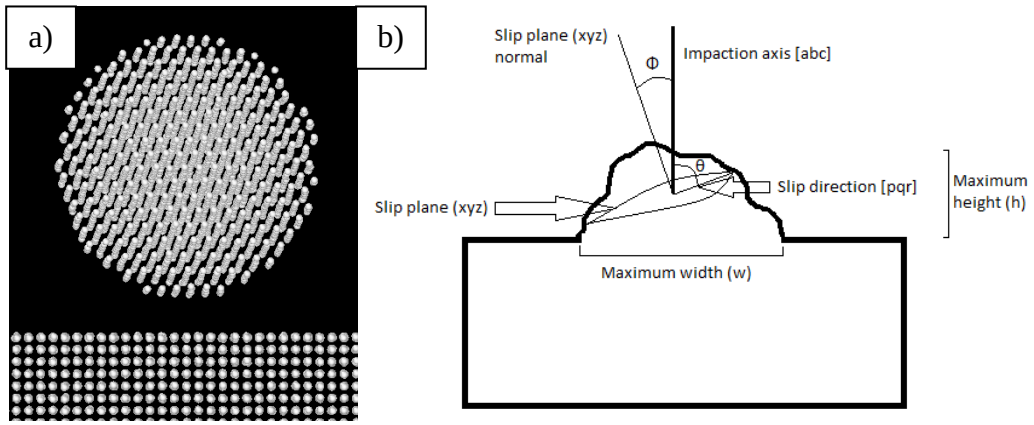

Figure 4.1: a) Snapshot taken from MD simulation of the NP and substrate surface before impact. This impacting NP orientation has the Miller indices: *x* [$1\bar{1}0$], *y* [$11\bar{2}$], *z* [111] and the substrate orientation has the Miller indices: *x* [100], *y* [010], *z* [001]. b) Schematic of the NP and substrate following impact showing the variables needed to evaluate the aspect ratio and Schmid factor.

4.3: RESULTS AND DISCUSSION

One hypothesis is that the magnitudes of the deformations experienced by the impacting NPs are correlated to the driving force to initiate deformation and therefore are correlated to the Schmid factors. To test this hypothesis, the calculated Schmid factors and the measured aspect ratios obtained from the final states from the simulations are plotted as a function of the rotation axes of the impacting NP with respect to the fixed substrate in Figs. 4.2(a) and (b), respectively. The origins in both the contour plots corresponded to the *z* [001] direction of the substrate and all rotations are plotted with respect to this axis. The numbers in parentheses on the plots are the Miller indices for specific impact directions and the numbers to the right are the measured aspect ratios for these directions. The smallest Schmid factor is observed when the NP impact axis is aligned along [111]. NP impact axes rotated such that they have a 20–25˚ misorientation about the *y* [010] axis have the highest Schmid factors. The Schmid factors remain high for 20–25˚ misorientations about the *y* [010] axis that also include simultaneous rotations about the z [001] by up to about 30˚.

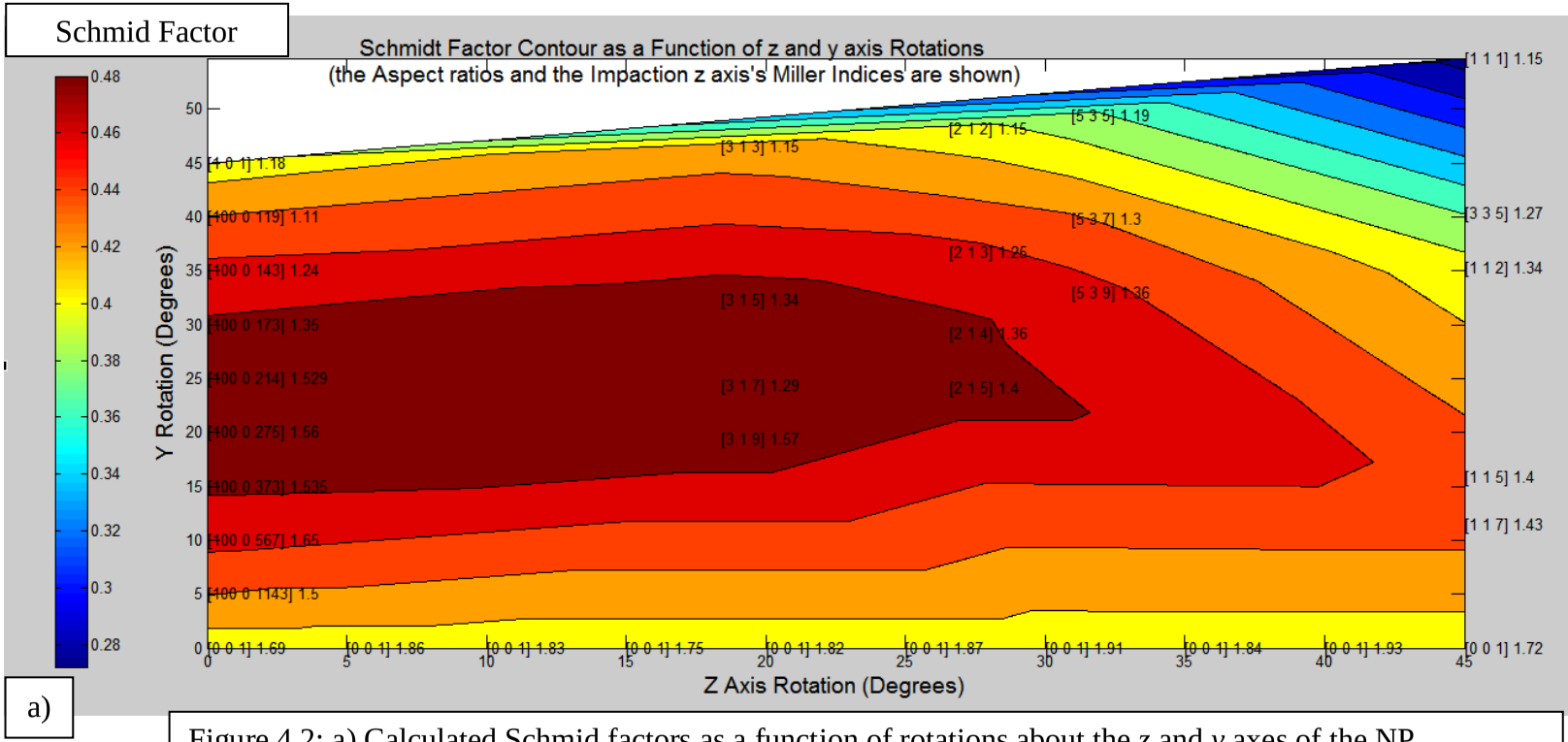

Figure 4.2: a) Calculated Schmid factors as a function of rotations about the *z* and *y* axes of the NP

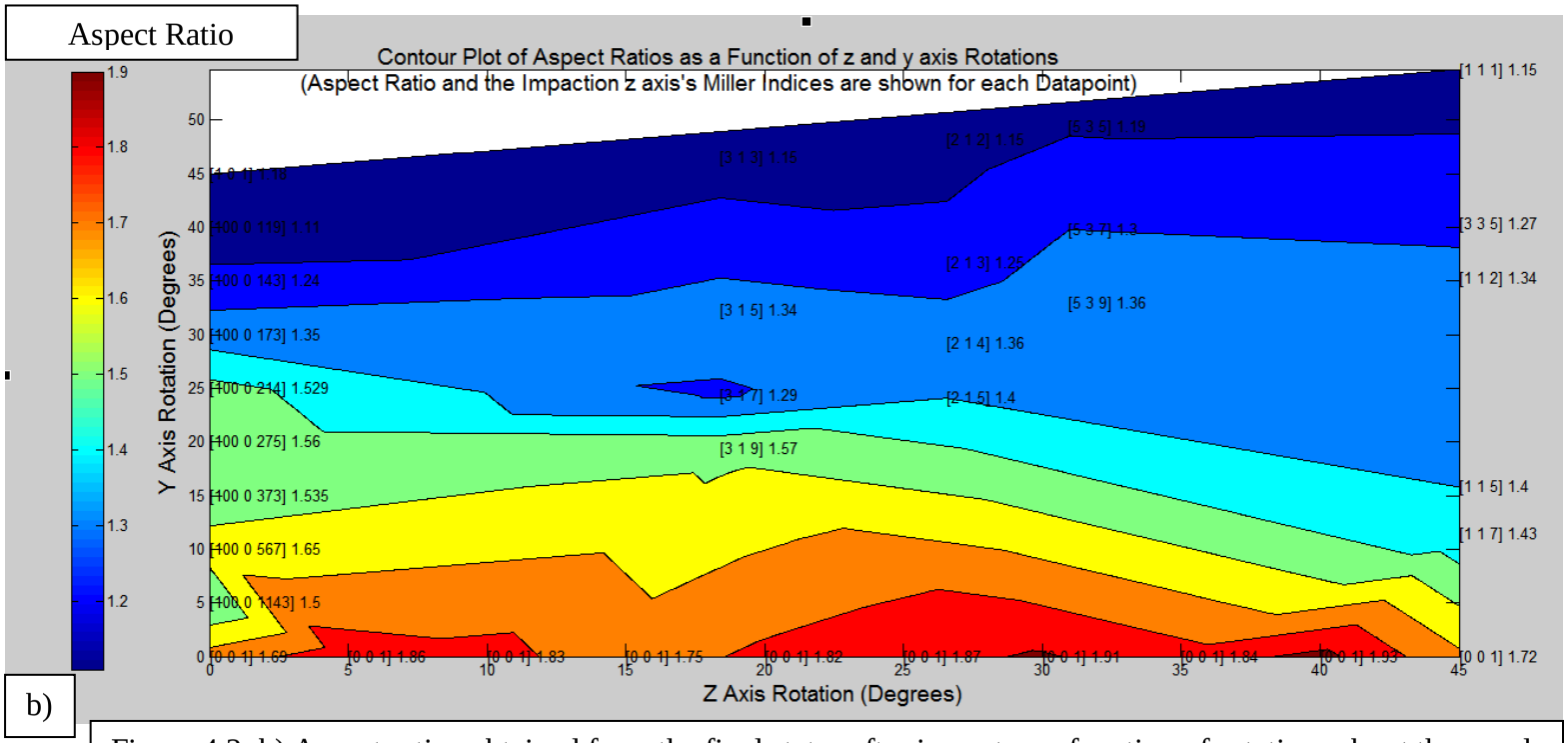

Figure 4.2: b) Aspect ratios obtained from the final states after impact as a function of rotations about the *z* and *y* axes.

Based on the hypothesis and Fig. 4.2(a), it would be expected that NPs that exhibit the greatest deformation would have impact axes that were rotated by 20–25˚ about the *y* [010] and the lowest deformations would be experienced along the [111] impact axis. However, Fig. 4.2(b) shows that the Schmid factor predictions are inconsistent with the measured aspect ratios since the lowest deformation is observed not only for NPs with their impact *z* axis aligned along [111] but also for all axes on the trace connecting [111] and [101]. Also, the highest deformation is observed when the *z* axis is aligned along [001], which also includes NP rotations about [001], and only modest deformations are obtained in directions where the Schmid factor predicts the highest deformations. This shows that a simple Schmid factor analysis where dislocation motion is expected to occur on a single plane with the highest resolved stress does not explain the magnitudes of the deformations obtained during the high-velocity deposition of NPs.

The Schmid factor analysis that was performed was strictly for {111} <110> slip, which we showed in Chapters 2 and 3 is not typically predicted to be the active slip system during high velocity NP impact. Instead, we typically predict {111} <112> slip which involves the motion of leading and trailing partial dislocations. The Schmid factor analysis that was performed is also relevant for characterizing the motion of (leading + trailing) partial dislocation slip since the directions that simultaneously maximize the driving force for the motion of both leading and trailing partial dislocations is the <110>. In other words, applying a shear stress parallel to the direction of the leading partial dislocation will tend to be more favorable than applying a shear stress along a <110> but

it will be less favorable to moving the trailing partial dislocation. If you want to move both, then the <110> is the best direction and our analysis is applicable.

There are many other possible Schmid factor analyses that could be considered, but our results show that no single Schmid factor analysis will be capable of predicting the deformation behavior because the deformation is driven by a complex sequence rather than deformation on any single slip system. Four sets of additional simulations corresponding to the lowest and highest deformation observed from the measured aspect ratios were therefore studied to further understand these deformation mechanisms that are responsible for the range of deformations in the impacted NPs.

Deformation Mechanisms for Soft Orientations

Orientations in which the deformations were extensive are termed a "soft" orientation, whereas orientations that produced relatively little overall deformation are termed "hard." Severe deformation with high aspect ratios (≈ 1.7–1.9) were observed in the first set of simulations when the NP was aligned along the [001] impact direction. Furthermore, the aspect ratios did not vary significantly when the NP was rotated about the impact *z* [001] axis. Two of these simulations were studied in more detail to observe the deformation mechanisms that resulted in extensive deformation as well as to understand why NP rotation about the *z* [001] axis did not affect the deformation significantly. Snapshots of central cross sections of the NP-substrate system containing 4 atomic layers and which are color-coded for the PTM values are shown at specific times after impact for the studied cases in the sections that follow. For most of these snap shots,

{110} cross-sections for the impacting NP were selected so that the simulations could be directly compared.

NP and Substrate with the Same Orientation

For these simulations, the NP and the substrate are both oriented with the Miller indices: *x* [100], *y* [010], *z* [001]. Fig. 4.3 shows the time evolution of the microstructure of the NP-substrate system following impact.

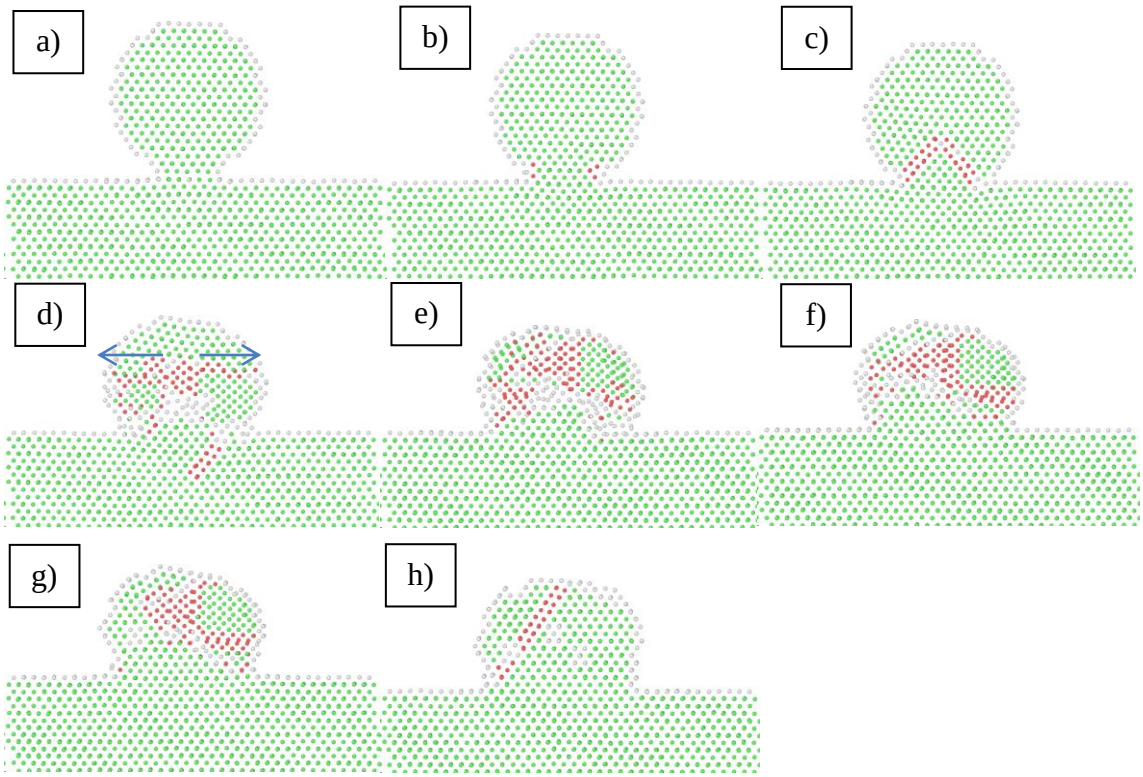

Figure 4.3: PTM snapshots showing a {110} view of the time evolution of the microstructure of the NP upon impact on the flat substrate at a) 0 ps (time after impact), b) 0.75 ps, c) 1.5 ps, d) 4 ps, e) 6 ps, f) 8 ps, g) 10 ps and h) 310 ps (final state). The NP and the substrate are oriented along the [001] impact axis. In d), arrows denote the directions of the moving partial dislocations.

Fig. 4.3(a) shows that the lattices of the NP and substrate following impact are initially aligned. At the early time steps (t = 0.5–2 ps after impact), deformation is highly localized to the near-contact region, where the hydrostatic strains are relatively large. A careful examination of these regions in Fig. 4.3(b) shows that partial dislocations are emitted from the edges of the contact zone between the particle and substrate, and then propagate on {111} planes into the NP. As shown in Fig. 4.3(c), these partial dislocations intersect, resulting in a pyramid-like feature bounded by stacking faults that are at an angle of $\sim$ 65–70˚ relative to the impact direction [1]. The intersection of the partial dislocations produces a lock which prevents further motion of the partial dislocations. As the NP continues to move downward, the contact area between the particle and substrate expands outward, leading to additional partial dislocations that nucleate from the edges of the expanding contact zone and propagate parallel to the partial dislocations that formed the initial pyramid (Fig. 4.3(b)). It has been shown previously [1] that this pyramidal feature acts like a rigid wedge as the upper part of the NP continues to move downward over the pyramid. As a result, the horizontally oriented (100) planes above the pyramid bend about the pyramid apex (see Fig. 4.3(c)). From Fig. 4.3(d), it is apparent that there are two mechanisms for relaxing the severe strains that accumulate locally in this region above the apex: 1) the atoms begin to disorder and then deform by viscous flow and 2) additional partial dislocations nucleate from the pyramid apex and propagate outward towards the NP surface. At longer times the NP stops moving down and deforming, and the disordered atoms begin to recrystallize with an epitaxial relationship with the substrate atoms, as shown in Fig. 4.3(e). The stacking faults that were produced by partial

dislocations are eliminated by disordering, but new partial dislocations nucleate and propagate upwards from this region. Following complete recrystallization (Fig. 4.3(f)), the grain boundary starts migrating upwards and, on the left of the NP, consume the defected regions (Fig. 4.3(g)). After 310 ps, the final state is reached (Fig. 4.3(h)) where it is apparent that the expanding grain boundary has consumed the entire NP such that the particle and substrate share a common orientation; we refer to this as an epitaxial deposition. A few stacking faults are generated by rapid recrystallization, which can be explained by Growth Accident Theory [12] and one of these defects is shown in the cross-section shown in Fig. 4.3(h). It is important to note that most of the deformation experienced by the NP occurs within ~ 4–10 ps after impact. Thus, the significant evolution of the microstructure that is observed 10–310 ps after impact does not influence the deformation of the NP.

NP Rotated by 45˚ About the Impact *z* [001] Axis

For these simulations, the NP was rotated about its impact *z* [001] axis by 45˚ with the Miller indices: *x* [110], *y* [$\bar{1}$10], *z* [001]. Comparing this simulation (Figs. 4.4(a-f)) to the previous one where the NP and the substrate had the same orientation, it is apparent that both cases result in significant deformation of the NP upon impact.

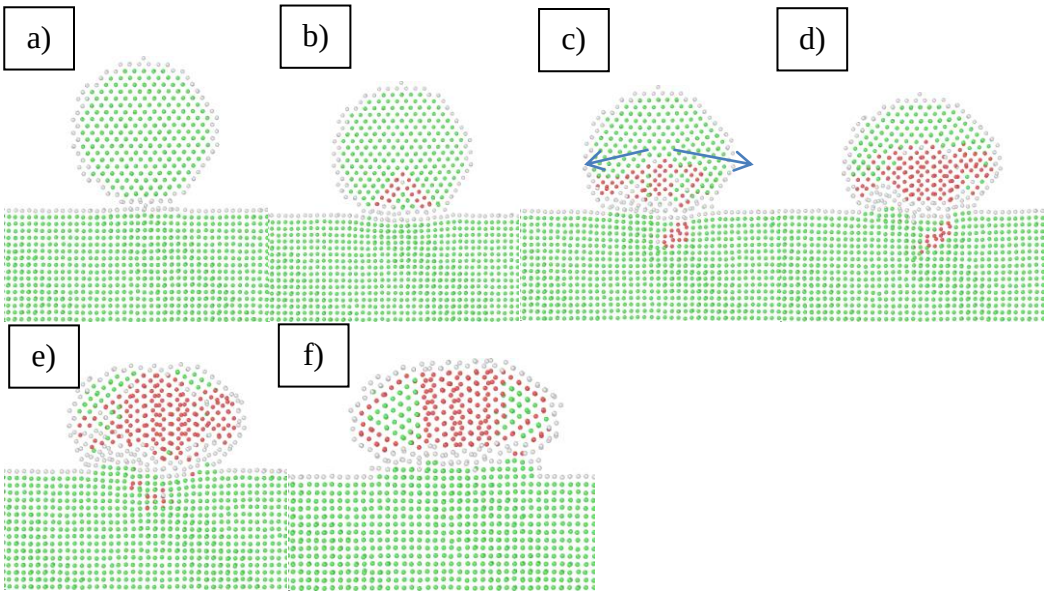

Figure 4.4: Snapshots in time showing a {110} view of the NP and of the time evolution of the deformation and microstructure of the NP upon its impact at a) 0 ps, b) 1.25 ps, c) 2.5 ps, d) 3.5 ps, e) 5 ps and f) 310 ps (final state). The NP is rotated about the [001] impact axis by 45˚ relative to the substrate prior to impact. In (c), arrows denote the directions of the moving partial dislocations.

Fig. 4.4(a) shows the misorientation in the lattices of the NP and the substrate at the onset of impact. The deformation is initially localized to the near contact region where a pyramidal feature is generated by the intersection of partial dislocations emerging from the contact zone where there are large hydrostatic strains, as was observed in the earlier simulation (Fig. 4.4(b)). However unlike the previous case, the atoms near the contact zone disorder immediately upon impact due to the additional lattice misorientation between the NP and the substrate at the impact surface. The pyramidal feature expands as the contact area spreads and the horizontally aligned (100) planes of atoms above the pyramidal apex begin bending, as seen in Fig. 4.4(c). The strains are relieved by the nucleation and propagation of partial dislocations outward from the apex

towards the NP surface. In the previous simulation, recrystallization of the disordered atoms was followed by a rapid growth of the epitaxial grain boundary upwards. However, in this case, the lattice misorientation between the NP and the substrate impedes epitaxial growth near the contact surface. Instead, the deformation of the NP that is still moving downwards is due to nucleation and propagation of new partial dislocations from this misoriented zone. This relieves strains along other {111} planes not visible in this cross-section, as shown in Figs. 4.4(d) and (e). Most of the stacking faults produced by these partial dislocations remain in the NP until at least the final state at 300 ps. Unlike the previous case where epitaxial growth occurred through most of the impacting particle, in this case epitaxial growth is restricted to only 1 or 2 atomic layers, as shown in Fig. 4.4(f). Thus, in the final state the NP contains a large number of stacking faults and the deposition is not epitaxial since a grain boundary remains between the impacted particle and substrate.

Although the simulations for the soft impact orientations shown in Figs. 4.3 and 4.4 exhibit similar magnitudes of the overall deformation, it is apparent that the rotation introduced between the NP and the substrate in Fig. 4.4 has a significant effect on the microstructural evolution of the deposited particle. In order to further study this effect, the von Mises equivalent strain, ε_{eq} was calculated for the first few time-steps after impact. The von Mises equivalent strain is a measure of the shear strain that causes distortion, but does not result in a volume change, and thus is a measure of the driving force for partial dislocation motion. The von Mises strains are plotted at 0.5 and 1.75 ps after impact for both of the soft orientations in Fig. 4.5.

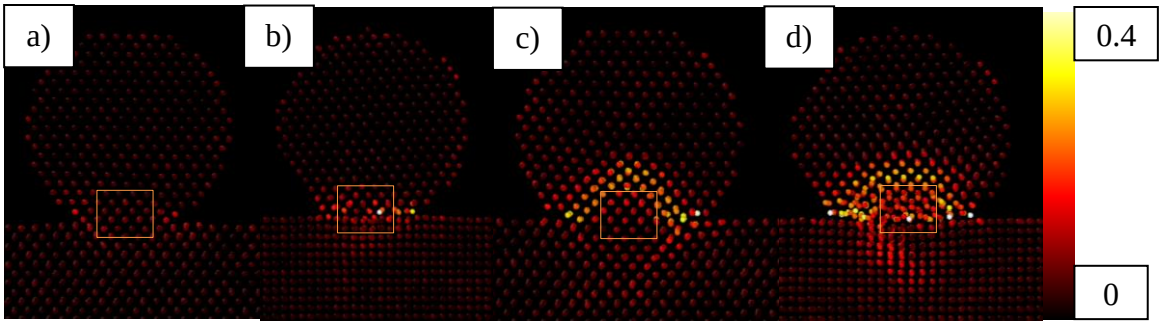

Figure 4.5: Snapshots of the von Mises strain a) 0.5 ps after impact for the case where the NP and substrate are initially aligned, b) 0.5 ps after impact for the case where the NP is rotated by 45˚about the *z* [001] impact axis, c) 1.75 ps after impact for the case where the NP and substrate are initially aligned and d) 1.75 ps after impact for the case where the NP is rotated by 45˚about the *z* [001] impact axis. The color coding of the scale bar is attached which indicates the magnitude of the von Mises strain. Note the differences that are apparent in the von Mises strain for in the central contact region demarcated by the rectangular boxes.

When the particle and substrate are initially aligned (Fig. 4.5(a)), we observe that the von Mises strain is relatively modest, whereas misorientation between the particle and substrate result in larger von Mises strains and atomic disorder near the contact region (Fig. 4.5(b)). At longer times, after the pyramidal feature has formed and has started to disorder 1.75 ps after impact, the von Mises strain is larger by a factor of ~ 4 in the disordered contact region (Fig. 4.5(d)) when the NP and substrate are misoriented compared to the relatively ordered contact region when the NP and substrate share the same orientation (Fig. 4.5(c)). This high von Mises strain is responsible for the large number of partial dislocations that nucleate and propagate in the misoriented NP compared to the aligned NP.

Deformation Mechanisms for Hard Orientations

Two additional simulations were studied to understand the deformation mechanisms for hard orientations. From Fig. 4.2 (b), it is apparent that the hardest orientations (aspect ratios ≈ 1.15–1.2) occur for NP orientations along [111] or [101].

NP Impact Axis Along [111]

For these simulations, the impacting NP is oriented along [111] with the Miller indices: *x* [$11\bar{2}$], *y* [$\bar{1}10$], *z* [111]. Fig. 4.6 shows the time evolution of the microstructure of the NP-substrate system following impact.

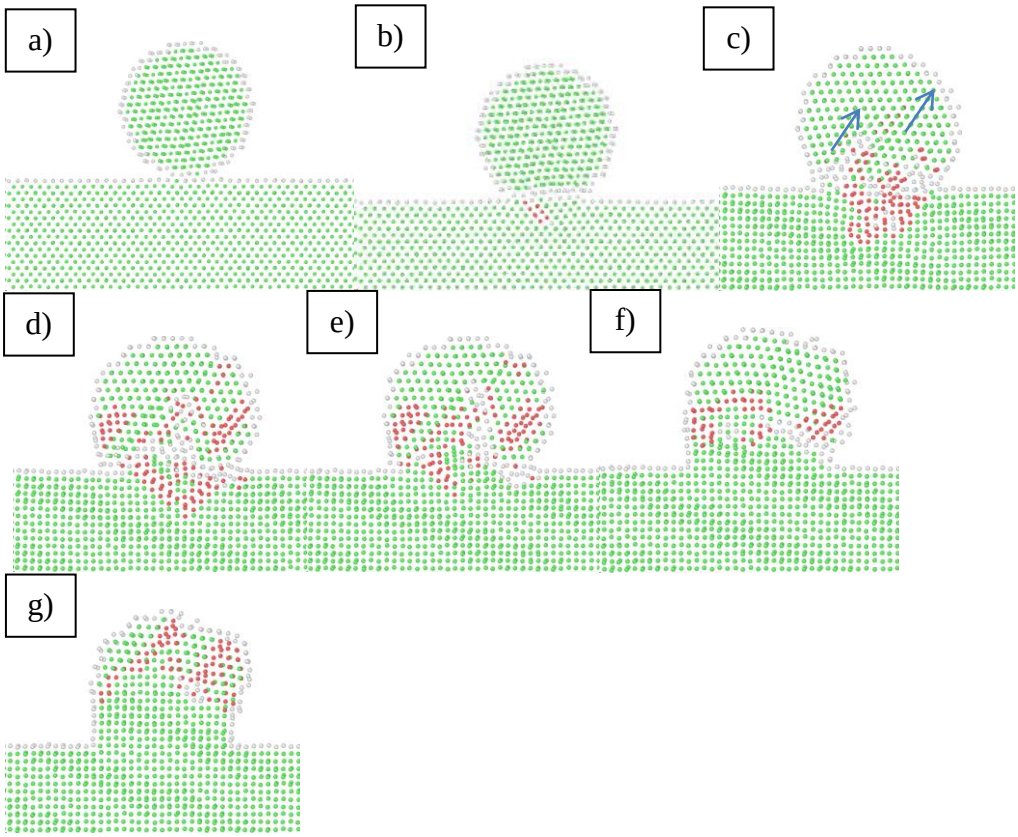

Figure 4.6: Snapshots showing the time evolution of the microstructure: a) 0 ps (after impact), b) 0.75 ps, c) 2.5 ps, d) 4.5 ps, e) 5 ps, f) 10 ps and g) 310 ps (final state). For all snapshots except a) and b), a {110} view of the NP is shown; for a) and b) a {110} view of the substrate is shown. The arrows in (c) denote the direction of the propagating partial dislocations.

The initial misorientation between the NP and the substrate is visible in Fig. 4.6(a). As was observed for soft orientations, the deformation upon impact is initially localized to near the contact region between the NP and the substrate. Due to the relative orientations of the impact axis and the close-packed {111} planes, the pyramidal feature observed for the soft orientations is not observed in this hard orientation. However, the lattice misorientation between the NP and the substrate still produces a relatively highly stressed contact region that results in the nucleation and propagation of partial

dislocations in {111} in both the substrate (Fig. 4.6(b)) and NP (Fig. 4.6(c)).Although the (001) atomic planes were observed to bend severely during impact in soft orientations, the parallel (111) atomic planes in this case do not bend for this hard orientation because of the absence of the rigid wedge-like pyramid feature. As the NP moves down, the contact region expands leading to further nucleation and propagation of partial dislocations towards the NP surface along a specific {111} plane (and along other {111} planes not visible in this cross-section) which is seen in Fig. 4.6(d). Since there is almost no disordering-recrystallization because the strains are much lower in the absence of the pyramidal feature, most of the deformation is accommodated by nucleation and propagation of partial dislocations.

It is apparent that there is significant motion of partial dislocations into the substrate, which was not evident for impact in soft orientations (Fig. 4.6(d)). The resulting substrate deformation accommodates the deformation of the NP-substrate, which is another reason for less deformation in the NP. In order to relax the residual strains in the substrate, the partial dislocations either retreat to the contact surface or trailing partial dislocations nucleate that retrace the paths of the leading partial dislocations (Fig. 4.6(e)). Either of these scenarios will eliminate stacking faults and return the lattice to a defect-free state, but the time steps between snapshots was too long to ascertain which scenario actually occurs. A similar mechanism is apparent in the NP where the density of partial dislocations is also observed to decrease with time (Fig. 4.6(f)). Lastly, the grain boundary between the NP and the substrate also begins to propagate upwards into the NP. The final state is shown in Fig. 4.6(g) after 310 ps, where

the epitaxial front has propagated upward by a few more atomic layers. The final state of the NP-substrate system is still polycrystalline with a large number of stacking faults emerging from the moving grain boundary [12]. Comparing this simulation to that shown in Fig. 4.4 for the soft [001] impact axis with a 45˚ rotation relative to the substrate prior to impact, we observe that the grain boundary here has advanced further into the nanoparticle.

NP Aligned Along [101]

In this simulation, the impacting NP is oriented along [101] with the Miller indices: *x* [$10\bar{1}$], *y* [010], *z* [101]. Fig. 4.7 shows the time evolution of the microstructure of the NP-substrate system following impact.

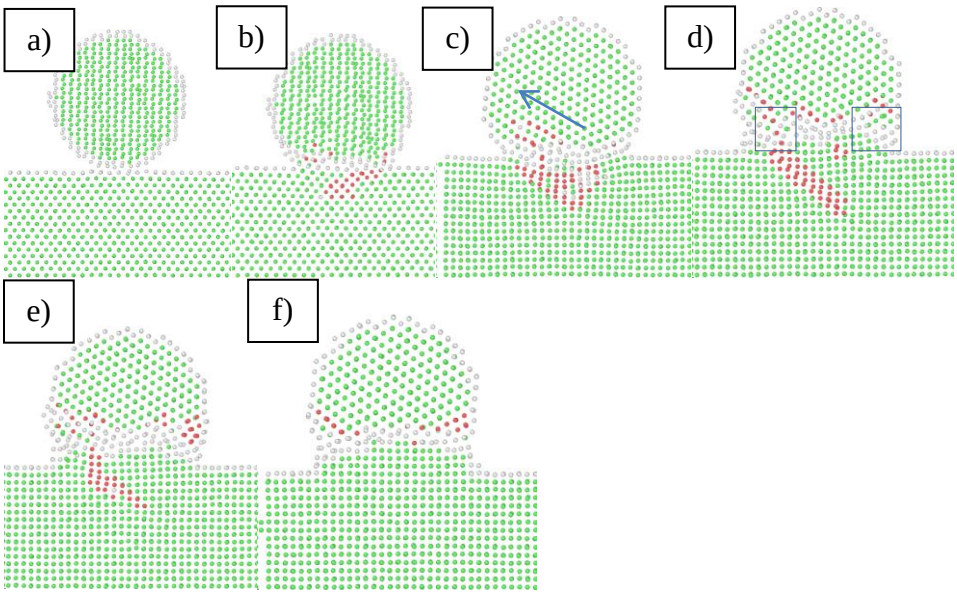

Figure 4.7: Snapshots showing the time evolution of the microstructure after impact: a) 0 ps (after impact), b) 1.5 ps, c) 2.5 ps, d) 4.5 ps, e) 5.5 ps and f) 310 ps (final state). For all snapshots except a) and b), a {110} view of the NP is shown; for a) and b) a {110} view of the substrate is shown. The arrow in (c) denotes the direction of the propagating partial dislocations.

The NP-substrate misorientation is evident in Fig. 4.7(a) upon impact. In Fig. 4.7(b), during the initial stages of impact, the deformation is localized near the contact area, with partial dislocations nucleating from this zone, as was observed in the previous simulation for the other hard orientation. However, in this case the partial dislocations propagate nearly horizontally (Fig. 4.7(c)) rather than upwards towards the NP surface, as was observed in the earlier simulation. This occurs because the partial dislocations are following the orientations of the most favorably oriented {111} planes, where the von Mises stresses are highest and these planes make a very small angle with the contact surface for this impact orientation. Thus, most of the deformation in this case is concentrated near the contact region and the upper regions of the NP retain their pre-

impact orientation. Similar to the case shown in Fig. 4.6 for the other hard orientation, the motion of partial dislocations into the substrate in this case results in significant deformation in the substrate. The large disordered contact region for this case induces viscous flow that further increases the contact area beween the NP and the substrate, as seen in the regions marked by rectangles in Fig. 4.7(d) [2]. This disordered region spreads near the NP-substrate interface, consuming the stacking faults, which is followed by the propagation of the grain boundary by a few atomic rows upwards, as seen in Fig. 4.7(e). When the NP has stopped moving, the partial dislocations in the substrate are removed by either the retreat of leading partial dislocations or by the nucleation of trailing partial dislocations. Thus, the final state is observed in Fig. 4.7(f) to be polycrystalline with a small number of stacking faults in the NP.

In summary, the decrease in the overall deformation of the NP observed for the simulations conducted for hard orientations can be attributed to the absence of favorably oriented {111} where the von Mises stress can propagate partial dislocations. The rigid wedge-like pyramidal feature that formed from the intersection of {111} planes in the soft orientations resulting in significant deformation did not form in the hard orientations. The primary mechanisms for limited deformation observed in these orientations can be attributed to partial dislocations that originate from the contact zone (for the <111> type hard impact orientations) and the viscous mass flow produced by the disordered region (for the <101> type hard impact orientations).

For the simulations that were conducted in this chapter, the substrate thickness

was proportionately increased with particle size to reduce the effects of momentum transfer from the particle to the substrate as the particle size was increased. In Chapter 2, we observed that if the substrate thickness was not increased with particle size, for larger particles, displacements of the entire NP-substrate system were observed. A direct comparison of the effects of substrate thickness are possible by comparing Figs. 2.3 and 4.4; these two simulations are identical, except the substrate thickness is thinner for the simulations presented in Fig. 2.3. Comparing the final states for the particle impacted with the thinner substrate (Fig. 2.3) to the particle impacted with the thicker substrate (Fig. 4.4), both the density of partial dislocations present in the impacting particle and the aspect ratio of the particle are lower. This shows the effective compliance of the substrate affects both the magnitude of the deformation and the deformation mechanisms that are active.

4.4: CONCLUSIONS

MD simulations were conducted for the impact of an Ag NP of fixed size and impact velocity onto a substrate while the crystallographic orientation of the impacting NP was systematically varied to understand the influence of particle impacting orientation on the deformation of the NPs. The case where the impacting NP was oriented with the same crystallographic orientation as the substrate was considered as well as cases where the NPs were rotated from 0˚–45˚ about both the x and y directions in order

to explore a range of possible impacting orientations. The deformation of the NPs in each simulation was quantified by measuring the aspect ratio of the deformed NPs and this was compared to the calculated Schmid factor. The lack of a direct correlation between the measured aspect ratios and the Schmid factors suggests that the underlying deformation mechanisms cannot be directly correlated to the stress to initiate plastic deformation. Thus, additional simulations were conducted for the cases where the maximum and minimum deformations were observed to study the underlying deformation mechanisms that are responsible for the range of deformations in the impacted NPs.

The largest deformation was observed when the impacting NP was oriented along the [001] direction (including rotations about the [001] impact axis) and these orientations were denoted as soft orientations. Two simulations were conducted with soft orientations: a) NP and substrate having the same orientation and b) NP and substrate relatively rotated by 45˚ about the [001] impact axis. The time evolution the deformations were further studied to understand the mechanisms responsible for deformation behavior as well as to observe the role of NP-substrate rotation on the deformation of the impacting NP. In both cases, the large deformation was attributed to a pyramidal feature comprised of propagating partial dislocations nucleating from the contact patch between the NP and the substrate. This pyramidal feature acts like a rigid wedge that results in the bending of atomic rows in the upper region of the NP where the von Mises stresses are increased by this deformation. Relaxation of strains in this region and further deformation

is aided by the disordering and subsquent recrystallization of atoms as well as nucleation of new partial dislocations from the highly stressed zone.

The impacts that resulted in the smallest deformations, which we denote as hard impacts, were observed when the NP was aligned along [111] and [101]. This was attributed to the orientations of the close-packed {111} planes that experience high von Mises stress. For the hard impact directions, the partial dislocations emerging from the contact patch do not lock and intersect to form a pyramidal formation. Although these partial dislocations still relieve some stress following the NP impact, the absence of the rigid pyramidal feature leads to a lower overall deformation of the impacting particle.

Control of the microstructures of films produced by impact requires an understanding of the role of process variables on deformation mechanisms. Previously, it has been shown that particle size and particle impact velocity influence the mechanisms for deformation that occur during the early stages of impact as well as the final microstructure of the particle-substrate [1]. This study shows that the orientation of the impacting particle also plays a significant role, even when the particle size, particle velocity and substrate orientation are fixed. Further work is needed to assess whether the substrate orientation also affects the deformation mechanisms. A systematic understanding of all of the variables that influence deformation could lead to the ability to control the microstructure of deposited films such that films with a broad range of microstructures – from nanocrystalline to monocrystalline may be possible.

4.5: REFERENCES

1. T.V. Chitrakar, J.W. Keto, M.F. Becker, D. Kovar, Acta Mater. 135, 252 (2017).

2. T.V. Chitrakar, G. J. J. Noiseau, J.W. Keto, M.F. Becker, D. Kovar, J. Appl. Phys. 125, 195104 (2019).

3. W.D. Callister, D.G. Rethwisch, *Materials Science and Engineering: An Introduction* (John Wiley and Sons, MA, USA, 2010).

4. S. Plimpton, J Comp Phys. 117, 1 (1995) (http://lammps.sandia.gov).

5. Lonestar Linux Cluster, TACC (http://www.tacc.utexas.edu).

6. P.L. Williams, Y. Mishin, J.C. Hamilton, Modelling Sim. Mater. Sci. Eng. 14, 817 (2006) (http://www.ctcms.nist.gov/potentials/Ag.html).

7. C. Huang, W.T. Nichols, D.T. O'Brien, M.F. Becker, D. Kovar, J.W. Keto, J. Appl. Phys. 101, 064902 (2007).

8. W. Shinoda, M. Shiga, M. Mikami, Phys Rev B. 69, 134103 (2004).

9. A. Stukowski, Modelling Simul. Mater. Sci. Eng. 18, 015012 (2010).

10. P.M. Larsen, S. Schmidt, J. Schiøtz, Modell. Simul. Mater. Sci. Eng. 24, 055007 (2016).

11. O. Engler, V. Randle, *Introduction to Texture Analysis: Macrotexture, Microtexture and Orientation Mapping* (CRC press, Taylor and Francis Group, Boca Ration, Florida, USA, 2010).

12. Y. Jin, M. Bernacki, G.S. Rohrer, A.D. Rollett, B. Lin, N. Bozzolo, In: Proceedings of 5th International Conference on Recrystallization and Grain Growth (ReX and GG 2013), May 5–10 (2013); Sydney, Australia.

CHAPTER 5: A Quantitative Criterion to Predict Atomic Disordering during High Velocity Particle Impact [3]

5.1: INTRODUCTION

A variety of aerosol deposition processes are utilized to produce thick films by accelerating particles to a high velocity and impacting the particles onto a substrate to build up a film [1–3]. Although the impact velocities are similar (300–1000 m/sec) for these processes, the particle sizes used in each process varies considerably. The cold spray process utilizes 5–40 μm particles [4], whereas the aerosol deposition process typically uses 0.1–0.4 μm particles [5–7]. Still smaller 2–40 nm particles are used in the laser ablation of microparticle aerosol (LAMA) process [3, 8, 9]. It is these finest particles that are the subject of this current chapter.

Independent of the size of the impacting particles used in LAMA, it has been reported that the grain size in the films differs from that of the impacting particles [10–12] suggesting that microstructural refinements occur upon impact. An extreme example of these microstructural refinements is predictions that single crystal films may be obtained under certain processing conditions [13]. Such extreme control of the microstructure in films requires an understanding of the mechanisms that result in grain refinement processes upon high speed impact, and there have been several recent studies

[3] T. V. Chitrakar, J. W. Keto, M. F. Becker, D. Kovar, *In preparation for submission in the Journal of Applied Physics* (I performed the simulations and helped analyze the results)

aimed towards this goal. For example, it has been shown that the impact of nanoparticles at velocities greater than 600–1000 m/sec results in partial or complete atomic disordering of the impacting nanoparticle [14, 15]. These disordered regions play a critical role in determining the final state after impact because the disordering and subsequent recrystallization mechanisms dictate whether deposition is monocrystalline or polycrystalline.

Disordering and recrystallization following high velocity impact has been observed for particles with a range of sizes and impacting velocities in regions where there are large strains in the lattice [14]. These regions appear to disorder spontaneously after experiencing large strains for several picoseconds. Since both the magnitude of the strain and the time during which the atoms experience high strains influence disordering, this suggests that the energy of the system is a key criterion in the initiation of disorder. Atomic-scale strains consisting of bond length changes, rotations or bending increase the potential energy (PE) relative to the undistorted lattice. If one atom in a lattice is displaced, the PE with respect to its neighbors will be increased. If two adjacent atoms are displaced in the same direction, the PE increase will be less than if the same two atoms were displaced in opposite directions. In the first case, the lattice will appear deformed but not disordered. However, in the latter case, or if the displacements are in random directions, the lattice may appear disordered if the displacements are large enough. Thus, an increase in PE might logically be correlated with the onset of disorder. This observation has led us to hypothesize that disordering may result when an individual atom or a small ensemble of atoms experience an excess in PE that renders the crystal

unstable. We further hypothesize that this PE threshold may, for a given material, be invariant to impact conditions, stress state, and particle size.

In this chapter, we use molecular dynamic (MD) simulations to study this hypothesis for silver nanoparticles having diameters in the range of 4.5– 9 nm and impact velocities between 100–1200 m/sec. In order to do this, the potential energies for selected atoms in an impacting particle are tracked during and following impact for several combinations of particle velocity, particle orientation, and particle size. The onset of disordering versus time and position in the particle are then correlated with the PE for each atom. We show that for a given material there is a threshold PE above which the crystal lattice disorders, independent of impact conditions or particle size. The significance of this finding towards controlling film microstructure from impacted nanoparticles will be discussed.

5.2: SIMULATION PROCEDURES

MD simulations of the impact of a spherical FCC silver nanoparticle (NP) onto a flat stationary silver substrate were conducted using LAMMPS [16] implemented on the Lonestar5 Linux cluster at the Texas Advanced Computing Center (TACC) [17] at the University of Texas at Austin. Two graphics processing units (GPUs) coupled with a total 40 central processing units (CPUs) were employed to run the simulations. The embedded-atom-method (EAM) potential for Ag from the NIST Interatomic Potentials

Repository Project was used [18]. The total simulation volume was 60 × 60 × 80 lattice constants (lattice constant= 0.409 nm for Ag), with the larger dimension in the z direction, which corresponded to the NP impact direction. The substrate size was contained within the bottom 60 × 60 × 40 lattice units (583,200 atoms) The boundary conditions in all three dimensions were periodic for the simulation volume.

First, spherical particles with diameters of 4.5 nm (≈ 2750 atoms) were impacted onto the substrate at a range of velocities and crystal orientations. This particle size was selected because it is sufficiently large so that surface effects are not dominant, allowing particle deformation mechanisms to be studied [14]. We have only considered particles that are initially free of stacking imperfections; and consistent with experimental observations, we have assumed the particles to be free of surface oxides [3]. The impacting NP was initially placed such that its center was 20 lattice units above substrate. The Ag atoms in the substrate and the impacting NP were allowed to thermalize at 300 K for 80 ps before the smaller NP was set in motion in the *z* direction. A constant velocity was imparted to all atoms in the impacting NP. The time integration for the equilibration of the system to 300 K and for the subsequent impact were performed with a time step of 0.001 ps (1 fs) using Nose-Hoover style, non-Hamiltonian equations of motion on the isothermal-isobaric (npt) ensemble [19]. The angular momentum of the impacting NP was set to zero at every timestep during thermalization to control particle orientation; the linear and angular momentum in the particle relative to the motion of the center of mass was set to zero every timestep prior to impact to preserve pre-impact orientation and to specify the impact location.

The positions, velocities, and potential energies of each atom were computed at every time step and captured every 50 fs (0.05 ps) for off-line analysis. Visualizations of the atomic positions were conducted using OVITO visualization software [20]. The PE is easily quantified using this procedure since it is calculated for each atom at each time step according to the potential function in use (EAM/alloy in this case). Polyhedral template matching (PTM) was used to identify the local atomic environment for all atoms in the simulations, which allowed the local crystal structure for the atoms to be determined [21]. The visualizations were color-coded with this information, with green representing local regions of FCC stacking and red representing regions with a local HCP stacking, and white being not identified or disordered. The PTM method was used to quantify the onset of disorder by defining a threshold root-mean-square deviation (RMSD). We set the RMSD threshold at the high end of the normal range, which resulted in the elimination of false positives that were not reasonable for Ag atoms (i.e. we retain only FCC, HCP, or unidentified structures). A cutoff value of the RMSD threshold of 0.15 was used in our simulations, which produced results that agreed with visual inspections of ordered and disordered regions of the simulations.

As described in Chapter 4 and in [22], it has been shown previously that NP impact velocity, NP orientation, and the relative misorientation between the NP and substrate are all important variables that influence the number of active partial dislocations and the planes on which they propagate. This in turn influences the magnitude of deformation experienced by the NP and substrate, the extent of disordering that occurs upon impact and the final state of the particle/substrate after impact.

Orientations that result in a relatively large magnitude of deformation at a given velocity are defined as soft orientations that also result in extensive atomic disordering, whereas hard orientations result in much less deformation and disordering.

A useful criterion for predicting the onset of disordering should be capable of predicting the onset of disordering independent of the mechanism, magnitude, or extent of deformation. Thus, impact parameters with the broadest possible range of deformations were selected to test our hypothesis. A set of simulations was first conducted by varying the impact velocity. In these simulations, the particle and substrate orientations were fixed such that the impact axis was oriented along [111] in the NP and the substrate surface normal was aligned along [001]. The simulations were performed at velocities of 100, 300, and 600 m/sec (≈ 0.006, 0.05, and 0.2 eV/atom). A second set of simulations was conducted with a fixed velocity (300 m/sec), but the particle and substrate orientations were varied to influence the active partial dislocation systems and the extent of deformation. Finally, a third set of simulations was conducted to assess the influence of particle size by impacting a larger 9 nm NP at 1,200 m/sec.

5.3: RESULTS

General Observations

Fig. 5.1 shows a snapshot 5 ps after impact at 300 m/sec for a representative impact of a 4.5 Ag NP with a [101] orientation onto a substrate with a [001] orientation. Significant deformation is apparent near the particle-substrate interface in both the lower regions of the particle and in the upper regions of the substrate. Several bands of red atoms are visible in the particle and substrate, indicating that the normal FCC atomic structure in these regions (green) has converted to a HCP structure as a result of the motion of partial dislocations. In the regions nearest to the particle-substrate interface, the atoms are white, indicating that the atomic structure has disordered. As has been detailed elsewhere [14], the disordered regions expand in subsequent timesteps, before shrinking due to recrystallization. The upper regions of the particle, which remain green, have not deformed significantly and the atoms within these regions remain FCC throughout the impact event.

Although the details of the location and extent of deformation varies with impact conditions, these general observations hold across all of the impact conditions studied and allow regions of the impacting particles to be identified and compared across impact conditions. For example, beyond a critical velocity, there is for each impact condition a region where disorder occurs near the contact region. Similarly, there are regions where stacking imperfections arise and there are other regions where deformation is minimal

and no changes to the lattice are apparent. The relative size of these regions varies with the impact conditions.

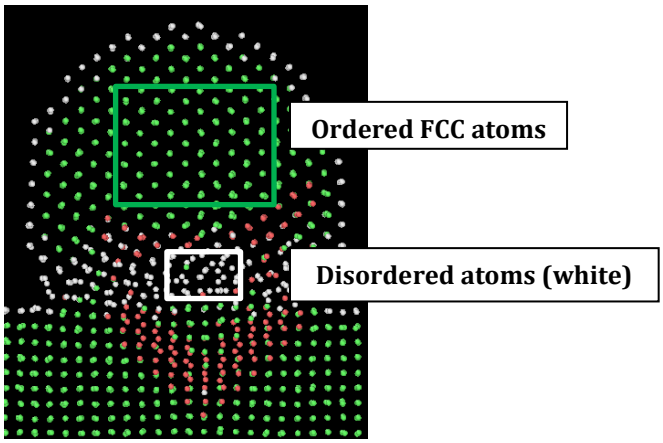

Figure 5.1: A PTM snapshot (5 atomic layers thick central cross-section) obtained 5 ps after impact for a NP with its impact axis oriented along [101] impacted onto a substrate whose surface normal is along the [001]. Atoms near the particle/substrate interface are disordered whereas atoms near the top of the NP are still ordered with a FCC crystal structure.

Twelve atoms for each impacting particle, shown in Fig. 5.2, were selected for further detailed study. The location of the 12 atoms was similar for each simulation, but, due to differences in the orientations of the nanoparticles, it was not possible to select identical atom locations when the particle orientation was varied. However, as shown in Fig. 5.2, the atom locations were based on the defined deformation behavior observed in different regions of the particle. Three atoms were selected from the upper portion of the particle, where little deformation and no disordering was experienced upon impact for any of the impact conditions that were studied. Nine atoms were chosen near the particle/substrate interface (3 rows of atoms x 3 atoms on each row), where deformation and disordering varied, depending on the impact conditions.

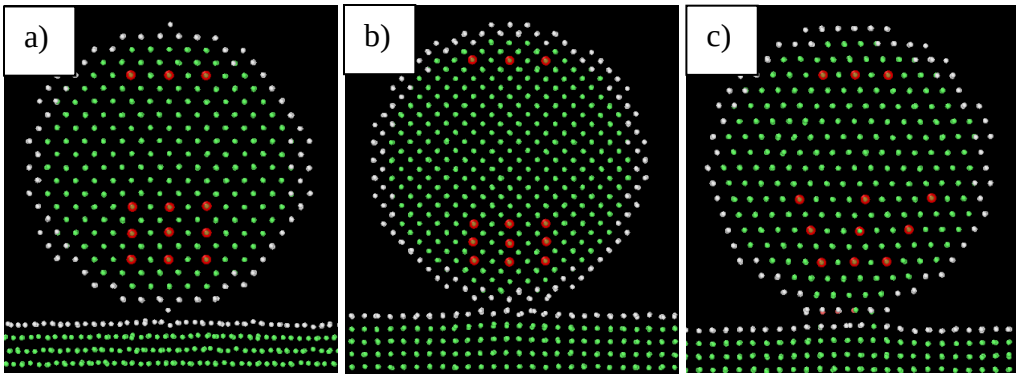

Figure 5.2: The 12 atoms (red) that were selected for calculation of PE for the a) [001], b) [101] and c) [111] oriented particles.

Our hypothesis is that the potential energy can be used as a quantitative predictor of disordering. To test this hypothesis, the PE was calculated for each of the twelve selected atoms at every 0.05 ps during the impact event. Since these simulations were conducted at room temperature, there are finite thermal fluctuations in PE. These fluctuations increase in regions of the particle that experience significant heating as the particle velocity is converted to heat upon impact before subsequently cooling. Thus, the PE was time-averaged in an effort to reduce the scatter in energy associated with these thermal fluctuations. The averaging was performed as a running average of seven data points, e.g. a running average over the previous 0.3 ps.

For these plots, the time-averaged PE is plotted as a colored solid line when the atom is ordered. A circle demarcates the time where the PTM indicates that the atom has disordered, and the line is dashed for all subsequent times. The three atoms located near the top of the particle which do not disorder for any of the impact conditions that were studied are all colored grey. The line for each of the other atoms are color-coded with a

unique color that indicates its location (See the legends in Figs. 5.3 and 5.4). For each plot, the average critical PE at which disordering was observed for all of the monitored atoms that disordered is indicated by the bold, black, horizontal line and one standard deviation above and below this PE are plotted as horizontal, black, dashed lines. We have not indicated on these plots the time at which the disordered atoms recrystallize, since the focus of this work is only on a criterion to predict the *onset* of disordering.

Influence of Impact Velocity

In Fig. 5.3, PE versus time is presented for three simulations conducted at velocities of a) 100 m/sec, b) 300 m/sec, and c) 600 m/sec where the NP has its impact axis oriented along [111] and the substrate surface normal aligned along [001]. At the lowest velocity (Fig. 5.3(a)), all of the atoms initially have similar potential energy of approximately -2.83 eV/atom relative to vacuum, with small peak-to-peak variations of 0.025 eV/atom due to thermal fluctuations. For the atoms located near the top of the particle (grey) which experience minimal deformation or localized heating, the PE and the variations in PE with time remain nearly constant. For atoms located near the middle of the particle (yellow, green, and purple) there is a small increase in PE up to about -2.80 eV/atom after approximately 5 ps, but the atoms never disorder. The atoms located nearest the bottom of the particles experience the greatest deformation, and the PE rises noticeably when this region experiences significant deformation beginning about 3 ps after impact. For these three atoms, the PE continues to increase until it reaches approximately -2.72 eV/atom after about 5 ps, at which point the atoms disorder. The

threshold energy for disordering is not discreet. Instead, there are fluctuations apparent in the PE that increase as kinetic energy is converted into heat upon impact, and thus the energies at which disorder occurs are statistically scattered by an amount that is approximately equal to the variation in PE associated with thermal fluctuations. In summary, for atoms in which the magnitude of deformation was small, the PE remained below -2.70 eV/atom and no disorder was observed. A threshold PE to disorder atoms of approximately -2.70 eV/atom is observed for a 4.5 nm Ag particle impacting at 100 m/sec.

In Fig. 5.3(b), the particle velocity has been increased to 300 m/sec while maintaining the same particle and substrate orientations, and the same particle size as shown in Fig. 5.3(a). Again, for atoms near the top of the particle that experience minimal deformation (grey) the PE remains approximately constant at about -2.83 eV/atom. Also similar to that observed at lower velocities, the PE for the atoms closer to the bottom of the particle begins to increase as the atoms experience significant deformation. Compared to the impact velocity of 100 m/sec, a larger fraction of the atoms in the particle impacted at 300 m/sec experience significant deformation, and a total of five atoms are observed to disorder. The mean PE at which atoms disorder at an impact velocity of 300 m/sec is -2.74 eV/atom, which is similar to the threshold PE observed for disorder at the lower impact velocity. Two of the atoms disorder at anomalously low values of PE; one disordered at a PE of approximately -2.79 eV/atom, although it experienced significantly higher PE for some time before disordering at this lower value. The other atom disordered at a PE of about -2.87 eV/atom, which is anomalously low.

The calculated temperature for this atom at the instant it disordered was 216K, despite the large deformation experienced by this atom, which suggests that passage of a phonon may have lowered the PE just prior to disordering.

Fig. 5.3(c) is a plot of the PE versus time for an impact velocity of 600 m/sec. Compared to the impacts at lower velocities, the extent of and magnitude of the deformation is significantly increased. As a result, the PEs increase at earlier times and to larger values. There is a small increase in PE for the three atoms near the top of the impacting NP as the deformation reaches the top of the particle, but these atoms do not disorder. All of the other atoms are observed to disorder with an average value of PE = -2.73 eV/atom at the onset of disorder, which again is similar to the threshold for disordering observed at the lower velocities. Seven of the nine atoms that disorder do so at an energy within one standard deviation (±0.04 eV/atom) of the mean. One atom is observed to disorder at a slightly higher PE and one atom is observed to disorder at a slightly lower PE.

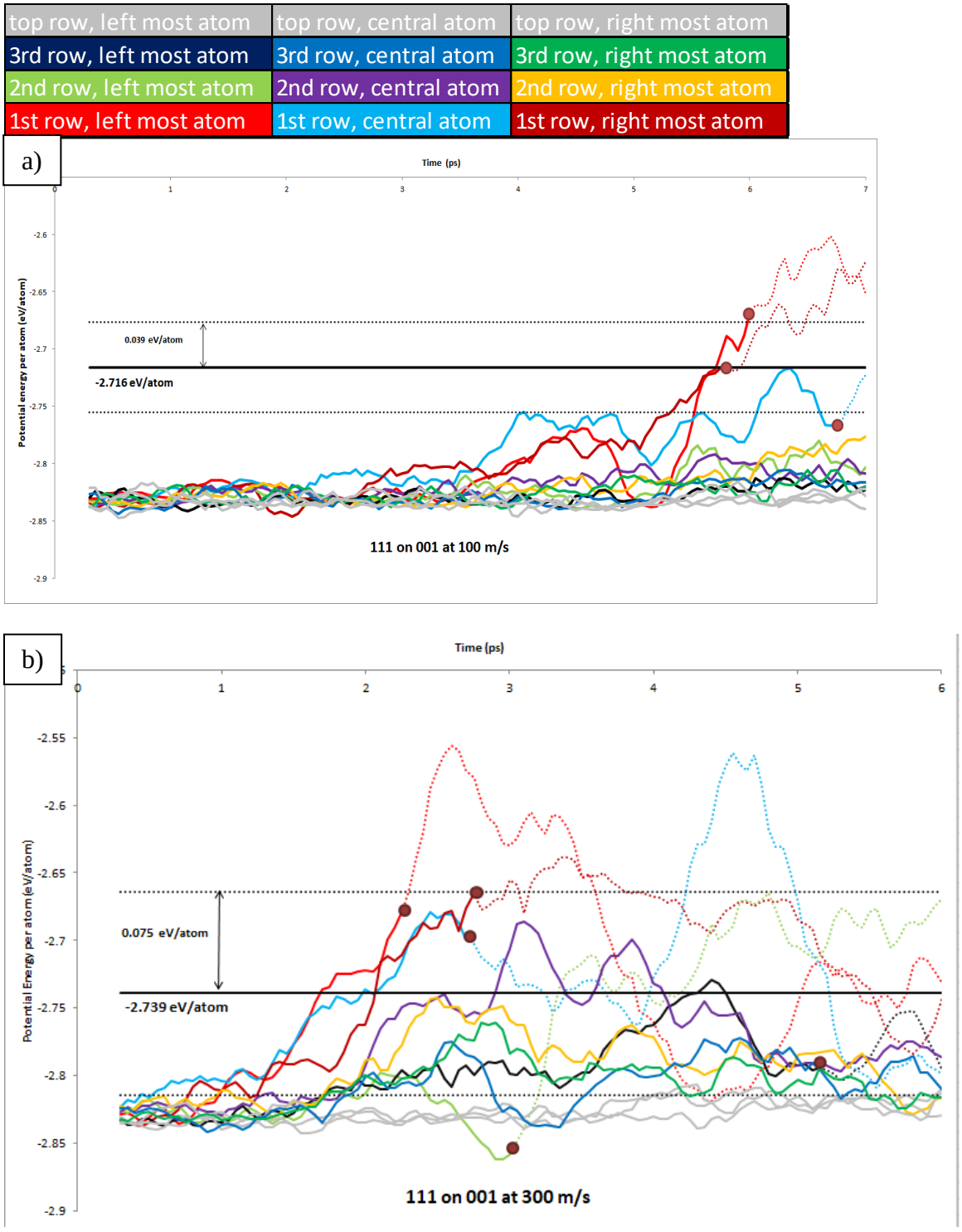

Figure 5.3: Plots of PE versus time for impact of a NP with a [111] orientation onto a substrate with an [001] orientation at a) 100 m/sec, b) 300 m/sec and c) 600 m/sec.

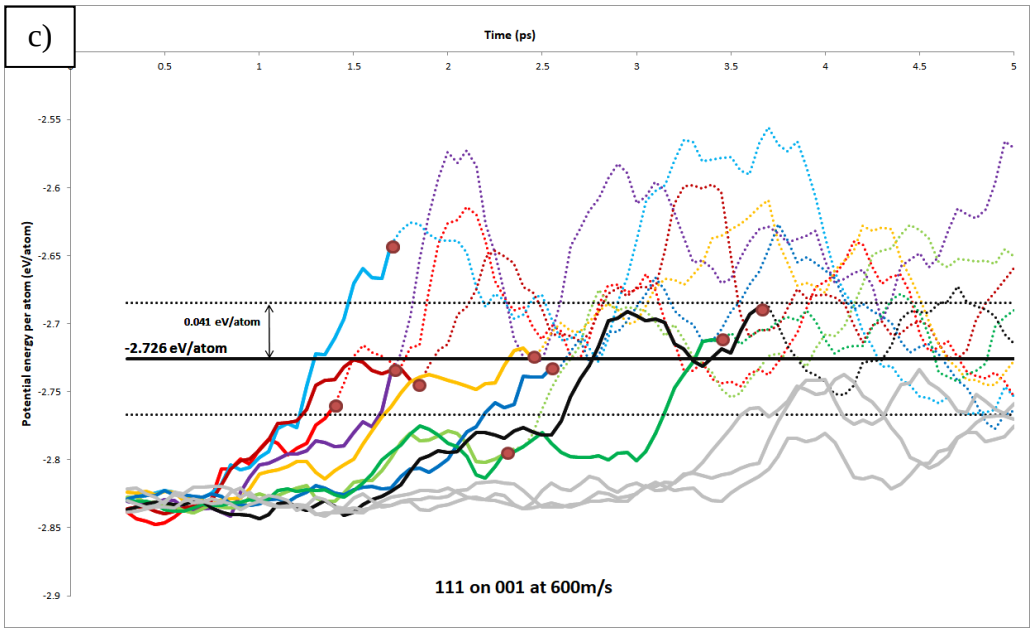

Figure 5.3: Plots of PE versus time for impact of a NP with a [111] orientation onto a substrate with an [001] orientation at a) 100 m/sec, b) 300 m/sec and c) 600 m/sec.

Influence of Particle/Substrate Orientation

To further test the hypothesis that disordering can be predicted based on a critical PE, additional simulations were performed where the impact velocity was fixed at 300 m/sec, but the particle impact orientation and/or the substrate orientation was varied. Since the extent and magnitude of the deformation are affected by the particle and substrate orientation, this provides an additional test of the generality of the disordering criterion. Three additional particle/substrate orientations were considered:

a) NP impact axis oriented along [001] with the substrate surface normal oriented along [001] such that the NP is rotated about the impact axis by 25˚ relative to the

substrate. This is considered a soft orientation for the particle, since the extent of deformation is relatively large.

b) NP impact axis oriented along [101] with the substrate surface normal oriented along [001]. This is considered a hard orientation for the particle since the extent of deformation is relatively small.

c) NP impact axis oriented along [111] with the substrate surface normal oriented along [111] such that the NP is rotated about the impact axis by 25˚ relative to the substrate. This is considered a hard orientation for the particle since the extent of deformation is relatively small.

For comparison, we also include the previous data for impact of a NP with a [111] orientation onto a substrate with an [001] orientation (a hard orientation), that was previously shown in Fig. 5.3(b) and this data is re-plotted in Fig. 5.4(a). In Fig, 5.4(b), the PE is plotted versus time for the case where the NP impact axis is oriented along [001] with the substrate surface normal oriented along [001] such that the NP is rotated about the impact axis by 25˚ relative to the substrate. Significant deformation is observed in the impacting particle, and the PE rises slightly even for the three atoms located near the top of the particle. The magnitude of the thermal fluctuations is larger than observed in Fig. 5.4(a) at the same impact velocity due to the greater extent of deformation for a [001] oriented NP and the associated heating. Although the atoms near the top of the particle do not disorder, the other nine atoms do, and the average threshold PE for the atoms that disorder is -2.75 eV/atom. Six of the nine atoms that disorder do so within one standard deviation (±0.04 eV/atom) of this mean, with two atoms disordering at a slightly lower

values and one atom disordering at slightly higher value. The larger fluctuations in PE are likely due to the larger thermal fluctuations due to the increased deformation relative to other cases that have been considered.

Fig. 5.4(c) shows the PE versus time for the case where the NP impact axis is oriented along the [101] with the substrate surface normal oriented along [001]. Although, in this case, significant local deformation is observed due to mass flow in the vicinity of the particle/substrate interface, the change in the shape of the particle upon impact is much less than that observed for the case shown in Fig. 5.4(b). Since the mass flow is localized near the contact surface only, the PE approximately remains the same for the three atoms located near the top of the particle. All nine of the atoms that are not located near the top of the particle disorder, and the average threshold PE for disorder is -2.71 eV/atom. Again, six of the nine atoms disorder at a PE within one standard deviation (±0.04 eV/atom) of the mean, with two atoms disordering at a slightly higher PE and one atom disordering at a slightly lower value.

Fig, 5.4(d) shows the PE versus time for the case where the NP impact axis is oriented along the [111] and the substrate surface normal is oriented along the [111] such that the NP is rotated about the impact axis by 25˚ relative to the substrate. Compared to the case considered in Fig. 5.4(b), the extent and magnitude of the deformation is considerably smaller for this case. The orientation of the {111} close packed planes for this impact orientation increase the density of partial dislocations which nucleate from the contact surface. Thus, the PE is slightly increased for the three atoms near the top of the NP. Six of the atoms disorder and the mean threshold PE for disordering is -2.72

eV/atom. Five of the six atoms disorder within one standard deviation (±0.04 eV/atom) of the mean and the sixth atom disorders more than one standard deviation above the mean, immediately after a rapid increase in PE.

To test whether the threshold PE to predict the onset of disordering is sensitive to particle size, an additional simulation was conducted in which a 9 nm particle was impacted onto a substrate at 1200 m/sec. The NP impact axis for this simulation was along [111] with the substrate surface normal oriented along [001] so that comparisons can be directly made with the smaller particle impacting at lower velocity shown in Fig. 5.4(a). Six of the nine atoms that were tracked and located near the bottom of the particle disordered upon impact and the average PE at which the disorder occurred was -2.71±0.11 eV/atom, which is consistent with the values recorded for smaller particles. This suggests that the critical PE for disordering is also not sensitive to particle size.

top row, left most atom	top row, central atom	top row, right most atom
3rd row, left most atom	3rd row, central atom	3rd row, right most atom
2nd row, left most atom	2nd row, central atom	2nd row, right most atom
1st row, left most atom	1st row, central atom	1st row, right most atom

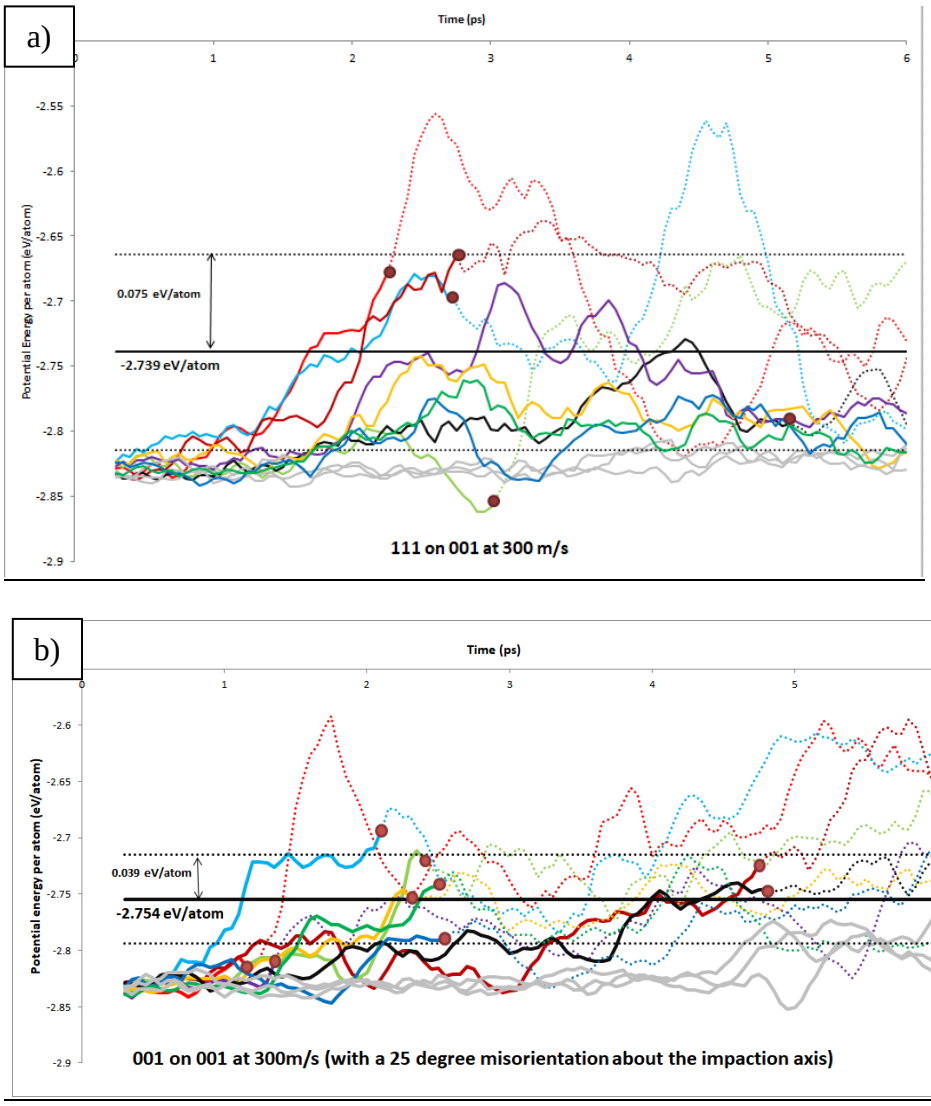

Figure 5.4: PE versus time showing the influence of NP orientation: a) NP impact axis oriented along [111] with the substrate surface normal oriented along [001], b) Both the NP and substrate have a [001] orientation; however, the NP is rotated about the impact axis by 25˚ relative to the substrate, c) NP impact axis oriented along [101] with the substrate surface normal oriented along [001], d) Both the NP and substrate have a [111] orientation; however, the NP is rotated about the impact axis by 25˚ relative to the substrate.

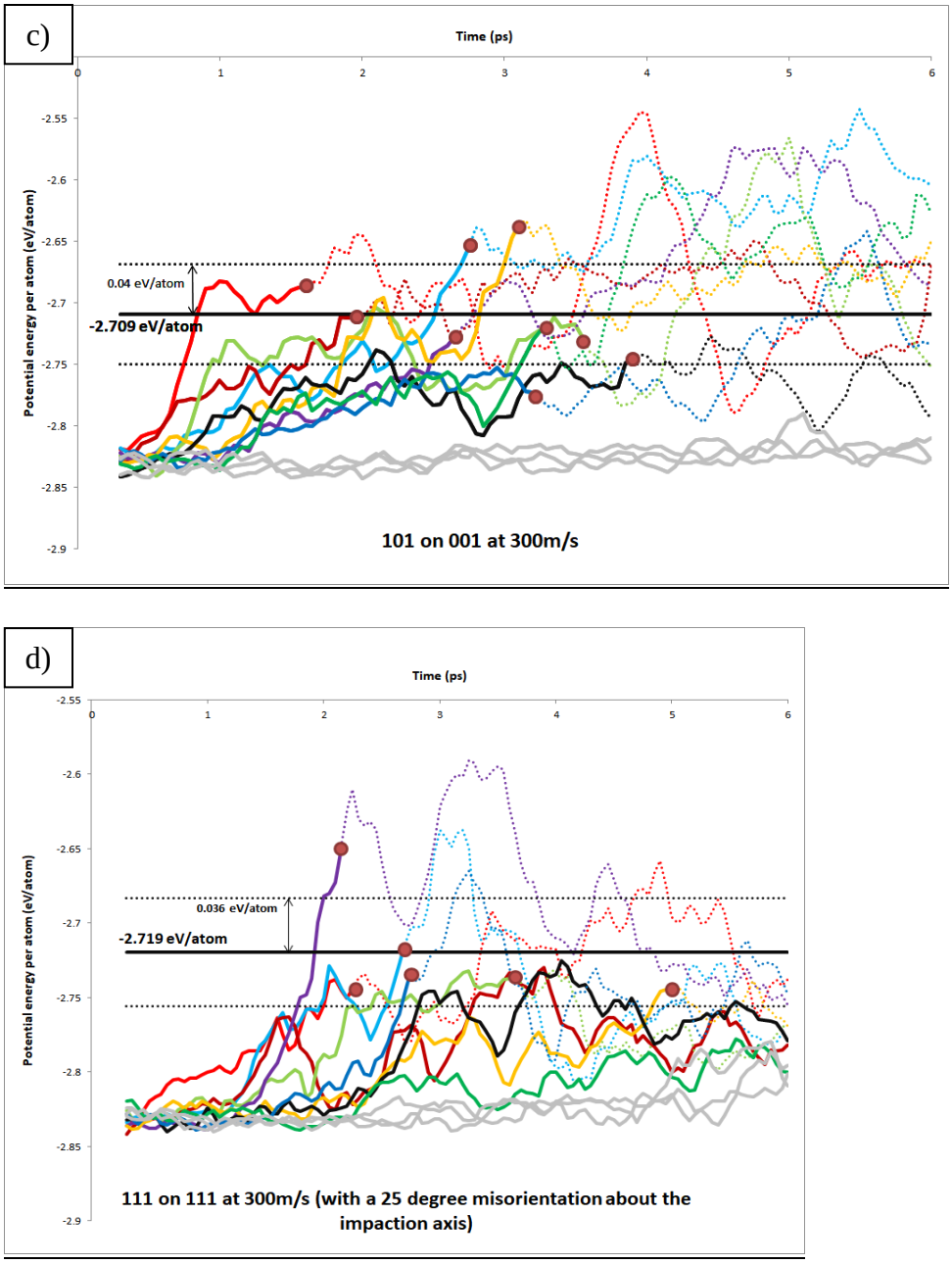

Figure 5.4: PE versus time showing the influence of NP orientation: a) NP impact axis oriented along [111] with the substrate surface normal oriented along [001], b) Both the NP and substrate have a [001] orientation; however, the NP is rotated about the impact axis by 25˚ relative to the substrate, c) NP impact axis oriented along [101] with the substrate surface normal oriented along [001], d) Both the NP and substrate have a [111] orientation; however, the NP is rotated about the impact axis by 25˚ relative to the substrate.

5.4: DISCUSSION

Analysis of the data in Fig. 5.3 suggests that disordering occurs at a threshold PE of approximately -2.7 eV/atom (compared to -2.83 eV/atom for the equilibrium lattice at 300 K), independent of the particle velocity and therefore the extent of deformation. Fig. 5.4 shows that this threshold PE is also independent of the particle/substrate orientation, which controls not only the extent of deformation, but also the active partial dislocation systems in the particle. The apparent invariance of the threshold PE for disordering of Ag is important because it has been shown previously that disordering can occur by at least two different mechanisms, depending on particle velocity and particle/substrate orientation. For example, for a 4.5 nm Ag particle impacting at 300 m/sec, it has been shown that disordering occurs spontaneously in the near-contact regions where the hydrostatic strains are maximum, but the deviatoric strains that drive partial dislocations are relatively small [14]. However, if the impact velocity is increased to 600 m/sec, significant disordering is observed far from the contact zone, where the deviatoric strains are much larger and where significant partial dislocation activity is observed. The disordering in this region has been attributed to multiple intersections of non-parallel partial dislocations. Our results show that the threshold PE for disordering does not depend on the mechanism for deformation. Finally, the simulation for a 9 nm NP at 1200 m/sec showed that the threshold for disordering is also invariant with NP size.

As was discussed previously, the threshold PE for disordering is not discreet, but rather there is a distribution of values at which disordering occurs. Considering all of the

simulations that were performed, the average threshold PE for disordering was -2.73±0.06 eV/atom. The nearly constant PE for disordering across a broad range of impact conditions suggests that disorder can be considered intrinsic to the material and is likely related to the crystal structure and bonding energies for the particular material. It is likely that a corresponding threshold energy could be computed for other materials using a similar approach so long as the material can be modeled using a spherically symmetric potential such as the Lennard-Jones or EAM potentials.

The standard deviations in the observed threshold PE for disordering of 0.06 eV/atom is greater than the room temperature thermal fluctuations, which are approximately 0.025 peak-to-peak eV/atom, based on the measured variations in PE for atoms that did not disorder and remained near room temperature throughout the impact event. However, it is important to note that the temperature of the atoms that are experiencing significant deformation prior to disordering experience brief but significant heating. For example, the maximum temperature for a 4.5 nm particle impacting at 600 m/sec is approximately 600K [14]. The calculated thermal energy associated with this temperature is 0.08 eV/atom. These calculations suggest that the variations in the PE at which disordering occurs is likely due to thermal fluctuations caused by localized heating following impact of the particle.

Although there have been predictions that suggest that epitaxial deposition may be possible using aerosol processes, these predictions have been based on simulations on a small number of impacting particles [13, 22], and experiments have not yet produced single crystal films. It is now recognized that epitaxial deposition requires atomic

disordering. The quantitative criterion to predict disordering that is presented here may be a further step in utilizing MD simulations to find impact conditions that produce epitaxial films over large areas.

5.5: CONCLUSIONS

Molecular dynamics simulations of Ag NPs impacting onto an Ag surface have been conducted under a variety of impact conditions. The PE of selected atoms were tracked during the impact event, and it was found that the PE increases as the strain increases in the lattice. Above a threshold PE of -2.73±0.06 eV/atom, it was observed that the atomic structure disordered, independent of the impact velocity, impacting particle or substrate orientation, or the particle size. This suggests that disordering is a fundamental material property for a given material that can be directly correlated to the distortion of the lattice and the resulting change in the potential energy of the atoms that disorder. The relatively small variations in the PE required to initiate disordering that were observed were attributed to thermal fluctuations that result from localized heating of the particle that occurs upon impact. A quantitative criterion to predict the onset of disordering such as we have presented may allow more detailed models to be developed that can predict the impact conditions required to completely disorder impacting particles, which is important since complete disordering has been identified as a necessary condition for the production of epitaxial films.

5.6: REFERENCES

1. H. Kreye, T. Stoltenhoff, In: Thermal Spray Surface Engineering via Applied Research: Proceedings of the 1st International Thermal Spray Conference, ASM international, Montreal, QUE, 2000; p 419.
2. J. Akedo, M. Lebedev, S. Nakano, H. Ogiso, Ceram. Eng. Sci. Proc. 24/3, 9 (2003).
3. C. Huang, W.T. Nichols, D.T. O'Brien, M.F. Becker, D. Kovar, J.W. Keto, J. Appl. Phys. 101, 064902 (2007).
4. T. Stoltenhoff, H. Kreye, H.J. Richter, J. Therm. Spray Tech. 11, 542 (2002).
5. A. Schroth, R. Maeda, J. Akedo, M. Ichiki, Jpn. J. Appl. Phys. 37, 5342 (1998).
6. J. Akedo, M. Ichiki, K. Kikuchi, R. Maeda, Sensors and Actuators A: Physical. 69, 106 (1998).
7. D. Hanft, J. Exner, M. Schubert, T. Stöcker, P. Fuierer, R. Moos, Journal of Ceramic Science and Technology. 6/3, 147 (2015).
8. W.T. Nichols, G. Malyavanatham, M.P. Beam, D.E. Henneke , J.R. Brock , M.F. Becker, J.W. Keto, In: Mat. Res. Soc. Symp. Proc., Nanophase and Nanocomposite Materials III, Materials Research Society , Warrendale, PA, 2000, editted by: Komarneni S, Parker JC, Hahn H; vol. 581: p 193.
9. G. Malyavanatham, D.T. O'Brien, M.F. Becker, W.T. Nichols, J.W. Keto, D. Kovar, S. Euphrasie, T. Loue, P. Pernod, J. Mat. Proc. Tech. 168, 273 (2005).
10. C. Borchers, F. Gartner, T. Stoltenhoff, H. Assadi, H. Kreye, J Appl Phys. 93/12, 10064 (2003).
11. M. Ichiki, J. Akedo, A. Schroth, R. Maeda, Y. Ishikawa, Jap. J. App. Phys. 36/9, 5815 (1997).
12. C. Huang, M.F. Becker, J.W. Keto, D. Kovar, J. Appl. Phys. 102, 054308 (2007).
13. H. Haberland, Z. Insepov, M. Moseler, Phys. Rev. B. 51, 11061 (1995).
14. T.V. Chitrakar, J.W. Keto, M.F. Becker, D. Kovar, Acta Mater. 135, 252 (2017).
15. H. Ogawa, J-Stage Mat. Transactions. 46/6, 1235 (2005).
16. S. Plimpton, J Comp Phys. 117, 1 (1995) (http://lammps.sandia.gov).

17. Lonestar Linux Cluster, TACC (http://www.tacc.utexas.edu).
18. P.L. Williams, Y. Mishin, J.C. Hamilton, Modelling Sim. Mater. Sci. Eng. 14, 817 (2006) (http://www.ctcms.nist.gov/potentials/Ag.html).
19. W. Shinoda, M. Shiga, M. Mikami, Phys Rev B. 69, 134103 (2004).
20. A. Stukowski, Modelling Simul. Mater. Sci. Eng. 18, 015012 (2010).
21. P.M. Larsen, S. Schmidt, J. Schiøtz, Modell. Simul. Mater. Sci. Eng. 24, 055007 (2016).
22. T.V. Chitrakar, G. J. J. Noiseau, J.W. Keto, M.F. Becker, D. Kovar, J. Appl. Phys. 125, 195104 (2019).

CHAPTER 6: Summary and Future Work

Thick films are produced via several related aerosol-based manufacturing processes by impacting particles onto a substrate at high velocities (100–1000 m/sec). A distinguishing characteristic between these manufacturing processes is the significant differences between the particle sizes of the impacting particles. The cold spray process utilizes 5–40 μm particles to produce thick films over large areas, whereas the aerosol deposition method (ADM) has been developed to deposit finer 0.1–0.4 μm particles onto patterned thick films. In the LAMA process, even finer 2–40 nm nanoparticles (NPs) are impacted to produce patterned, microscale thick films. Thick films produced by the deposition of particles larger than 0.1 μm using the cold spray and ADM techniques were observed to have higher relative film densities of 85–100% compared to relative densities of 70% produced using the LAMA process. Since the relative densities of films are an indirect measure of the magnitude of deformation that occurred upon impact, it can be inferred that the magnitude of deformation is dependent on particle size. The deformation mechanisms that occur during particle impact for particles less than 0.1 μm have not been previously systematically explored.

In this dissertation, molecular dynamic (MD) simulations have been used to study the deformation and deformation mechanisms that occur during high speed impact of Ag NPs. These simulations allow the NP size, NP impact velocity, and the NP crystallographic orientation relative to the substrate to be systematically varied and the resulting deformation mechanisms to be documented. The goal of this dissertation was to

develop a fundamental understanding of the available processing parameters during a single NP deposition event. This is a first step that is necessary to ultimately understand how film microstructures develop when thousands of particles are impacted to produce a film.

In Chapter 2, MD simulations were used to study the impact of a single Ag nanoparticle onto a flat {001} Ag substrate (the nanoparticle is oriented similar to the substrate except with a 45˚ rotation about its impact (001) *z* direction). Simulations were conducted for a range of nanoparticle sizes (2–9 nm) and particle impact velocities (10–1500 m/sec) that are experimentally accessible using the LAMA process. The goal was to study the corresponding deformation mechanisms and to observe how these mechanisms influenced the final structure of the deposited particle-substrate system. A transition from polycrystalline to epitaxial morphologies was observed with increases in the impact velocity for a fixed particle size. The transition from polycrystalline to epitaxial morphologies was also observed with decreases in the particle size for a given impact velocity. For particles larger than 3 nm and moderate impact velocities (300–600 m/sec), deformation was governed by the formation of a rigid-pyramidal structure created by initiation and propagation of a/6 $<11\bar{2}>$ partial dislocations lying along 4 non-parallel, intersecting {111} planes. This feature resulted in significant straining of the atoms outside of the pyramidal structure and was responsible for the high density of defects observed in the final polycrystalline NP-substrate system. The same mechanism was observed at higher velocities, but the increased magnitude of the strains at high impact velocities resulted in almost complete disordering of the impacting nanoparticle. Upon

cooling and recrystallization, the final NP-substrate system was epitaxial. This study showed that it may be possible to produce epitaxial films by particle impact if the particle size and velocity can be controlled.

Chapter 3 explored particle-on-particle impacts using a combination of experiments and MD simulations. A wide range of final states ranging from polycrystalline to epitaxial were observed experimentally using TEM even though the particle sizes and impact velocities were similar. This suggested that particle size and impact velocities may not be the only parameters that influence final morphologies. MD simulations were used to systematically study impact parameters independently that could not be controlled experimentally nor ascertained from *post mortem* observations, including particle crystallographic orientations and particle-particle crystallographic misorientations. Other key differences between the impact conditions studied in Chapter 2 and those studied in this chapter were 1) the impacting particle size was larger (13.6 nm) and 2) The impacted surface was a curved particle rather than a flat substrate. In this study, an alternative method of attaining epitaxial deposition was discovered which was favored when both the impacting and impacted particle axes were aligned near a <110> orientation. With small tilt misorientations between the impacting and impacted particles away from the <110>, asymmetric deformation and localized disordering was observed. The associated asymmetric mass flow resulted in tilting and reorientation of the impacting particle during the impact event. In the final state, the impacting particle had the same orientation as the impacted particle. It was found that this mechanism can produce epitaxial depositions for particles with tilt misorientations of up to 15˚ from the

<110> impact axis for 13.6 nm particles that impacted at a velocity of 860 m/sec. In summary, it was shown that, for a fixed particle size and impact velocity, a range of final states are produced depending on the orientations of the impacting and impacted particle. This suggested that a better understanding of particle orientation effects was needed to ascertain impact conditions that could produce fully epitaxial films.

In Chapter 4, MD simulations of the impact of a Ag NP of fixed size (4.5 nm) and impact velocity (300 m/sec) onto a substrate with a fixed crystallographic orientation were conducted to understand the influence of impacting particle orientation on the deformation of the NPs. These simulations were conducted by first considering an impacting NP with the same orientation as the substrate and then considering the influence of orientation as the NP was rotated about specific coordinate axes from 0˚–45˚. The lack of direct correlation between the magnitude of the deformation experienced by the impacting particle (as measured by the aspect ratios of the deformed NPs) and the calculated Schmid factors suggested that the range of deformation behavior could not solely be explained by the required stress to initiate plastic deformation. Thus, additional simulations were conducted for cases where maximum and minimum deformations were observed to study the underlying deformation mechanisms. The largest deformations (denoted as soft impacts) were observed when the impacting NP was oriented along the [001] direction (including rotations about the [001] impact axis) and the smallest deformations (denoted as hard impacts) were observed when the NP was aligned along the [111] and [101] directions. Similar to what was observed in Chapter 2, the large deformations were attributed to a rigid wedge-like pyramidal feature that bent the upper

atomic rows of the NP, leading to a region of high von Mises stress. Relaxation of strains in this region and further deformation was aided by the disordering-recrystallization of atoms as well as nucleation of new partial dislocations from the highly stressed zone. However, for the smaller deformations, the partial dislocations emerging from the contact patch did not lock and intersect to form a pyramidal structure. Although these partial dislocations still relieved some stress following the NP impact, the absence of the rigid pyramidal feature lead to a lower overall deformation of the impacting particle. A systematic understanding of the influence of particle impact orientations on a range of deformation behavior was obtained in this study.

MD simulations were used in Chapter 5 to track the potential energies (PE) for selected atoms in an impacting particle during and following impact for several combinations of particle velocity, particle orientation, and particle size (similar to the impact conditions explored in Chapters 2, 3 and 4). The onset of disordering of the selected atoms in the particle versus time and position were then correlated with the PE for each atom. It was observed that the PE increased as the strain increased in the lattice and above a threshold PE of -2.73±0.06 eV/atom, the atomic structure disordered, which was independent of the impact velocity, impacting particle or substrate orientation, and particle size. This suggested that disordering is a fundamental material property for a given material that can be directly correlated to the distortion of the lattice and the resulting change in the potential energy of the atoms that disorder. The relatively small variations in the PE required to initiate disordering were attributed to thermal fluctuations that result from localized heating of the particle upon impact. This quantitative criterion

to predict the onset of disordering may allow more detailed models to be developed that can predict the impact conditions required to completely disorder impacting particles. This is important as we previously showed that complete disordering followed by recrystallization is one of the mechanisms for obtaining epitaxial deposition.

This dissertation provides a comprehensive study of a single NP impact by predicting a range of deformation mechanisms depending on the impacting NP size, velocity and crystallographic orientation. These mechanisms explained the range of deformation behavior and final morphologies (from polycrystalline to epitaxial) observed for different combinations of these studied NP parameters. Since thick films are generated by the deposition of several of these single NPs, valuable insight into the formation of films can be obtained by this systematic study of understanding each NP deposition parameter. Above a critical impact velocity and irrespective of the impacting NPs' orientation, it was observed that film deformation is predominantly dependent on the nucleation and propagation of partial dislocations from the contact region between the NPs and that of the growing film. The subsequent disordering and recrystallization of atoms due to high strains in the impact zone following the motion of partial dislocations is shown to be important to facilitate epitaxial growth. However, epitaxy using this mechanism is possible only for smaller NPs at reasonably large impact velocities. Experimentally, a broad size distribution of NPs are typically observed. Since the acceleration of particles depends on their size, the particles in practice impact with a range of velocities. This explains why it is difficult to produce epitaxial films using the existing experimental setup.

However, this dissertation also provides guidance on how the currently produced LAMA films might be improved by tuning certain impact parameters. For example, it is clear that narrower particle size distributions should lead to less variation in particle velocities and a homogenization in the range of deformation behavior. To maximize this effect, smaller NPs are desirable since much higher deposition energies are needed for larger NPs which might lead to significant heating of the film and be detrimental retaining the as impacted microstructure. In addition, if it is possible to use external electric fields to align NPs such that their impact axes are aligned approximately along the <110> direction, it may be possible to produce epitaxial films at much lower impact energies. It is also possible that a larger range of particle misorientations from an exact <110> impact axis can be tolerated and still produce epitaxy by increasing the impact energy above the one used in this dissertation.

Although three important NP impact parameters were the focus of this dissertation, there are other parameters that could also be studied. NPs in this size range may have a large number of pre-impact defects like stacking faults or twins which has not been explored in this dissertation. Preliminary studies were performed where a single pre-existing twin was introduced at three different locations within the NP with the twin in each case oriented parallel to the substrate surface before impact. Deformation was observed up to the location of the twin, but it was observed to act as a barrier for disordering. Thus, the crystal structure above the twin remained intact. NPs containing twins located at the center of the NP were also impacted orthogonally to the substrate surface and it was observed that this resulted in even greater resistance to the propagation

of deformation of the NP. However, only a single twin in two different orientations were studied; thus, a systematic study of multiple defects at different locations in the NP and having different orientations is required to understand how pre-existing defects can influence particle deformation. Substrate orientation effects also need to be studied systematically. Lastly, to understand film formation mechanisms, multi-particle impacts are required. Although not presented in this dissertation, some preliminary studies were undertaken where four NPs were impacted in succession. A great challenge in performing multi-particle studies is that the number of variables increases markedly. For example, in addition to the variable that were studied in this dissertation for single particle impacts, one must consider the distances between the three impacted NPs, the angle of contact between the impacting NP and the three deposited NPs, and the possibilities that the particles may have different orientation. Thus, a study of these variables would require a large number of simulations.

BIBLIOGRAPHY

- A. Mette, P.L. Richter, M. Hörteis, S.W. Glunz, Prog. in Photovol.: Res. App. 15, 627 (2007).
- A. Schroth, R. Maeda, J. Akedo, M. Ichiki, Jpn. J. Appl. Phys. 37, 5342 (1998).
- A. Stukowski, Modelling Simul. Mater. Sci. Eng. 18, 015012 (2010).
- A. Tolvanen, K. Albe, Beilstein J. Nanotechnol. 4, 173 (2013).
- B. Yildirim, S. Muftu, A. Gouldstone, Wear. 270, 703 (2011).
- C. Borchers, F. Gartner, T. Stoltenhoff, H. Assadi, H. Kreye, J Appl Phys. 93/12, 10064 (2003).
- C. Borchers, T. Schmidt, F. Gärtner, H. Kreye, Applied Physics A. 90, 517 (2008).
- C. Borchers, T. Stoltenhoff, F. Gartner, H. Kreye, H. Assadi, In: Proceedings of the Materials Research Society Conference, San Francisco, CA, Apr 17-19, 2001; vol. 673: p 7.
- C. Huang, M.F. Becker, J.W. Keto, D. Kovar, J. Appl. Phys. 102, 054308 (2007).
- C. Huang, W.T. Nichols, D.T. O'Brien, M.F. Becker, D. Kovar, J.W. Keto, J. Appl. Phys. 101, 064902 (2007).
- C.E. Carlton, L. Rabenberg, P.J. Ferreira, Phil. Mag. Let. 88, 715 (2008).
- C.E. Carlton, P.J. Ferreira, Micron. 43/11, 1134 (2012).
- D. Hanft, J. Exner, M. Schubert, T. Stöcker, P. Fuierer, R. Moos, Journal of Ceramic Science and Technology. 6/3, 147 (2015).

- D. Huang, F. Liao, S. Molesa, D. Redinger, V. Subramanian, J. Electrochem. Soc. 150, G412 (2003).
- D. Hull, D.J. Bacon, *Introduction to Dislocations* (Butterworth-Heinemann, Oxford, GB, 2011).
- D. Mordehai, M. Kazakevich, D.J. Srolovitz, E. Rabkin, Acta Mater. 59, 2309 (2011).
- D.B. Williams, C.B. Carter, *Transmission Electron Microscopy*: A Textbook for Materials Science (Springer, New York, 2009).
- G. Malyavanatham, D.T. O'Brien, M.F. Becker, W.T. Nichols, J.W. Keto, D. Kovar, S. Euphrasie, T. Loue, P. Pernod, J. Mat. Proc. Tech. 168, 273 (2005).
- G.T. Gray, Ann. Rev. Mat. Res. 42, 285 (2012).
- H. Assadi, F. Gärtner, T. Stoltenhoff, H. Kreye, Acta Mater. 51, 4379 (2003).
- H. Haberland, Z. Insepov, M. Moseler, Phys. Rev. B. 51, 11061 (1995).
- H. Hsieh, R. S. Averback, H. Sellers, C. P. Flynn, Phys. Rev. B. 45/8, 4417 (1992).
- H. Hsieh, R. S. Averback, Phys. Rev. B. 42, 5365 (1990).
- H. Kreye, T. Stoltenhoff, In: Thermal Spray Surface Engineering via Applied Research: Proceedings of the 1st International Thermal Spray Conference, ASM international, Montreal, QUE, 2000; p 419.
- H. Ogawa, Mat. Transactions. 46/6, 1235 (2005).
- H. Tsuzuki, J.P. Rino, P.S. Branicio, J. Phys. D: Appl. Phys. 44, 055405 (2011).

- J. Akedo, M. Ichiki, K. Kikuchi, R. Maeda, In: Proceedings of the 1997 10th Annual International Workshop on Micro Electro Mechanical Systems, MEMS: 1997 Jan 26-30; IEEE, Piscataway, NJ, USA. Nagoya, Jpn: 1997. p 135.
- J. Akedo, M. Ichiki, K. Kikuchi, R. Maeda, Sensors and Actuators A: Physical. 69, 106 (1998).
- J. Akedo, M. Lebedev, Jpn. J. Appl. Phys. 38, 5397 (1999).
- J. Akedo, M. Lebedev, S. Nakano, H. Ogiso, Ceram. Eng. Sci. Proc. 24/3, 9 (2003).
- J. E. Hearn, R. L. Johnston, J. Chem. Phys. 107, 4674 (1997).
- J. Li, Modelling Simul. Mater. Sci. Eng. 11, 173 (2003) (http://mt.seas.upenn.edu/Archive/Graphics/A).
- J. Song, D. J. Srolovitz, Acta Materialia. 55, 4759 (2007).
- J.G. Bai and G.Q. Lu, IEEE Transactions on Device and Materials Reliability. 6, 441 (2006).
- J.G. Bai, T.G. Lei, J.N. Calata, and G.Q. Lu, J. Mater. Res. 22, 3494 (2007).
- J.G. Bai, Z.Z. Zhang, J.N. Calata, and G.Q. Lu, in: Proceedings of IMEC2005, ASME. 415 (2005).
- J.R. Greer, W.D. Nix, Phys. Rev. B. 73, 245410 (2006).
- K. Meinander, J. Frantz, K. Nordlund, J. Keinonen, Thin Solid Films. 425, 297 (2003).
- K. Meinander, K. Nordlund, J. Keinonen, Nuclear Instruments and Methods in Phys. Research B. 242, 161 (2006).

- K. Meinander, K. Nordlund, Phys. Rev. B. 79, 235431 (2009).
- K. Nordlund, T.T. Järvi, K. Meinander, J. Samela, Appl. Phys. A. 91, 561 (2008).
- L. B. Han, Q. An, S. N. Luo, W. A. Goddard, Materials Letters. 64, 2230 (2010).
- L. Bardotti, B. Prevel, P. Melinon, A. Perez, Q. Hou, M. Hou, Phys. Rev. B. 62/4, 2835 (2000).
- L. Dupont, G. Coquery, K. Kriegel, and A. Melkonyan, Microelectr. Rel. 49, 1375 (2009).
- Lonestar Linux Cluster, TACC (http://www.tacc.utexas.edu).
- M. Ichiki, J. Akedo, A. Schroth, R. Maeda, Y. Ishikawa, Jap. J. App. Phys. 36/9, 5815 (1997).
- M. Lebedev, J. Akedo, T. Ito, J. Cryst. Growth. 275, 1301 (2005).
- M. Nahar, I.F. Gallardo, K.L. Gleason, M.F. Becker, J.W. Keto, D. Kovar, J. Nanopart. Res. 13, 3455 (2011).
- M. Nahar, PhD Dissertation, (University of Texas at Austin, 2012).
- M. Nahar, J. W. Keto, M. F. Becker, D. Kovar, Journal of Electronic Materials. 44/8, 2559 (2015).
- M. S. Daw, M. I. Baskes, Phys. Rev. B. 29, 6443 (1984).
- M. S. Daw, M. I. Baskes, Phys. Rev. Lett. 50, 1285 (1983).
- M.A. Asoro, D. Kovar, P.J. Ferreira, Chem. Comm., 50/37, 4835 (2014).
- Muller, J. Appl. Phys. 61/7, 2516 (1987).

- O. Engler, V. Randle, *Introduction to Texture Analysis: Macrotexture, Microtexture and Orientation Mapping* (CRC press, Taylor and Francis Group, Boca Ration, Florida, USA, 2010).
- P. J. Steinhardt, D. R. Nelson, M. Ronchetti, Phys. Rev. B. 28, 784 (1983).
- P.L. Williams, Y. Mishin, J.C. Hamilton, Modelling Sim. Mater. Sci. Eng. 14, 817 (2006) (http://www.ctcms.nist.gov/potentials/Ag.html).
- P.M. Larsen, S. Schmidt, J. Schiøtz, Modell. Simul. Mater. Sci. Eng. 24, 055007 (2016).
- Q. Hou, M. Hou, L. Bardotti, B. Prevel, P. Melinon, A. Perez, Phys. Rev. B. 62/4, 2825 (2000).
- S. Link, C. Burda, Z. L. Wang, M. A. El-Sayed, J. Chem. Phys. 111, 1255 (1999).
- S. Plimpton, J Comp Phys. 117, 1 (1995) (http://lammps.sandia.gov).
- T. Stoltenhoff, H. Kreye, H.J. Richter, H. Assadi, in: Thermal Spray 2001 New Surfaces for a New Millennium: Proceedings of the International Thermal Spray Conference. (May 28-30, 2001) p: 409.
- T. Stoltenhoff, H. Kreye, H.J. Richter, J. Therm. Spray Tech. 11, 542 (2000).
- T.T. Jarvi, A. Kuronen, K. Meinander, K. Nordlund, K. Albe, Phys. Rev. B. 75, 115422 (2007).
- T.V. Chitrakar, G. J. J. Noiseau, J.W. Keto, M.F. Becker, D. Kovar, J. Appl. Phys. 125, 195104 (2019).
- T.V. Chitrakar, J.W. Keto, M.F. Becker, D. Kovar, Acta Mater. 135, 252 (2017).

- U. Scheuermann, Microelectr. Rel. 49, 1325 (2009).
- V.K. Champagne, M. Trexler, Y. Sohn, and G.E. Kim, in: ICAA13, 13th International Conference on Aluminum Alloys (John Wiley & Sons, Inc., 2012), p. 993.
- W. Bouwen, E. Kunnen, K. Temst, P. Thoen, M.J. Van Bael, F. Vanhoutte, H. Weidele, P. Lievens, R.E. Silverans, Thin Solid Films. 354, 87 (1999).
- W.D. Callister, D.G. Rethwisch, *Materials Science and Engineering: An Introduction* (John Wiley and Sons, MA, USA, 2010).
- W. Huang, W. Qian, M. A. El-Sayed, Y. Ding, Z. L. Wang, J. Chem. Phys. C Lett. 111, 10751 (2007).
- W. Shinoda, M. Shiga, M. Mikami, Phys Rev B. 69, 134103 (2004).
- W.T. Nichols, G. Malyavanatham, D.E. Henneke, J.R. Brock, M.F. Becker, J.W. Keto, H.D. Glicksman, J. Nanoparticle Research. 2, 141 (2000).
- W.T. Nichols, G. Malyavanatham, M.P. Beam, D.E. Henneke , J.R. Brock , M.F. Becker, J.W. Keto, In: Mat. Res. Soc. Symp. Proc., Nanophase and Nanocomposite Materials III, Materials Research Society , Warrendale, PA, 2000, editted by: Komarneni S, Parker JC, Hahn H; vol. 581: p 193.
- W.T. Nichols, J.W. Keto, D.E. Henneke, J.R. Brock, G. Malyavanatham, M.F. Becker, H.D. Glicksman, Applied Physics Letters. 78, 1128 (2001).

- Y. Jin, M. Bernacki, G.S. Rohrer, A.D. Rollett, B. Lin, N. Bozzolo, In: Proceedings of 5th International Conference on Recrystallization and Grain Growth (ReX and GG 2013), May 5–10 (2013); Sydney, Australia.
- Y. Qiang, Y. Thurner, T. Reiners, O. Rattunde, H. Haberland, Surf. Coat. Tech. 100-101, 27 (1998).
- Y. Wang, S. T. C. Dellago, J. Chem. Phys. 122**,** 214722 (2005).